Simultaneous Measurement of Top Quark Mass and Jet Energy Scale Using Template Fits at the CMS Experiment

Dissertation
zur Erlangung des Doktorgrades
des Fachbereichs Physik
der Universität Hamburg

vorgelegt von

Sebastian Naumann-Emme
aus Henstedt-Ulzburg

Hamburg
2011

Gutachter der Dissertation:	1. Prof. Dr. Peter Schleper 2. Prof. Dr. Thomas Müller
Gutachter der Disputation:	1. Prof. Dr. Peter Schleper 2. Prof. Dr. Johannes Haller
Datum der Disputation:	22.06.2011
Vorsitzende des Prüfungsausschusses:	Prof. Dr. Caren Hagner
Vorsitzender des Promotionsausschusses:	Prof. Dr. Peter Haussschildt
Leiterin des Fachbereichs Physik:	Prof. Dr. Daniela Pfannkuche
Dekan der Fakultät für Mathematik, Informatik und Naturwissenschaften:	Prof. Dr. Heinrich Graener

Abstract

In this thesis, pairs of top quarks produced in proton-proton collisions at a center-of-mass energy of 7 TeV and decaying in the muon+jets channel $t\bar{t} \to (b\mu\nu)(bqq')$ are analyzed using data that were recorded by the CMS detector in the year 2010 and correspond to an integrated luminosity of 35.9 pb^{-1}. A sample of 78 events is selected by requiring exactly one isolated muon and at least four jets, two of them being identified as jets from the decay of b quarks. Given these selection criteria, the expected fraction of $t\bar{t}$ events is 94%. The trijet mass, M3, and the dijet mass, M2, are reconstructed, taking into account the b-tagging information. M3 and M2 are estimators of the masses of hadronically decaying top quarks and the corresponding W bosons, respectively. Templates for M2 and for the event-wise mass difference $\Delta\mathrm{M}_{32} = \mathrm{M3} - \mathrm{M2}$ are parametrized as linear functions of the top quark mass, m_t, and the jet energy scale (JES). Based on the precise knowledge of the W boson mass, M2 provides a strong handle on the energy scale of jets from light quarks. The reconstructed M2 and $\Delta\mathrm{M}_{32}$ in data are compared to the template functions from simulation in a combined likelihood fit. The overall JES in the selected sample is found to be 1.048 ± 0.040 (stat) ± 0.015 (syst) relative to the simulated JES and the measured m_t is 167.8 ± 7.1 (stat+JES) ± 3.1 (syst) GeV. This is one of the first measurements of m_t at the Large Hadron Collider. Furthermore, the JES measurement is an important input for the commissioning of the CMS experiment for the upcoming measurements with more data in the near future.

Kurzfassung

In der vorliegenden Arbeit werden Ereignisse mit Top-Quark-Paaren analysiert, die in Proton-Proton-Kollisionen bei einer Schwerpunktsenergie von 7 TeV erzeugt wurden und im Myon+Jets-Kanal $t\bar{t} \to (b\mu\nu)(bqq')$ zerfallen. Der verwendete Datensatz wurde im Jahr 2010 vom CMS-Detektor aufgezeichnet und entspricht einer integrierten Luminosität von 35.9 pb^{-1}. Insgesamt 78 Ereignisse werden selektiert, die ein isoliertes hoch-energetisches Myon sowie mindestens vier Jets aufweisen, wobei verlangt wird, dass zwei der Jets dem Zerfall eines b-Quarks zugewiesen werden können. Der erwartete Anteil von $t\bar{t}$-Ereignissen nach diesen Selektionskriterien ist 94%. Dreijet- und Zweijet-Massen, M3 bzw. M2, werden unter Berücksichtigung der Zuordnung von Jets zu b-Quarks rekonstruiert. M3 und M2 dienen als Schätzer für die Massen von hadronisch zerfallenden Top-Quarks bzw. der zugehörigen W-Bosonen. Zusätzlich wird die Massendifferenz $\Delta\mathrm{M}_{32} = \mathrm{M3} - \mathrm{M2}$ in jedem Ereignis als Observable verwendet. Die Formen der erwarteten Verteilungen von M2 und $\Delta\mathrm{M}_{32}$ werden als lineare Funktionen der Top-Quark-Masse, m_t, sowie der Jetenergieskala (JES) parametrisiert. Dank der präzisen Kenntnis der Masse des W-Boson erlaubt die M2-Verteilung eine Messung der Energieskala von Jets leichter Quarks. Die in den Daten gefundenen Werte von M2 und $\Delta\mathrm{M}_{32}$ werden mit den erwarteten Verteilungen verglichen. Eine gemeinsame Maximum-Likelihood-Messung ergibt eine mittlere JES von 1.048 ± 0.040 (stat) ± 0.015 (syst) relativ zu der simulierten JES für die gewählten Ereignisse sowie $m_t = 167.8 \pm 7.1$ (stat+JES) ± 3.1 (syst) GeV. Dies ist eine der ersten Messungen von m_t am Large Hadron Collider. Darüber hinaus ist das Ergebnis der JES-Messung eine wichtige Information für die Vorbereitung des CMS-Experiments auf die kommenden Messungen mit mehr Daten in der nächsten Zeit.

Contents

Chapter 1

Introduction

The fundamental constituents of our universe, which cannot be further subdivided, are referred to as elementary particles. The aim of particle-physics research is to identify, describe and understand these particles, their properties and the interactions between them.

According to our current understanding, there are four fundamental forces: gravity, electromagnetism and the weak and strong nuclear forces. The latter three, successfully described by gauge theories, are the pillars of the Standard Model of particle physics. This theoretical framework accommodates almost all observations made up to now. It contains a relatively small number of elementary particles, which are classified into three basic types: quarks, leptons and fundamental bosons.

There are six quarks and six leptons, arranged into three generations of doublets in both cases:

$$\begin{pmatrix} u \\ d \end{pmatrix} \quad \begin{pmatrix} c \\ s \end{pmatrix} \quad \begin{pmatrix} t \\ b \end{pmatrix} \qquad \text{and} \qquad \begin{pmatrix} \nu_e \\ e \end{pmatrix} \quad \begin{pmatrix} \nu_\mu \\ \mu \end{pmatrix} \quad \begin{pmatrix} \nu_\tau \\ \tau \end{pmatrix}$$

All quarks and leptons are particles with spin $\frac{1}{2}$, i.e. fermions. The down-type quarks, down (d), strange (s) and bottom (b), have an electric charge of $Q = -\frac{1}{3}$, while the up-type quarks, up (u), down (d) and top (t), have $Q = +\frac{2}{3}$. The charged leptons, electron (e), muon (μ) and tau (τ), have $Q = -1$, whereas their partners, the neutrinos ν_e, ν_μ and ν_τ, do not carry electric charge. The masses range from 0.5 MeV for the electron to about 173 GeV for the top quark.* In the Standard Model, neutrinos are assumed to be massless. However, experimental evidence has been accumulated in the last years that neutrinos have very small but non-zero masses. All quarks and leptons have their respective antiparticles†, with identical mass and quantum numbers except for opposite parity and electric charge.

*The "natural units" of particle physics are used in this thesis, i.e. $\hbar = c = 1$.

†In the following, particle-conjugate states are often implied without explicitly naming them. If necessary, antiparticles are denoted with a bar (e.g. $\bar{q}$ for an antiquark).

The fundamental interactions of the Standard Model are mediated via the exchange of the gauge bosons γ, W, Z and g. The massless photon, γ, mediates the electromagnetic interaction between all electrically charged particles. The heavy W and Z bosons are the mediators of the weak force between all particles that carry a "weak charge" (quarks, leptons as well as the W and Z bosons themselves). While the Z does not carry electric charge, the W exists in two different states with an electric charge of $Q = \pm 1$. The massless gluon, g, which exists in eight different so-called color states, is responsible for the strong force between particles that carry a "color charge" (all quarks and gluons).

At small distances and, equivalently, at high energies, quarks and gluons behave like free particles. At large distances and low energies, in contrast, the strength of the color field increases until it finally becomes possible to reduce the potential energy by creating new particles out of the vacuum. As a consequence, bare quarks and gluons cannot be observed. They are confined inside hadrons, which have no net color charge. These phenomena, asymptotic freedom and confinement, are central aspects of Quantum Chromodynamics (QCD), the $SU(3)$ gauge theory that describes the strong nuclear force. The typical products of QCD processes are jets, bundles of particles that result from the hadronization of quarks and gluons.

In its simplest form, the $SU(3) \times SU(2) \times U(1)$ gauge symmetry of the Standard Model predicts that all elementary particles, including the gauge bosons, are massless. This is in contradiction to experimental observations. An additional field is therefore postulated that breaks the electroweak $SU(2) \times U(1)$ symmetry. The physical manifestation of this field is the Higgs boson, H. It grants masses to the W and Z bosons via gauge interactions and to the quarks and leptons via Yukawa interactions. For the fermion masses, m_f, one has $m_f = Y_f \cdot v/\sqrt{2}$, where $v = 246$ GeV is the vacuum expectation value of the Higgs field and Y_f is the strength of the Yukawa coupling. The measured masses suggest that the Yukawa coupling of the top quark is $Y_t \simeq 1$, while the others range from $Y_e \sim 10^{-6}$ for electrons to $Y_b \sim 10^{-2}$ for b quarks. The Higgs boson, however, remains the last elementary particle of the Standard Model that has not yet been observed. Direct searches have provided limits on the Higgs boson mass, m_H, and precise measurements of other electroweak parameters further constraint the possible values of m_H.

Among all elementary particles, the top quark plays a very special role. This is due to several reasons, which in the end are all connected with its large mass. The top quark lifetime ($\sim 10^{-25}$ s) is even shorter than the hadronization timescale ($\sim 10^{-23}$ s). It is the only quark that decays via a weak interaction before hadronization through the strong interaction could begin. Furthermore, virtual particle loops modify the predictions from perturbative electroweak calculations and, given the large mass, loops including top quarks yield the dominant contribution to these higher-order corrections, which are crucial, e.g., for indirect measurements of the Higgs boson. Again due to its large mass, the top quark also plays an important role in the production and decay of many new particles predicted by extensions of the Standard Model. The fact that the Yukawa coupling of the top quark

appears to be approximately unity has even motivated the postulation of exotic models implying that the top quark mass is one of the central parameters of nature.

The first direct experimental evidences for the top quark were found at the Tevatron, a machine colliding protons (p) with antiprotons ($\overline{\mathrm{p}}$) at center-of-mass energies $\sqrt{s}$ of nearly 2 TeV. The Tevatron remained the only place where top quark measurements could be performed for about 16 years. In 2010, the Large Hadron Collider (LHC) started to collide protons at $\sqrt{s} = 7$ TeV. Experiments at this energy are expected to eventually reveal the mechanism of electroweak symmetry breaking and to answer many other questions concerning the Standard Model and possible extensions or alternative theories. In any case, the LHC produces top quarks at a significantly higher rate compared to the Tevatron.

Already the first determinations of the top quark mass, m_t, at the LHC are important measurements, regardless of their impact on the experimental world average of m_t. Being the first direct measurements not performed at the Tevatron and the first measurements at $\sqrt{s} = 7$ TeV and in pp collisions instead of $\mathrm{p\overline{p}}$, they represent valuable systematic cross checks for the previous measurements of m_t. Furthermore, they are milestones on the way to precision measurements of m_t and of other observables in events with similar topology, including a large number of observables that would be sensitive to physics beyond the Standard Model. Finally, top quark mass measurements offer possibilities to calibrate aspects of the experimental setup that cannot be easily assessed from the data by other means.

This thesis includes one of the very first m_t measurements with LHC data. Events recorded by the Compact Muon Solenoid (CMS) experiment are analyzed. The chosen criteria for event selection aim at pairs of top and antitop quarks ($t\bar{t}$) that decay into one muon plus four or more jets. A template fitting technique is used to simultaneously determine m_t and the jet energy scale (JES).

A short review of previous m_t measurements and of the phenomenological context is given in Chapter 2 of this document. The LHC machine and the CMS detector are introduced in Chapter 3. A summary of the employed event simulation can be found in Chapter 4, while Chapter 5 describes the techniques and criteria used in the event reconstruction and selection. Chapter 6 contains a study of the jet energy scale in simulated events. The simultaneous measurement of m_t and JES is presented in Chapter 7. The results are summarized and a brief outlook is given in Chapter 8.

This thesis was endorsed by the CMS Top Quark Physics Analysis Group on the 19th of April 2011. In addition, the main results are included in a Physics Analysis Summary that is expected to be released by the CMS Collaboration in June [1].

Chapter 2

Top Quark Mass Measurements and their Phenomenological Context

2.1 Top Quark Production

The dominant mechanisms for the production of top quarks are based on $q\bar{q}$ annihilation and gg fusion. In both cases, a $t\bar{t}$ pair is produced via the strong interaction. The corresponding leading-order diagrams are shown in Fig. 2.1. At next-to-leading order, also gq and $g\bar{q}$ scatterings produce $t\bar{t}$ pairs.

The production of top quarks in hadron-hadron collisions can be described factorizing long-distance from short-distance effects. Each incoming hadron is regarded as a composition of so-called partons, quasi-free quarks and gluons that share the hadron momentum. The total $t\bar{t}$ production cross section in the collision of hadrons a and b can then be calculated as a convolution of parton distribution functions (PDFs) and cross sections for the interaction of partons i and j, with $i, j = g, q, \bar{q}$:

$$\sigma_{ab\to t\bar{t}} = \sum_{i,j} \int_{x_i} \int_{x_j} \mathrm{d}x_i \; \mathrm{d}x_j \; f_i^{(a)} f_j^{(b)} \sigma_{ij\to t\bar{t}} \tag{2.1}$$

Each PDF $f(x, \mu_F)$ describes the probability density for finding a parton that caries a fraction x of the longitudinal momentum of the hadron. μ_F is the energy scale used to separate the long-distance and short-distance regimes. The partonic cross sections $\sigma_{ij\to t\bar{t}}$, which depends also on the choice of the factorization scale μ_F and on $\sqrt{s}$ and m_t, can be calculated perturbatively while the PDFs have to be determined experimentally.

The $pp \to t\bar{t}$ cross section at $\sqrt{s} = 7$ TeV has been calculated at approximate next-to-next-to-leading order (NNLO) to be 163^{+10}_{-11} pb [2]. As shown in Fig 2.2, the theoretical predictions are in good agreement with the measurements performed so far.

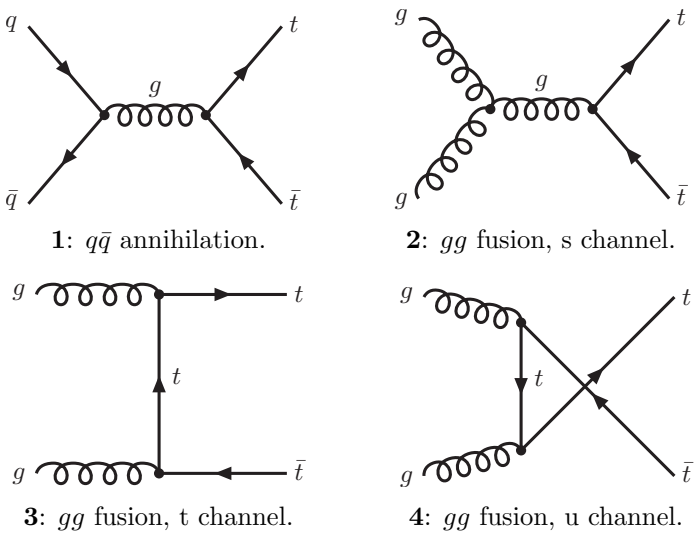

Figure 2.1: Diagrams for $t\bar{t}$ production at leading order.

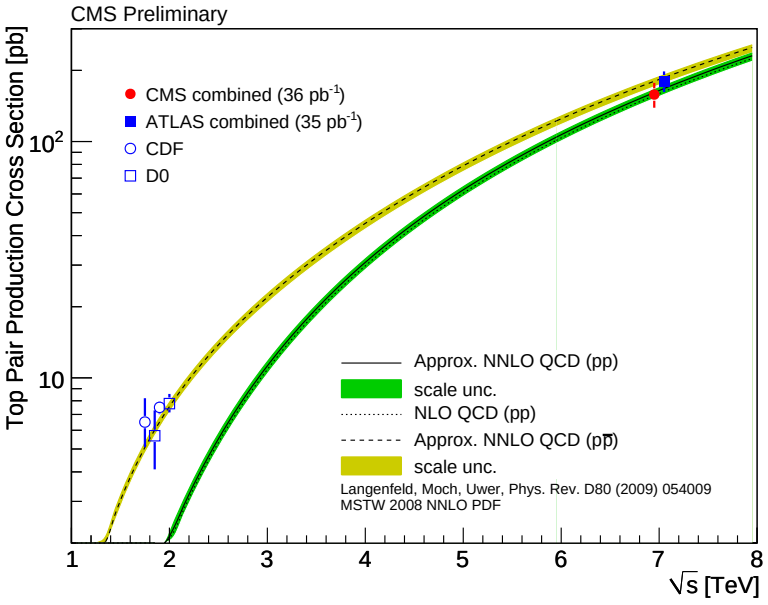

Figure 2.2: Theory predictions for the $t\bar{t}$ cross section as a function of $\sqrt{s}$ compared to measurements performed in $p\bar{p}$ collisions at 1.8 and 1.96 TeV and pp collisions at 7 TeV [3].

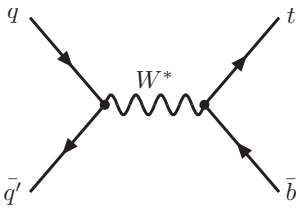

1: s-channel production with tb final state.

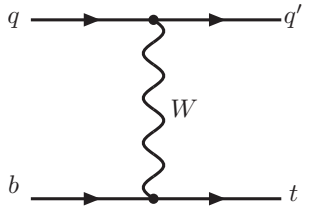

2: t-channel production with a tq final state.

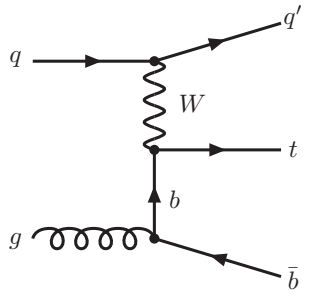

3: t-channel production with a tbq final state.

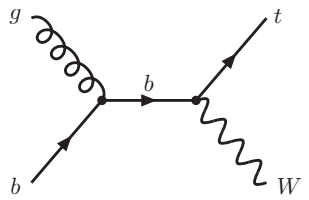

4: Associated tW production through the s channel.

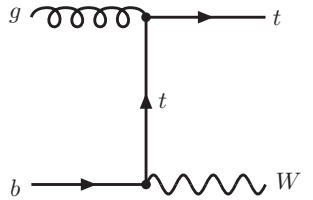

5: Associated tW production through the t channel.

Figure 2.3: Dominant diagrams for the production of single top quarks.

Besides the production of top quark pairs via the strong interaction, the production of single top quarks is possible via the weak interaction. Leading-order diagrams are shown in Fig. 2.3. Compared to $t\bar{t}$, the cross section for the production of single top quarks is only smaller by not much more than a factor of 2. However, events with single top quarks experimentally suffer from a much larger background.

2.2 Top Quark Decay

Top quarks decay via the weak interaction. As mentioned above, this happens even before a top quark could couple to any other quark through the strong interaction in order to form top-flavored hadrons. Since flavor-changing neutral currents are forbidden in the Standard Model, top quark decays that do not contain a W boson can only occur through

Table 2.1: Leading-order branching ratios for the decay of a W^+W^- pair. Taking into account the three color eigenstates of quarks and the fact that the sum of the quark masses in the third generation exceeds the W mass, there are nine decay modes for each W boson. This results in a total of 81 final states for the boson pair.

		W^+			
		$c\bar{s}, u\bar{d}$ $(\frac{6}{9})$	$e^+\nu_e$ $(\frac{1}{9})$	$\mu^+\nu_\mu$ $(\frac{1}{9})$	$\tau^+\nu_\tau$ $(\frac{1}{9})$
W^-	$\bar{c}s, \bar{u}d$ $(\frac{6}{9})$	36/81	6/81	6/81	6/81
	$e^-\bar{\nu}_e$ $(\frac{1}{9})$	6/81	1/81	1/81	1/81
	$\mu^-\bar{\nu}_\mu$ $(\frac{1}{9})$	6/81	1/81	1/81	1/81
	$\tau^-\bar{\nu}_\tau$ $(\frac{1}{9})$	6/81	1/81	1/81	1/81

higher-order diagrams and are thus highly suppressed. A variety of measurements, mainly from the b sector, constrain the elements of the CKM quark-mixing matrix. Whereas V_{tb} is close to unity, V_{ts} and V_{td} are rather small, resulting in a predicted branching ratio for the $t \to Wb$ mode of larger than 99.8%. The W boson subsequently decays either into a lepton and the corresponding neutrino or into a pair of light quarks.

The final states of $t\bar{t}$ decays are classified according to the decay modes of the two W bosons. The corresponding leading-order branching ratios are given in Table 2.1. Assuming that top quarks decay 100% of the time as $t \to Wb$, there are always two b quarks accompanying the decay products of the two W bosons. Each final-state quark leads to a jet of hadrons. It can be seen from Table 2.1 that the final state is fully hadronic in about 44% of the cases. In another 44%, one W boson decays leptonically while the other decays hadronically. This final state is referred to as the lepton+jets channel. One example is shown in Fig. 2.4. Both W bosons decay leptonically in about 11% of the cases. This is referred to as the dileptonic channel.

2.3 Top Quark Mass

2.3.1 Mass definitions

In quantum field theory, the propagator of a massive fermion with four-momentum p has a pole at the complex position $\sqrt{p^2} = m - \frac{i}{2}\Gamma$. The real part of this is called the on-shell or pole mass, which also corresponds to the invariant mass calculated from the four-momenta of the direct decay products. In this sense, the invariant mass reconstructed from the W boson and the b quark stemming from the decay of a top quark should be interpreted as the top quark pole mass. However, in the case of quarks a special situation arises from the confinement of the quarks due to their color charge. This applies also to top quarks

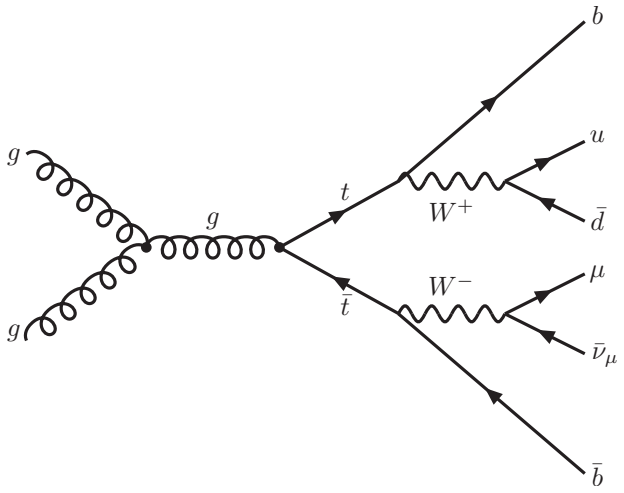

Figure 2.4: Example of a $t\bar{t}$ event in the muon+jets decay channel.

even though they decay via the weak interaction before a hadronization through the strong interaction could take place [4]. The b quark that arises from the decay carries on the color of the top quark. The strong interaction then forces the b quark to hadronize and at least one quark within the resulting color-neutral hadrons has to come from "somewhere else", i.e. is not a direct decay product of the top quark. Such long-range effects, which are softer than the lower scale of the perturbative calculations, lead to an irreducible ambiguity in the order of $\Lambda_{\mathrm{QCD}} \approx 0.2$ GeV for quark pole masses.

It is possible to define so-called short-distance masses that could in principle be measured with arbitrary accuracy and are at the same time well-behaved parameters from the theorist's point of view. At short distances and, equivalently, high energies, particle masses can be calculated within perturbation series. Divergences are removed using renormalization procedures. The most common choice in this context is the modified minimal subtraction ($\overline{\mathrm{MS}}$) scheme [5], in which the divergent part of the radiative corrections plus certain finite terms are subtracted from the particle amplitudes.

The relation between pole mass, m, and the short-distance mass in the $\overline{\mathrm{MS}}$ scheme, $\overline{m}$, has been calculated in up to three orders of the strong coupling constant α_s. A ratio of $m/\overline{m} \approx 1.06$ is found for the top quark [6], which means that a pole mass of 173 GeV would correspond to an $\overline{\mathrm{MS}}$ mass of 163 GeV.

Simulated events generated using Monte Carlo techniques are an import input for many top quark studies. The parameters corresponding to the top quark mass in these Monte Carlo generators are similar (though not necessarily identical) to the pole mass rather than to the $\overline{\mathrm{MS}}$ mass.

The experimental techniques that have been used so far in the determination of the top quark mass typically involve some Monte Carlo based calibration of the measured mass.

Furthermore, most measurements are based on the invariant mass of the top quark decay products. For these reasons, the measured top quark mass has been interpreted as the pole mass by the Particle Data Group [7]. For all other quarks, in contrast, the $\overline{\text{MS}}$ masses are used.

Comparing measurements of the cross section for top quark production with the predicted cross section from perturbative calculations can give an experimental handle on the top quark $\overline{\text{MS}}$ mass, thereby avoiding the intrinsic uncertainty in the order of Λ_{QCD}. However, this not only requires quite precise measurements of the cross section, it also has to be taken into account that the experimental extraction of the cross section usually involves information derived from simulated events and thus again the pole mass. With respect to the conditions at hadron colliders, a scan in the region of the $t\bar{t}$ production threshold performed at a future e^+e^- collider would offer incomparably better options for measuring the top quark $\overline{\text{MS}}$ mass.

In the last years, an interesting mass scheme based on event shapes has been developed [8]. The so-called thrust axis is used to assign the final-state objects of $e^+e^- \rightarrow t\bar{t}$ events to two hemispheres and the invariant mass is calculated for each hemisphere. The top quark mass is extracted from a double-differential cross section based on the hemisphere masses. The theoretical value of this double-differential cross section is calculated factorizing the final state into two "jet functions" and one "soft function". The jet functions can be calculated perturbatively and contain the actual mass dependence. The soft function, which is independent of the mass, comprises the non-perturbative part of the final state, in some analogy to the PDFs that cover the soft part in the factorization of hadronic initial states. While for $e^+e^- \rightarrow t\bar{t}$ mainly the experimental apparatus is missing, theoretical issues still have to be solved in order to allow such measurement in the hemisphere mass scheme to be performed at hadron-hadron colliders [9]. Most problems arise from influences of the less clean initial state of the scattering.

2.3.2 Electroweak fits

In many processes of high-energy physics, loops of virtual particles can lead to effects even from particles that are too heavy to be produced "on shell", i.e. as real particles given the available energy of the process. Example diagrams for such quantum fluctuations are shown in Figures 2.5 and 2.6. They correspond to higher-order corrections in perturbative calculations. The size of the resulting effect depends on the masses of the particles in the loops.

Of particular importance for tests of the Standard Model are contributions from virtual loops to the expected mass values of W boson, m_W, and Z boson, m_Z. Both masses are

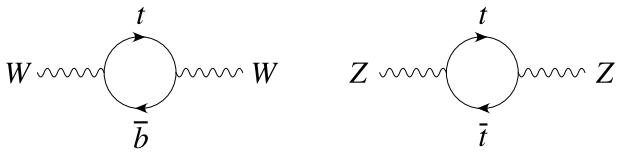

Figure 2.5: Virtual loops with top quarks in the W and Z propagators [10].

Figure 2.6: Virtual loops with Higgs bosons in the W and Z propagators [10].

related through the electroweak mixing angle θ_W:

$$\sin^2\theta_W = 1 - \frac{m_W^2}{m_Z^2} \tag{2.2}$$

Perturbative calculations for m_W yield [10]:

$$m_W^2 = \frac{\pi\alpha_e}{\sqrt{2}G_F \sin^2\theta_W \cdot (1-\Delta r)} \tag{2.3}$$

The electroweak mixing angle as well as the electromagnetic coupling constant α_e and the Fermi constant G_F have already been measured with high precision. The radiative corrections Δr arise from the virtual loops in the boson propagators. Diagrams like those in Fig. 2.5 exist with all types of fermions, but the large value of m_t makes the top quark contribution dominant [10]:

$$(\Delta r)_t \simeq -\frac{3G_F m_t^2}{8\sqrt{2}\pi^2 \tan^2\theta_W} \tag{2.4}$$

As a consequence, the value of m_t can be constrained via m_W (or m_Z). At the time of the first direct top quark observations, the constraints obtained using data from precise electroweak measurements already pointed exactly to the correct mass region. Currently, the latest global fit to the electroweak data yields 179^{+12}_{-9} GeV for the indirect measurement of m_t [11].

Figure 2.6 shows through which virtual loops the Higgs boson is expected to contribute. While the radiative corrections depend quadratically on m_t, the dependence on the Higgs boson mass, m_H, is only logarithmic [10]:

$$(\Delta r)_H \simeq \frac{3G_F m_W^2}{8\sqrt{2}\pi^2}\left(2\ln\frac{m_H}{m_Z} - \frac{5}{6}\right) \tag{2.5}$$

In this way, limits from direct Higgs boson searches can be complemented by constraints on m_H gained from electroweak fits, as illustrated in Fig. 2.7. Direct measurements of m_t are an important input for these fits.

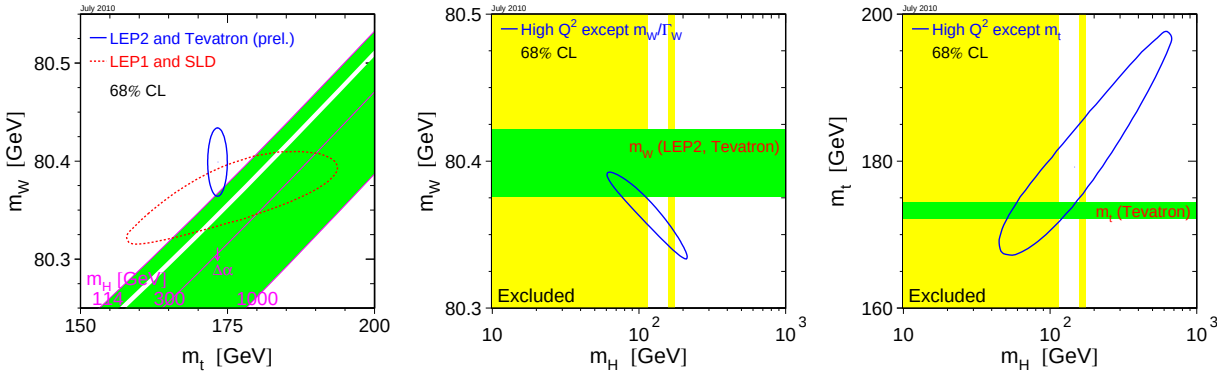

Figure 2.7: Comparisons of indirect constraints on the masses of the W boson, m_W, the top quark, m_t, and the Higgs boson, m_H, with direct measurements [11].

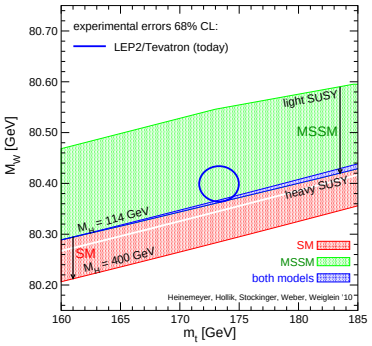

Figure 2.8: Comparison of the measured values of W boson mass, m_W, and top quark mass, m_t, to predictions by the Standard Model (SM) with different Higgs boson masses, m_H, and by the minimal supersymmetric extension (MSSM) with different masses of the supersymmetric particles [12].

Comparing predictions from perturbative electroweak calculations to precise measurements of m_W and m_t also allows one to test extensions of the Standard Model that include the existence of new elementary particles. Depending on their mass, virtual loops including these new particles could again yield non-negligible contributions to the radiative corrections for electroweak observables like m_W. The most popular extension of the Standard Model is Supersymmetry (SUSY), including a new bosonic partner for each Standard Model fermion and vice versa. Figure 2.8 shows that an increased precision in the measurements of m_W and m_t would allow for the experimental discrimination between the Standard Model and SUSY scenarios with different masses of the supersymmetric particles.

2.3.3 Direct measurements

A multitude of direct m_t measurements has been performed at the Tevatron, using all $t\bar{t}$ decay channels (lepton+jets, dileptonic and fully hadronic). Apart from the extraction of

the mass from the $t\bar{t}$ cross section, two main approaches can be identified: the template method and the matrix-element method.

For the template method, any measured quantity that has a significant correlation to m_t can be used. The distribution of such estimator in data is compared to the expected distributions for various assumed values of m_t. These so-called template distributions are obtained from simulated events. The most common estimators are invariant masses reconstructed from jets or from jets and leptons, but there are even measurements that simply take the transverse momentum, p_T, of the lepton as estimator or the transverse decay length of the b quark, calculated from the distance between the primary vertex of the event and a displaced secondary vertex.

In the matrix-element method, all possible assignments of reconstructed objects to the final-state fermions in leading-order matrix elements for production and decay of $t\bar{t}$ pairs are taken to account, each weighted by an m_t-dependent probability determined from the matrix element. An integration is performed over all possible momentum configurations of the colliding partons, using the corresponding PDFs, and over the final-state configurations. The correspondence between final-state four-vectors on parton level and measured quantities on detector level is described by so-called transfer functions. In general, the matrix-element method includes calculations that are much more time-consuming than those required for the template method, but in turn has a better statistical sensitivity.

Several variations of these two approaches haven been developed. The ideogram method, to name an outstanding example, combines some features of both approaches and lies in between the two in terms of computing time and statistical sensitivity. For a detailed discussion of the different techniques used in m_t measurements, see [13].

Since all methods make use of certain simplifications, any measured m_t has to be tested for biases. This is done by performing pseudo-experiments, i.e. running the analysis on simulated signal and background events, combined according to the respective expectations, and comparing the resulting m_t to the input value of the simulation. If necessary, a correction as a function of the measured values can be derived from the pseudo-experiments to calibrate the measurement for existing biases.

One of the largest systematic uncertainties in most m_t measurements arises from the JES uncertainty. This can be reduced either by minimizing the dependence of the analysis on the JES, choosing, for example, an m_t estimator like the lepton p_T or the decay length of the b quark, or by performing an in-situ JES calibration, typically comparing reconstructed dijet masses to m_W.

The current average obtained from the Tevatron is $m_t = 173.3 \pm 1.1$ GeV [14], as illustrated in Fig. 2.9. The most precise results have been obtained from the lepton+jets channel.

The first m_t measurement at the LHC was performed by the CMS Collaboration based on 36 pb^{-1} of data [15]. A result of 175.5 ± 4.6 (stat) ± 4.6 (syst) GeV was obtained

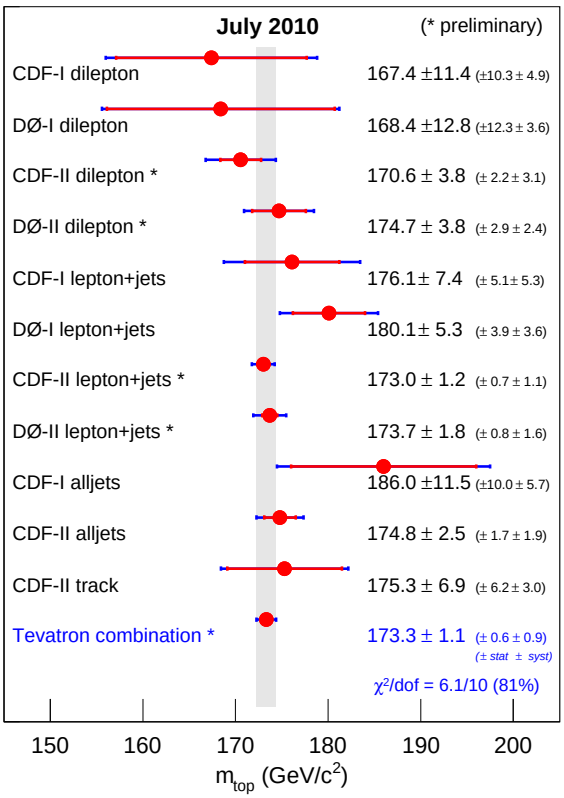

Figure 2.9: Summary of top quark mass measurements performed at the Tevatron [14].

by combining two analyses in the dileptonic $t\bar{t}$ channel. Both analyses are based on the template method and both solve kinematic equations for the $t\bar{t}$ system, but they differ in the techniques that are employed to derive estimators for m_t from the solutions of the under-constrained system.

The ATLAS Collaboration measured m_t using the template method in the lepton+jets channel [16]. They analyzed roughly the same integrated luminosity as CMS and obtained a result of 169.3 ± 4.0 (stat) ± 4.9 (syst) GeV.

Chapter 3

Experimental Setup

3.1 The Large Hadron Collider

The Large Hadron Collider (LHC) is a collider ring designed for pp collisions at a center-of-mass energy of 14 TeV [17]. It is operated by the European Organization for Nuclear Research CERN (formerly called Conseil Européen pour la Recherche Nucléaire) and located in the Swiss-French border region near Geneva. The LHC is also used for heavy-ion collisions, but only the operation mode with protons will be discussed here. The LHC has a circumference of 26.7 km and two beam-pipes with opposite magnetic dipole fields that guide the clockwise and anti-clockwise proton beam, respectively. The beams are brought to collision at four interaction points. One large detector is located at each interaction point: There are ATLAS and CMS, two multipurpose detectors, ALICE, a dedicated detector for heavy-ion collisions, and LHCb, specialized for the measurement of hadrons with b quarks.

The protons are pre-accelerated in a chain of linear accelerators and synchrotrons before they are injected in bunches into the LHC with an energy of 450 GeV. First stable pp collisions were provided by the LHC in November 2009, at the beginning with protons at injection energy, resulting in a center-of-mass energy of 900 GeV, then for a few days with protons at 1.18 TeV, i.e. a center-of-mass energy of 2.36 TeV. In 2010, the protons were accelerated up to an energy of 3.5 TeV. First collisions at a center-of-mass energy of 7 TeV were provided in March 2010.

Besides the center-of-mass energy, the main parameter of a collider is its instantaneous luminosity, $\mathcal{L}$, which correlates the event rate $\mathcal{N}$ of a given process with the cross section σ of this process:

$$\mathcal{N} = \mathcal{L} \cdot \sigma \tag{3.1}$$

The instantaneous luminosity can be calculated from the number of bunches N_b, the

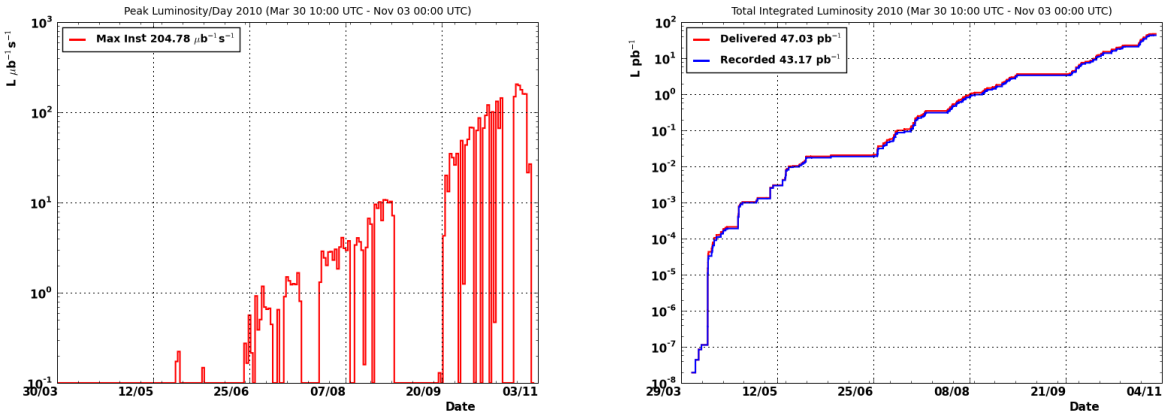

Figure 3.1: Maximum instantaneous luminosity per day delivered to CMS during stable beams (left) and total integrated luminosity as a function of time (right).

number of protons per bunch N_p, the revolution frequency f and the beam profile A at the interaction point:

$$\mathcal{L} = \frac{N_b N_p^2 f}{A} \tag{3.2}$$

Given that the protons travel the 26.7 km of the LHC almost at the speed of light, the revolution frequency is in the order of 11 kHz. The beam profile depends, among other parameters, on the transverse beam size, the longitudinal bunch size and the beam crossing angle.

In the 2010 pp running at $\sqrt{s} = 7$ TeV [18], the LHC started with relatively low intensities of 1 to $2{\cdot}10^{10}$ protons per bunch and only up to 50 widely spaced bunches were circulated. The instantaneous luminosity was about $8{\cdot}10^{26}$ cm^{-2} s^{-1} in the beginning. Finally, the nominal $1.15{\cdot}10^{11}$ protons per bunch were used and up to 348 colliding bunches, grouped in so-called bunch trains with a 150 ns spacing. The maximum instantaneous luminosity reached was $2{\cdot}10^{32}$ cm^{-2} s^{-1}. Figure 3.1 shows the evolution of instantaneous and integrated luminosity as a function of time. Note the logarithmic scales. Most of the integrated luminosity was delivered in the very last weeks of 2010 pp running.

3.2 The Compact Muon Solenoid

The CMS experiment [19] is located on one of the interactions points of the LHC, about 100 m underground. It is a detector with cylindrical layout, radially symmetric around the beamline and symmetric in both directions along the beamline from the interaction point. It has a length of 21.6 m and a diameter of 14.6 m. Figure 3.2 illustrates size and arrangement of the main detector components. They will be further described on the

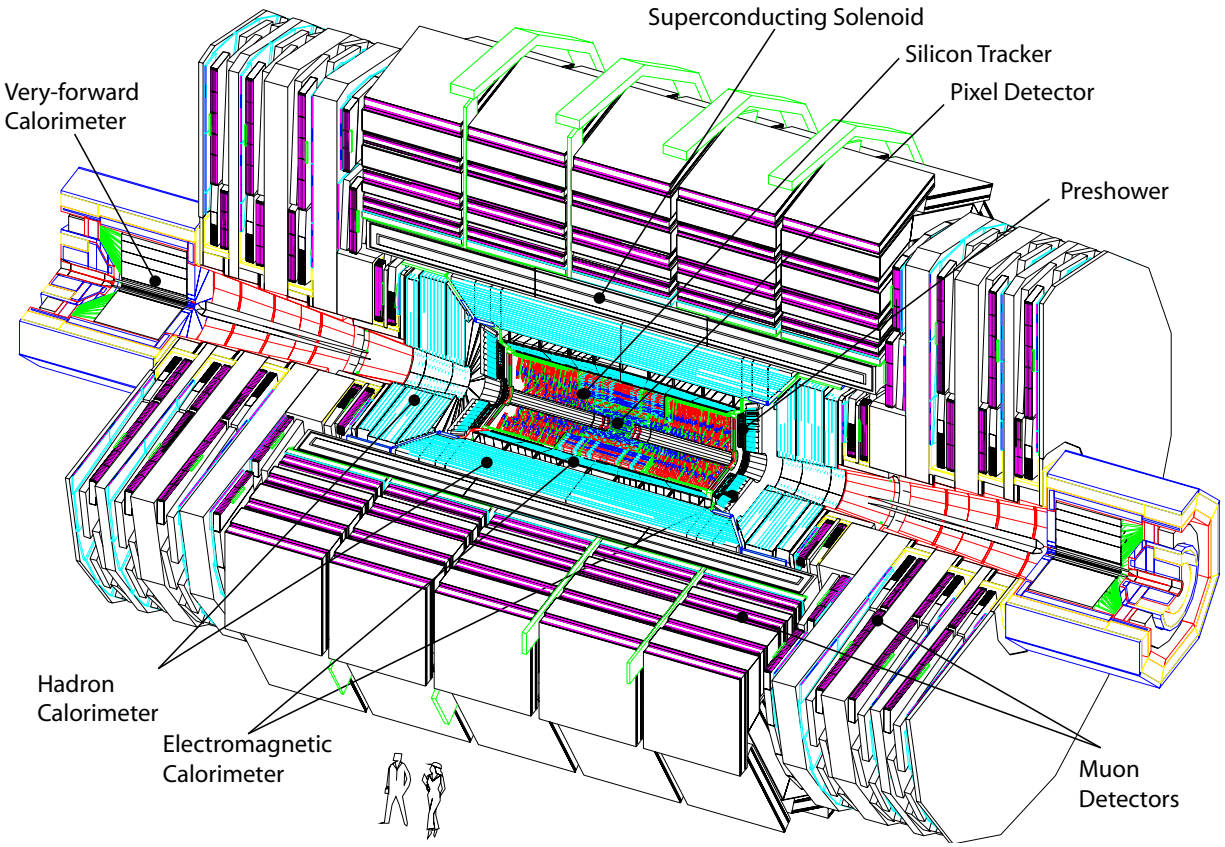

Figure 3.2: Drawing of the CMS detector with its main components [19].

following pages. More details on the reconstruction of physics objects from the detector signals will be given in Chapter 5.

The right-handed coordinate system adopted by CMS has its origin at the nominal collision point, i.e. in the center of the detector. The x axis points radially inwards to the center of the LHC ring, the y axis vertically upwards and the z axis along the anti-clockwise beamline. The azimuthal angle ϕ is measured with respect to the x axis in the (x, y) plane and the polar angle θ with respect to the z axis in the (y, z) plane. The pseudorapidity η, a Lorentz-invariant variable that is often used in preference to the polar angle, is defined as $\eta = -\ln\left(\tan\frac{\theta}{2}\right)$ and the corresponding angular distance is $\Delta R = \sqrt{\Delta\phi^2 + \Delta\eta^2}$.

3.2.1 Magnet

A central feature of CMS is the solenoid that provides a homogeneous field of 3.8 T for the inner detectors. The very strong bending of all charged particles that travel through CMS with a transverse component with respect to the beamline allows an excellent momentum

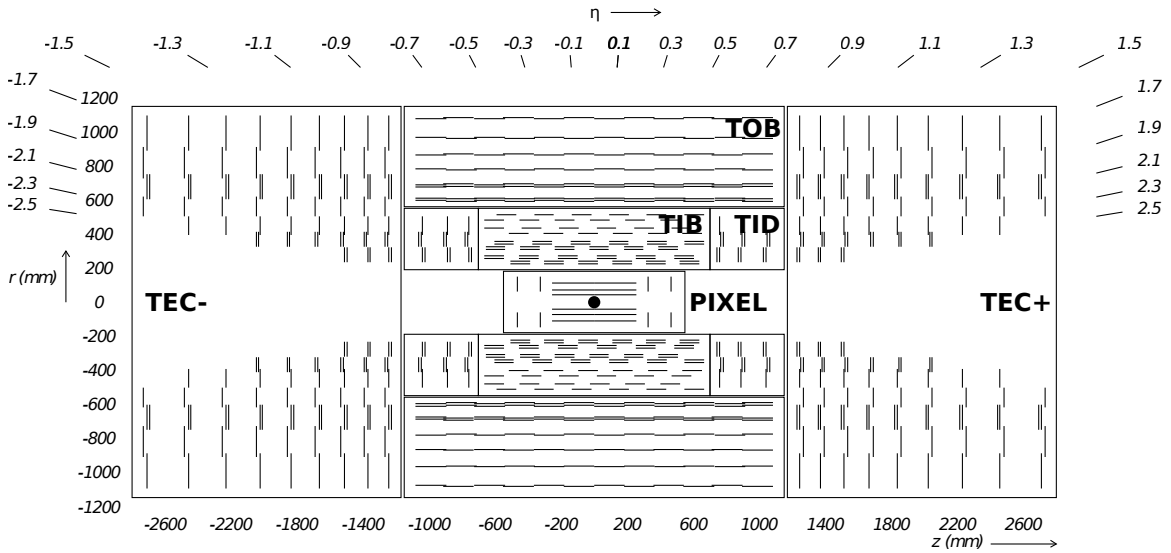

Figure 3.3: Schematic drawing of the inner tracking detectors of CMS in the (y,z) plane [19]. Shown are the pixel detector and the tracker inner barrel (TIB), outer barrel (TOB), inner disks (TID) and endcaps (TEC).

resolution from the measured tracks. The solenoid has a length of 12.5 m and consists in a superconducting coil with an inner diameter of 6 m. The tracker as well as the main calorimeters are located inside the coil. The magnetic flux is returned through a massive iron yoke, which consists of five wheels around the solenoid and two endcaps. The muon detectors are embedded into the return yoke.

3.2.2 Inner tracking detectors

The purpose of the inner tracking system, referred to as the tracker, is to reconstruct the trajectories of all charged particles in the central detector region as precise and efficient as possible. Together with the bending field of the solenoid, this allows to determine particle momenta and charge signs. Furthermore, precisely measured tracks are essential for the reconstruction of interaction vertices.

The CMS tracker consists of the pixel detector, located next to the beampipe, and the surrounding strip detector. The complete tracker is based on semi-conducting silicon as active material. It covers the range of $|\eta| < 2.5$. A sketch of the inner tracking system with the corresponding sub-detectors can be found in Fig. 3.3.

The pixel detector has three concentric cylindrical barrel layers and four disks that close the barrel ends. The barrel layers have an active length of 53 cm and are located at radii of 4.3, 7.3 and 10.2 cm, while the endcap disks are located at longitudinal distances of 35.5

and 48.5 cm from the nominal interaction point and cover the region from 4.8 to 14.4 cm in radius. The active elements are 66 million 100×150 μm pixels, arranged on 1,440 modules. The pixel detector provides typically three hits from tracks with $|\eta| < 2.2$ and two hits from tracks in the region of $2.2 < |\eta| < 2.5$.

The strip detector consists of four subsystems: the tracker inner barrel (TIB), outer barrel (TOB), inner disks (TID) and endcaps (TEC). The active elements are 9.3 million silicon strips, arranged on a total of 15,148 modules. The TIB is located right outside the pixel detector. Both the TIB and the neighboring TID have an outer radius of 55 cm. The TIB has four layers of strips oriented parallel to the beamline, with a strip spacing of 80 μm in the inner pair of layers and 120 μm in the outer pair. The TID has three disks on each side of the TOB and each of these disks three rings. The strips are oriented radially on the rings and have a spacing that varies from 100 to 141 μm. TIB and TID are enclosed in the TOB. The TOB has an outer radius of 116 cm. It has six layers of strips oriented parallel to the beamline and a strip spacing of 183 μm in the first four layers and 122 μm in the outer pair. The TEC covers the region of 124 cm $< |z| <$ 280 cm and radii from 22.0 to 113.5 cm. Each endcap has nine disks and each of these disks up to seven rings with radially oriented strips. The strip spacing varies from 97 to 184 μm. The inner two layers of TIB and TOB, the inner two rings of TID and TEC and the fifth ring of the TEC have a second strip module mounted back-to-back and with a stereo angle of 100 mrad. This allows to measure the orthogonal coordinate (z in the barrel and r in the disks). From tracks with $|\eta| < 2.4$, the strip detector provides typically ≈ 9 hits.

From studies using the detector simulation, the momentum resolution of the tracker in the central η region is expected to range from 1 to 5% at 1 GeV and 1 TeV, respectively, and the impact parameter resolution for high-momentum tracks to be close to 10 μm. The studies performed with the data collected so far suggest a good agreement of the actual with the expected performance of the tracker [20].

3.2.3 Calorimeters

The main subsystems for calorimetry at CMS are the electromagnetic lead-tungstate calorimeter (ECAL) and the surrounding hadronic brass/scintillator calorimeter (HCAL). They provide coverage for $|\eta| < 3.0$. In radiation lengths, the ECAL thickness corresponds to around 25 X_0. The HCAL thickness, depending on η, varies from 7 to 11 nuclear interaction lengths (10 to 15, when including the tail catcher located outside the solenoid).

The ECAL is a homogeneous calorimeter built from lead-tungstate crystals ($PbWO_4$). The layout is shown in Fig 3.4. It consists of a barrel section (EB) and two endcaps (EE). In front of the EE, there is a special sampling calorimeter consisting of two layers of silicon sensors interleaved with lead absorbers, which have a total thickness of 3 X_0. Main purpose of this preshower detector is the discrimination of closely spaced photon pairs, typically

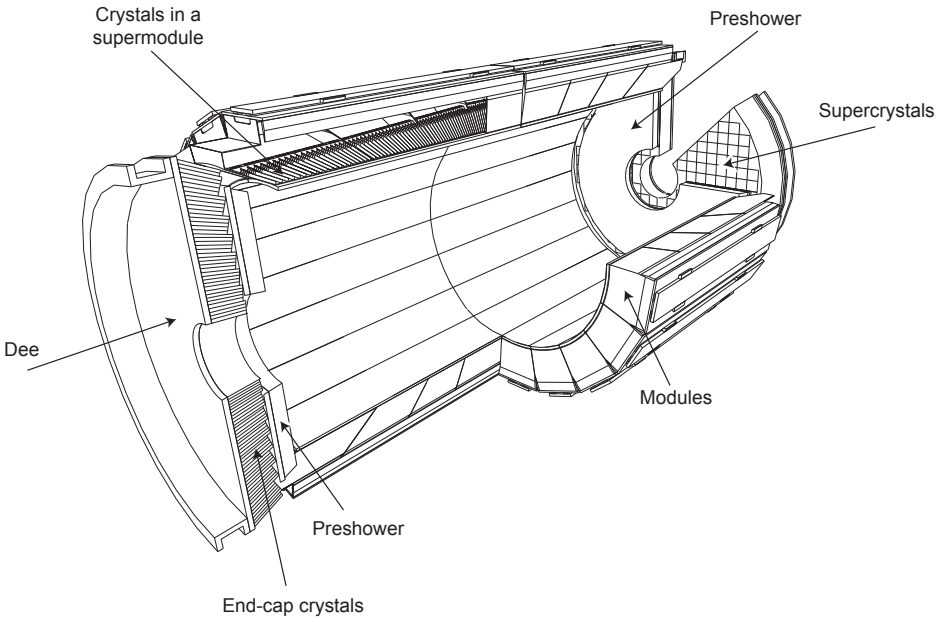

Figure 3.4: Layout of the electromagnetic calorimeter of CMS [19].

emerging as decay products of π^0 mesons within jets, from single photons.

The EB has an inner radius of 129 cm, covers the region of $|\eta| < 1.5$ and contains 61,200 crystals. The crystals in the EB have a size of 0.087×0.087 in (η, ϕ), i.e. 1° in ϕ, corresponding to 22×22 mm^2 at the front face and 26×26 mm^2 at the rear. They are arranged in a quasi-projective geometry. A small tilt of their axes with respect to the direction to the nominal interaction point is introduced in order to minimize the number of particle trajectories going along cracks between the crystals. The EB crystals are arranged in 36 identical so-called supermodules, each extending over half the barrel length and 20° in ϕ and containing 1,700 crystals. The two endcaps have a distance of 314 cm to the nominal interaction point and cover the region of $1.5 < |\eta| < 3.0$. Each endcap has 7,324 crystals and is subdivided into a pair of dees. The EE crystals have a size of 29×29 mm^2 at their front and 30×30 mm^2 at the rear, are tilted by 2 to 8° with respect to the direction to the interaction point and grouped in structures of 5×5 crystals, sometimes referred to as supercrystals. The crystal length is 23.0 cm in the EB and 22.0 cm in the EE, which corresponds to 25.8 and 24.7 X_0, respectively. The scintillation light emitted in the crystals is detected by silicon avalanche photodiodes in the EB and vacuum phototriodes in the EE.

Prior to their integration into the CMS detector, the energy resolution of ECAL supermodules was measured to be:

$$\frac{\sigma(E)}{E} = \frac{2.8\%}{\sqrt{E/\mathrm{GeV}}} \oplus \frac{12\%}{E/\mathrm{GeV}} \oplus 0.3\% \tag{3.3}$$

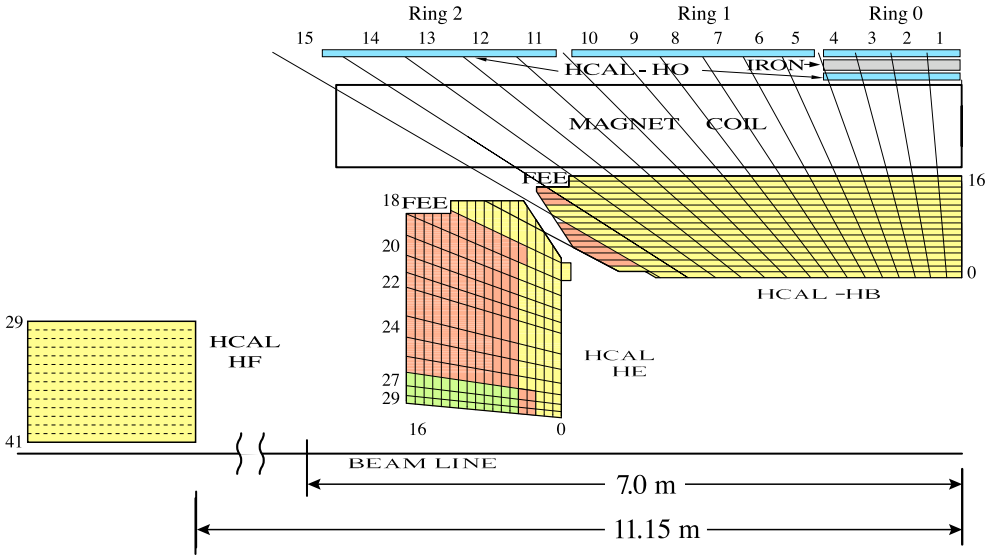

Figure 3.5: Layout of the hadronic calorimeter of CMS [22]. Shown is a quarter slice with the corresponding barrel (HB), endcap (HE), outer (HO) and forward (HF) subdetectors and the location of front-end electronics (FEE) for the readout of HB and HE.

The first term corresponds to a stochastic and the second to a noise term. The third is a small constant term, which dominates the resolution at high energies. The above numbers were obtained in the absence of a magnetic field and with an electron beam directed to the central crystal of the supermodule. However, studies based on the first 250 nb^{-1} of data collected at $\sqrt{s} = 7$ TeV already showed that the actual energy scale of the ECAL agrees with the expectation within 1% in the barrel and 3% in the endcaps [21].

As shown in Fig 3.5, the HCAL comprises four different subsystem: the hadronic barrel (HB), endcap (HE), outer (HO) and forward (HF) calorimeters. The HO, located between solenoid and muon system, can be employed to catch energy leakage from the HB. It has not been used within this thesis.

The HB fills up the space between the EB and the solenoid and covers the range of $|\eta| < 1.4$, while the HE occupies the space between the EE and the endcaps of the return yoke and covers $1.3 < |\eta| < 3.0$. HB and HE are sampling calorimeters built from brass as absorber and plastic scintillator as active material. The first scintillator layer, located next to the ECAL, has a thickness of 9 mm. The thickness of the other scintillator layers is 3.7 mm each. The brass absorber plates have a thickness of about 5 cm in the HB and 8 cm in the HE. The scintillation light is converted by wavelength-shifting fibers, which are embedded in the scintillator modules, and sent to hybrid photodiodes through clear fibers. The HCAL is subdivided into towers that project radially outwards with respect to the nominal interaction point. These towers have a size of 0.087×0.087 in (η, ϕ), except for some HE towers at high $|\eta|$, where the size goes up to 0.35 in η and 0.175 in ϕ. Each HB and HE tower maps exactly to a specific array of ECAL crystals.

The HF is an iron/quartz-fiber calorimeter placed at a distance of 11.2 m from the nominal interaction point. It provides coverage for $3.0 < |\eta| < 5.2$. Inner and outer radii of the HF are 12.5 and 130.0 cm, respectively. The quartz fibers have a diameter of less than 1 mm and are aligned parallel to the beamline. Cerenkov light is emitted by charged showers in the fibers and detected by photomultipliers. Half of the fibers run through the full 165 cm of the iron absorber, while the other half starts at a depth of 22 cm from the front face. This allows to distinguish hadronic from electromagnetic showers, since the latter typically deposit most of their energy within the first centimeters of the absorber. The HF readout segmentation is 0.175×0.175 in (η, ϕ), except for the towers with highest $|\eta|$, which have a size of 0.3 in η and 20° instead of 10° in ϕ.

3.2.4 Muon system

As shown in Fig. 3.6, the muon system, embedded into the return yoke, is subdivided into four so-called muon stations. Each station consists of a combination of gas-ionization detectors: drift tubes (DTs) or cathode strip chambers (CSCs) in the barrel and endcaps, respectively, complemented by resistive plate chambers (RPCs) in both regions. The muon system is not only crucial for the identification of muons and for momentum measurements with a long lever arm on muon tracks. It also provides fast and highly-efficient measurements for muon based trigger algorithms.

The DTs cover the region of $|\eta| < 1.2$ and are aligned parallel to the beamline. In each station, there are eight DT chambers that measure the muon coordinate in the (r, ϕ) plane. In each of the first three stations, there are four additional DT chambers that provide a measurement in the z direction. The CSCs cover the region of $0.9 < |\eta| < 2.4$. They are aligned perpendicular to the beamline. Their cathode strips run radially outwards with respect to the nominal interaction point and provide a measurement in the (r, ϕ) plane. The anode wires run approximately perpendicular to the cathode strips and provide additional information on the muon η. The RPCs cover the region of $|\eta| < 1.6$. They are operated in avalanche mode and provide good timing information but a less precise position measurement compared to DTs and CSCs. Most muon stations contain one RPC layer, but there are two RPC layers in the first two stations in the barrel, which allows triggers based on the muon system to work even for low-momentum muons that do not reach the last two stations.

3.2.5 Luminosity monitoring

The instantaneous luminosity can be determined by measuring the rate of events from a process with known cross section (cf. Eq. 3.1). The total rate of inelastic pp collisions is currently used at CMS to measure the luminosity delivered by the LHC [24].

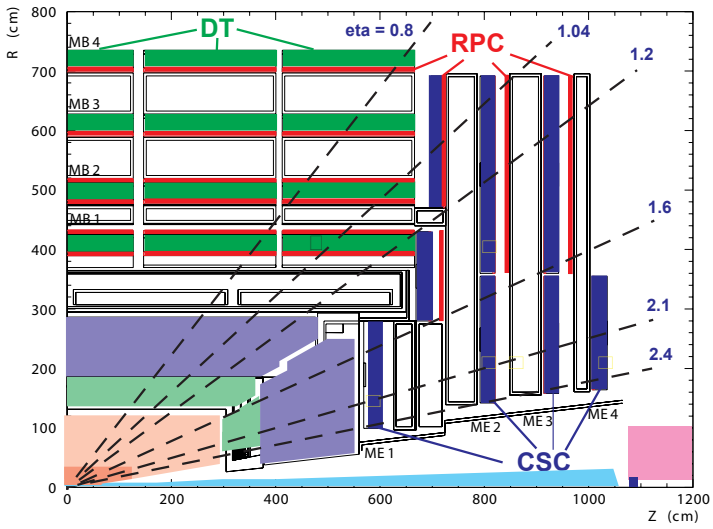

Figure 3.6: Layout of the muon system of CMS [23]. Shown is a quarter slice with the drift tube chambers (DT), cathode strip chambers (CSC) and resistive plate chambers (RPC). The labels MB and ME refer to stations of the muon barrel and endcap system, respectively.

The number of interactions per bunch crossing, n, is distributed around the mean value μ following Poisson statistics:

$$P(n) = \mu^n \frac{\exp(-\mu)}{n!} \tag{3.4}$$

Given that it is typically not possible to reliably distinguish if there was a single interaction or if there were multiple interactions in a given bunch crossing, while it is easier to distinguish between zero and one or more interactions, the mean number of interactions per bunch crossing is often determined from so-called zero counting, i.e. inverting Eq. 3.4 to obtain:

$$\mu = -\ln P(0) \tag{3.5}$$

The instantaneous luminosity is measured online at CMS using signals from the HF calorimeters. Two methods are employed. One is based on zero counting and uses the average fraction of empty towers. The other is based on a linear correlation of the average transverse energy per tower with the number of interactions per bunch crossing. A pedestal subtraction is done using the average noise from empty bunch crossings and the residual level coming from beam-gas interactions and beam scraping is estimated using unpaired bunches, which pass without colliding with a bunch from the opposite beam.

One offline method is based on coincidental energy depositions in the HF calorimeters on both sides of CMS. A summed transverse energy of at least 1 GeV is required on each side. Timing criteria are imposed to eliminate non-collision background. Another offline method requires per collision at least one vertex reconstructed from at least two tracks.

The longitudinal positional of this vertex is required to lie within $|z| < 15$ cm. Both offline methods estimate the average number of events per bunch crossing via zero counting.

For the 2010 data, a good consistency was found between the online and offline luminosity measurements and the final accuracy was estimated to be 11%.

3.2.6 Trigger and data acquisition

The CMS trigger and data acquisition system consists of four parts: the detector electronics, the hardware-based "level-1" (L1) trigger, the readout network and the software-based high-level trigger (HLT). Data from only about 10^2 events per second can be written to archival media, while the actual interaction rate at the LHC is higher by many orders of magnitude. Triggers are therefore needed that reject the vast majority of events but efficiently select the most interesting interactions. The CMS trigger system was designed to achieve a rejection factor of $1/10^6$.

The hardware logic of the L1 trigger processes information with reduced granularity from the calorimeters and the muon system. Decisions are taken based on global energy sums or the presence of primitive candidates for objects like photons, electrons, muons and jets. Parts of the L1 electronics are directly mounted on the corresponding subdetectors, while other parts are installed in an underground control room at a distance of about 90 m from the experimental cavern. The time allocated for the L1 trigger is 3 μs. During this time, which also includes the transit of signals to the service cavern and finally the distribution of the L1 trigger decision back to the front-end electronics, the full detector data from the corresponding bunch crossing has to be buffered. Pipelined memories at the front-end electronics allow almost dead-time-free data taking. The design output rate limit of the L1 trigger is 100 kHz. During operation, trigger settings are adopted to the instantaneous luminosity in order to optimize the usage of the data throughput capacity. CMS has defined the so-called luminosity section as a time interval of 93 s (corresponding to 2^{20} LHC orbits) during which trigger settings may not change. Variations of the bunch crossing rate within one luminosity section can cause data-taking dead time.

The HLT is an online event filter system with access to the information of all subdetectors with full granularity. It consists in a farm of processor units running in parallel a software that performs complex calculations similar to those made in the offline event reconstruction. The HLT has to achieve the final event output rate of 100 Hz for mass storage.

Chapter 4

Event Simulation

For the analysis presented in this thesis, the simulation of $t\bar{t}$ production and decay is based on the Monte Carlo matrix-element generator MadGraph [25], including top quark pairs in association with up to three jets from additional light quarks and gluons. The top quark mass is set to 172.5 GeV as central value but events generated with top quark masses of 166.5 and 178.5 GeV will also be used in the following for generating mass templates. For the simulation of initial- and final-state radiation and hadronization, the hard processes generated with MadGraph are passed on to the Monte Carlo generator Pythia [26]. The matching of parton showers from Pythia to the matrix elements is done using the MLM algorithm [27]. Concerning the simulation of the so-called underlying event, consisting mainly of particles that originate from the beam remnants or from interactions of secondary parton pairs and that accompany the primary hard parton scattering, the Pythia tune D6T [28] was chosen. In order to study the impact of changes in the underlying-event settings, the results obtained with D6T will be compared to results obtained with the tune Z2 [29]. All simulated events are passed through a full simulation of the CMS detector based on Geant4 [30] and finally through the same reconstruction software as the data.

The electroweak production of single top quarks is considered as a background for the analysis presented here. The production of W and Z bosons in association with additional hard jets, in the following sometimes referred to as W+jets and Z+jets, can also have a similar signature as $t\bar{t} \to (b\mu\nu)(bqq')$ if the vector boson decays leptonically. Due to the relatively small cross sections, s-channel production of single top quarks as well as diboson production are neglected in this thesis. Events with single top quarks from t-channel production and from the associated production of a single top quark and a W boson as well as $W \to l\nu$ and $Z/\gamma* \to l^+l^-$ events are generated using again MadGraph in combination with Pythia. The production of up to four additional jets on matrix-element level is simulated in these cases. Samples with events from QCD multijet production are generated using Pythia directly. Here, hard muons typically emerge from decays of b and c quarks and from the decay of K and π mesons in flight. For technical reasons, the

Table 4.1: Cross sections computed in NLO and NNLO using MCFM and FEWZ, respectively. The given uncertainties include the uncertainties due to the factorization and renormalization scales as well as the uncertainties on the PDFs and on α_s.

	$t\bar{t}$	t-channel single top	Associated tW	$W \to l\nu$	$Z/\gamma* \to l^+l^-$ ($m_{ll} > 50$ GeV)
Cross section	158^{+23}_{-24} pb	$64.6^{+3.4}_{-3.2}$ pb	10.6 ± 0.8 pb	31.3 ± 1.6 nb	3.05 ± 0.13 nb
Order	NLO	NLO	NLO	NNLO	NNLO

single-top and QCD multijet samples were not generated with the tune D6T but only with Z2. This inconsistency is assumed to have no significant effect on the results of the analysis presented here.

Within the CMS Collaboration, the parton-level integrator MCFM [31] has been employed to compute next-to-leading order (NLO) cross sections for the production of top quark pairs and single top quarks, using a top quark mass of 172.5 GeV to be consistent with the event simulation described above, while FEWZ [32] has been used to compute next-to-next-to-leading order (NNLO) cross sections for $W \to l\nu$ and $Z/\gamma* \to l^+l^-$. The results, listed in Table 4.1, are used in this thesis for the corresponding processes to normalize the event rates predicted by the leading-order (LO) Monte Carlo generators. For the background from QCD multijet production, the plain LO prediction from the Monte Carlo generator is used due to the lack of a better estimate for the corresponding cross section. Pythia finds a cross section of 80 nb for QCD multijet events that have a final-state muon with a p_T of at least 15 GeV on generator level.

Chapter 5

Event Reconstruction and Selection

The analysis presented here includes the full dataset from pp collisions at $\sqrt{s} = 7$ TeV recorded by the CMS detector in the year 2010. There are three different periods of data taking relevant for this thesis. They are summarized in Table 5.1. While an integrated luminosity of 47.0 pb^{-1} was delivered by the LHC (cf. Fig. 3.1), only 43.2 pb^{-1} could be recorded by CMS and 35.9 pb^{-1} were declared as good for analyses, i.e. without problems in any of the relevant CMS subsystems.

The experimental signature of a $t\bar{t} \rightarrow (b\mu\nu)(bqq')$ event consists in a muon, missing transverse energy, $\not\!\!E_T$, from the neutrino, which escapes undetected, and four jets from the hadronization of the four quarks. Additional jets can be produced by higher-order radiation. The criteria used for the selection of physics objects and events in this thesis are based on those developed within the CMS Top Quark Physics Analysis Group as reference selection for the muon+jets topology and employed also for the first cross-section measurement in this channel [33]. Events are required to have exactly one isolated high-momentum muon, no isolated electron and at least four jets. No requirements are imposed on the reconstructed $\not\!\!E_T$. The only difference between the criteria in [33] and the event selection chosen for this thesis is that in the following two jets per event are required to be

Table 5.1: Data-taking periods from the year 2010 used in this analysis, listed together with the corresponding ranges of run numbers, trigger thresholds on the muon p_T and integrated luminosities.

Period	Run numbers	Trigger threshold	Luminosity
May 22nd - August 30th	136035 - 144114	9 GeV	3.16 pb^{-1}
September 22nd - October 3rd	146428 - 147116	9 GeV	5.02 pb^{-1}
October 4th - October 29th	147196 - 149294	15 GeV	27.71 pb^{-1}

identified as jets from the decay of b quarks. Further details of the selection criteria are given in the following sections together with a description of the involved reconstruction algorithms.

5.1 Trigger

The triggers used in this analysis require at least one high-momentum muon. No requirements on the isolation of the muon candidate are made at this stage. Muon reconstruction for the HLT consists of several steps [34]. An L1 trigger object is taken as a seed for the reconstruction of a track in the muon system. Then tracks are reconstructed in the silicon tracker in the region around the direction of the track from the muon system. Finally, if a tracker track can be matched to the muon track, a global track fit is performed that combines the hits in the silicon tracker and those in the muon system.

For the analysis presented here, a trigger with a muon p_T threshold of 9 GeV was used for the online event selection during the first two periods of data taking defined in Table 5.1. Then, given the increased instantaneous luminosity, a trigger with a 15 GeV threshold was employed.

5.2 Vertex

The reconstruction of primary vertices from pp interactions [20] is based on tracks that are clustered according to their z position with respect to their distance of closest approach to the beamline. Within an adaptive vertex fitting procedure, the tracks are assigned weights between 0 and 1 based on their proximity to the fitted vertex. Events are ensured to have a well reconstructed primary vertex by requiring the vertex to yield ndof > 4, where ndof corresponds to the summed weights of the tracks associated to the vertex, and to be in the central detector region of $|z| < 24$ cm and $\rho < 2$ cm around the nominal interaction point. In this analysis, only the vertex with the highest scalar sum of track p_T is considered in each event.

5.3 Muons

There are three different algorithms for the offline reconstruction of muon candidates at CMS [34]. The first algorithm is based exclusive on the recorded signals in the muon system:

1. So-called *standalone muons* are reconstructed starting from the track segments detected in the innermost muon chambers. Hits in neighboring layers are added in a Kalman filter fit. The resulting muon track is finally propagated back to the interaction point.

The other two algorithms combine the signals in the muon system with hits in the silicon tracker, either in an outside-in or an inside-out approach:

2. *Global muons* are reconstructed using the same logic as already employed for muons at HLT level, i.e. matching tracks in the silicon tracker to a standalone muon and then performing a combined fit that includes both the corresponding hits in the muon system and those in the silicon tracker.

3. The reconstruction of *tracker muons* starts with the tracks in the silicon tracker and extrapolates them to the muon system, taking into account the expected energy loss and the uncertainty due to multiple scattering.

For the analysis presented here, muons are required to be found both as tracker and as global muon candidates and reconstruction quality criteria are imposed on these candidates. The track of the tracker muon is required to be reconstructed from at least 11 hits, the global muon to have matched segments from at least two muon stations and the global muon track fit to have a normalized χ^2 smaller than 10. The muons are required to have in impact parameter d_0 with respect to the beam spot of $|d_0| < 0.02$ cm and a longitudinal distance to the primary vertex of $\Delta z < 1$ cm. In order to select muons from leptonic W decays and no muons from decaying b or c quarks, they are required to appear well separated from other objects in the detector. Isolation variables trkIso and calIso are calculated by summing within a cone of $\Delta R < 0.3$ around the muon all track p_T and calorimeter energies, respectively, excluding the muon track and energy depositions within $\Delta R < 0.007$. A combined relative isolation, relIso, is then calculated as the sum of both divided by the muon p_T:

$$\text{relIso} = \frac{\text{trkIso} + \text{calIso}}{p_T} \tag{5.1}$$

In this analysis, muons are required to have relIso < 0.05 and to be separated by $\Delta R > 0.3$ from any jet reconstructed and selected as described in Sec. 5.5.

As event selection criterion, one muon passing the above muon selection and having $p_T > 20$ GeV with $|\eta| < 2.1$ is demanded. Furthermore, there is a veto on additional muons, using a rather loose muon selection: There shall not be a second global muon with $p_T > 10$ GeV, $|\eta| < 2.5$ and relIso < 0.2 in the event.

5.4 Electrons

At CMS, electrons are reconstructed combining signals measured in the tracker and the electromagnetic calorimeter. A description of the involved algorithms can be found elsewhere [35]. For the analysis presented here, events that contain isolated hard electrons are rejected by simply imposing a veto on any electron candidate with $E_T > 15$ GeV, $|\eta| < 2.5$ and relIso < 0.2, where relIso is defined analogously as for the muons in Sec. 5.3.

5.5 Jets

5.5.1 The particle-flow algorithm

In this thesis, particle-flow jets are used. The particle-flow algorithm [36] combines the different CMS sub-detectors with the aim of achieving a complete reconstruction of all stable particles in the event, identifying them as muons, electrons, photons, charged or neutral hadrons. The large silicon tracker within the strong magnetic field of the coil and the high granularity of the electromagnetic calorimeter with its excellent energy resolution are two characteristics of CMS that are essential for the particle-flow algorithm. The reconstruction of photons, including their separation from electrons, is completely based on the high angular and energy resolution of the electromagnetic calorimeter. Charged and neutral hadrons deposit most of their energy in the hadronic calorimeter, which provides only a relatively coarse angular and energy resolution. Not only the identification but also the reconstruction of charged hadrons is thus based on the information from the silicon tracker, while neutral hadrons are detected as an energy excess on top of the energy deposited by the charged hadrons pointing to the same calorimeter cells. The list of particle candidates resulting from the particle-flow reconstruction is finally taken as input for the jet clustering.

5.5.2 The anti-k_T algorithm

The anti-k_T jet algorithm [37] with a size of $R = 0.5$ is used for the analysis presented here. This jet algorithm successively clusters objects i and j according to

$$d_{ij} = \min(1/k_{T,i}^2, 1/k_{T,j}^2) \cdot \left((y_i - y_j)^2 + (\phi_i - \phi_j)^2\right)/R^2 \tag{5.2}$$

as long as d_{ij} is smaller than $1/k_{T,i}^2$, where y and ϕ are rapidity and azimuth and k_T is the transverse momentum. The anti-k_T algorithm is infrared and collinear safe, i.e. the result would not change neither if an infinitesimally small amount of energy was added to the final state nor when replacing two collinear objects by a single one with the same total

momentum. This is not only significant for the cancellation of divergences in perturbative calculations; from an experimental point of view, it guarantees that the result does not exceedingly depend on the detection of particles from soft radiation and that the result is largely independent of the granularity of the detector. In addition to this, the anti-k_T algorithm provides jets with regular boundaries and a shape very similar to a simple cone of size R, even in the presence of soft radiation. Such jet shapes, which are not among the characteristics of other infrared and collinear safe algorithms, can partially simplify, for example, the experimental jet energy calibration.

5.5.3 Jet energy corrections

When using simulated events to compare jets clustered from stable particles, i.e. at the level of hadrons, to jets reconstructed from the corresponding detector signals, one finds that the reconstructed systematically deviates from the true energy. The main reason is the non-uniform and non-linear response of the CMS calorimeter. CMS has adopted a factorized approach to calibrate jet energies for this as well as for several additional effects [38]. The default corrections are multiplicative factors as a function of the jet p_T and η and currently derived from QCD multijet events in pp collisions generated with the Pythia Monte Carlo program and passed through the full GEANT detector simulation. For particle-flow jets with $p_T > 30$ GeV, the correction factors are typically between 1.0 and 1.1 [39], while they are much larger for jets reconstructed from calorimeter information only. A validation of the jet energy corrections in simulated $t\bar{t}$ events together with a short discussion of flavor dependent effects will be given in Chapter 6.

Small residual corrections are applied to account for discrepancies between the jet response observed in data and the simulated jet response. These residual corrections [40] were determined from p_T balance in dijet events, which were used to measure the jet response as a function of η, relative to the reference region of $|\eta| < 1.3$, and from photon+jet events, which allowed to measure the absolute jet energy scale as a function of p_T in the central detector region. The combined factors for the residual correction are independent of the jet p_T and between 0.98 and 1.03 for jets with $|\eta| < 2.4$.

5.5.4 Jet selection

A series of quality criteria are imposed in order to identify real hadronic jets, rejecting fake jets from instrumental noise. Jets are required to have:

- at least two constituents
- at least one charged constituent

- charged hadronic energy fraction > 0
- neutral hadronic energy fraction < 0.99
- charged electromagnetic energy fraction < 0.99
- neutral electromagnetic energy fraction < 0.99

Finally, only events are selected that have at least four jets with $p_T > 30$ GeV and $|\eta| < 2.4$.

5.5.5 Identification of jets from b quarks

Jets arising from the hadronization of b quarks significantly differ from jets arising from light quarks or gluons. The main differences are due to the relatively large mass and the long lifetime of the corresponding hadrons, which result in several characteristic signatures that can be used to identify b jets in the detector. Different algorithms for b tagging have been developed and commissioned for CMS [41, 42]. In this thesis, the "simple secondary vertex" (SSV) algorithm is employed. The lifetime of the hadrons from b-quark fragmentation results in decay lengths of up to several mm. This allows for the reconstruction of a secondary vertex, spatially separated from the vertex of the primary parton-parton scattering. In its so-called high-efficiency version, the SSV tagger requires the reconstruction of a secondary vertex with at least two tracks assigned to it. The significance of the three-dimensional flight distance is taken as the b discriminator for the SSV tagger. The discriminator distributions for b jets and for non-b jets is shown in Fig. 5.1 together with the resulting b-tagging efficiency and mis-tag rate as a function of the cut on the discriminator. Within the limited statistics for b jets in the W+jets samples used for this thesis, there are no differences between the b-tagging efficiencies and mis-tag rates for jets in $t\bar{t}$ and $W \to l\nu$ events. For the analysis presented in the following, jets with a discriminator value larger than 1.74 are taken as b jets. This cut value corresponds to the so-called "medium" working point of the high-efficiency SSV tagger. As shown in Fig. 5.1, a b-tag efficiency of around 60% and a mis-tag rate in the order of 5% are found for jets with $p_T > 30$ GeV in simulated $t\bar{t}$ events. Based on the high acceptance and efficiency of muon reconstruction at CMS, one can use semileptonic decays of b hadrons to measure b-tagging efficiencies in data. With this technique, a scale factor of $0.97 \pm 0.04(\text{stat}) \pm 0.19(\text{syst})$ was determined to account for the difference between the b-tagging efficiency of the SSV algorithm at the medium working point in data and simulation [42]. The second error given on this value corresponds to a preliminary estimate of the systematic uncertainty. The scale factor of 0.97 has been nicely conformed for the $t\bar{t}$ topology within a cross section measurement in the lepton+jets channel [43]. To be conservative, the original 19% uncertainty will still be used for the measurement presented in this thesis. This uncertainty one the b-tagging scale factor can be translated into an 11% uncertainty on a b-tagging efficiency of 60%.

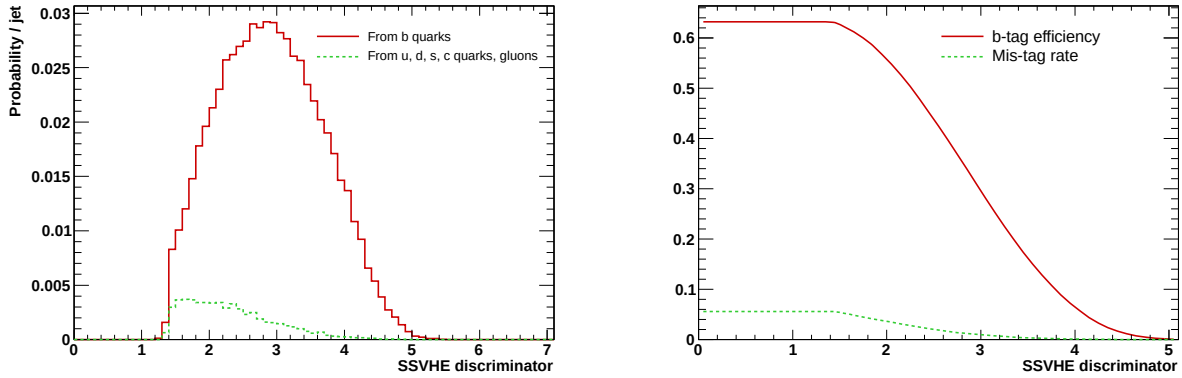

Figure 5.1: Distribution of the b discriminator from the high-efficiency version of the "simple secondary vertex" algorithm (SSVHE) for b jets and non-b jets (left) and the resulting b-tagging efficiencies and mis-tag rates (right). These distributions were obtained using jets with $p_T > 30$ GeV in simulated $t\bar{t}$ events. The low number of entries visible for non-b jets on the left side is due to the fact that typically no appropriate secondary vertex is found for these jets.

Table 5.2: Expected event yields and relative contribution of the different processes after the final selection step for an integrated luminosity of 35.9 ± 1.4 pb^{-1}. The uncertainties account for the statistics of the simulated samples and for a 4% uncertainty on the luminosity but not for cross section uncertainties.

Total	$t\bar{t}$	Single t	Assoc. tW	$W \to l\nu$	$Z/\gamma* \to l^+l^-$	QCD
69.9 ± 2.7	65.8 ± 2.7	1.7 ± 0.1	1.0 ± 0.1	1.0 ± 0.3	0.3 ± 0.1	0.2 ± 0.1
(100%)	(94.1%)	(2.4%)	(1.4%)	(1.5%)	(0.4%)	(0.3%)

5.6 Selected Sample

Requiring a well reconstructed pp interaction vertex, exactly one isolated high-momentum muon, no isolated electron and at least four jets as defined above, exactly two of them identified as b jets, results in 78 selected events from the available 35.9 pb^{-1} of data. Table 5.2 lists the expected event yields from the different relevant processes. The expected event yields include a scale factor of 0.965 to correct them for the actual muon trigger, identification and isolation efficiencies observed in data [33]. The total $t\bar{t}$ acceptance and selection efficiency is expected to be approximately 1%.

It can be seen from Table 5.2 that the expected $t\bar{t}$ fraction after the last selection step is 94.1%. An uncertainty of 1.1% on the $t\bar{t}$ fraction arises from the finite statistics of the simulated samples and from the uncertainty on the luminosity. Assuming a conservative

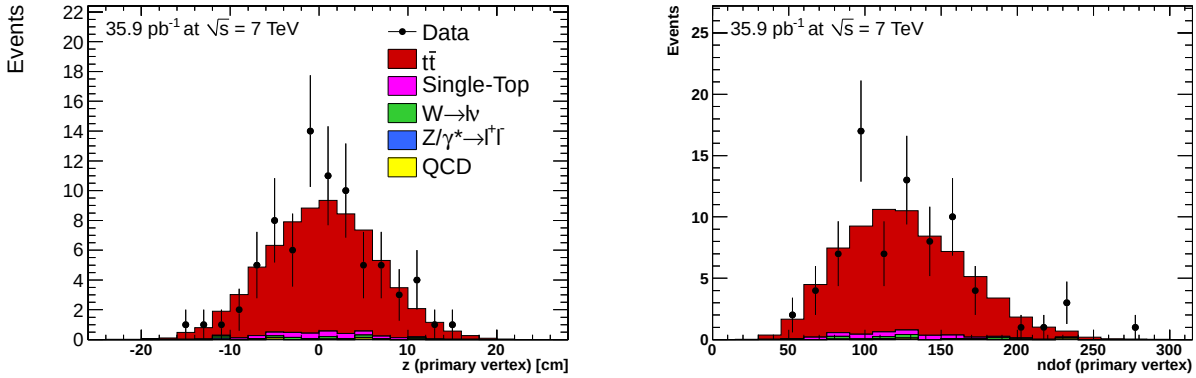

Figure 5.2: Longitudinal position (left) and number of degrees of freedom (right) of the primary vertex after the final event selection.

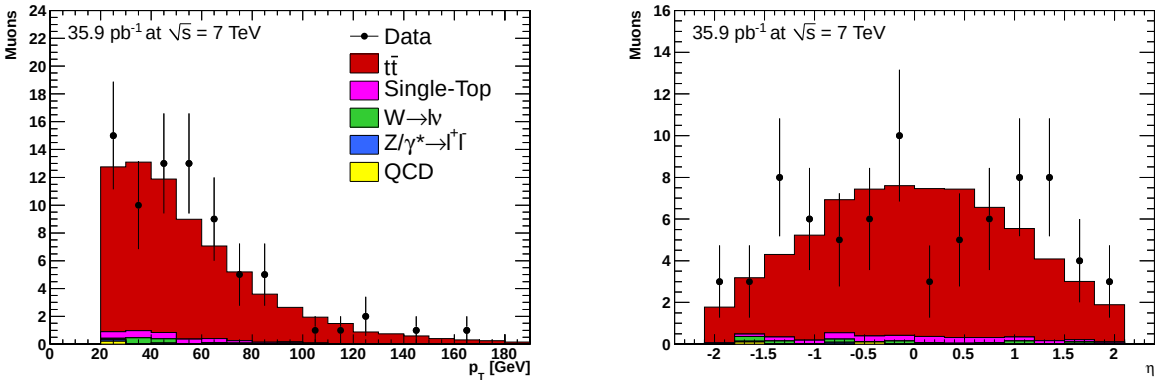

Figure 5.3: Muon transverse momentum (left) and pseudorapidity (right) after the final event selection.

uncertainty of 50% on the event yields for $t\bar{t}$, single-top, $W \rightarrow l\nu$ and $Z/\gamma* \rightarrow l^+l^-$ and an uncertainty of 100% for QCD, results in an uncertainty of 3.4% for the $t\bar{t}$ fraction. 88% of the selected $t\bar{t}$ events are expected to decay in the muon+jets channel.

The primary vertex z and ndof distributions after the final event selection can be found in Fig 5.2 and the muon p_T and η distributions in Fig. 5.3. Figure 5.5 shows the jet multiplicity, p_T and η, while the variables used for the jet identification are shown in Fig. 5.6. The distribution of the b discriminator and the multiplicity of b jets are shown Fig. 5.4. Apart from the fact that the total event rate is slightly lower in simulation than in the data, the overall description of the shape of the distributions in data by the simulation is reasonable. The largest discrepancy is observed for the muon η.

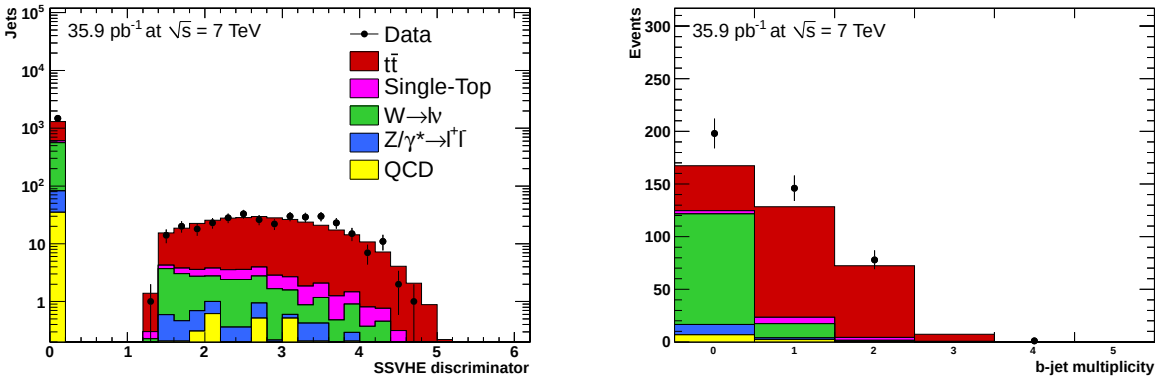

Figure 5.4: The b discriminator from the high-efficiency version of the "simple secondary vertex" algorithm (SSVHE) is shown on the left, while the multiplicity of jets with a discriminator value larger than 1.74 is shown on the right. Note that these distribution are obtained from the sample of 423 events before demanding two b-tagged jets.

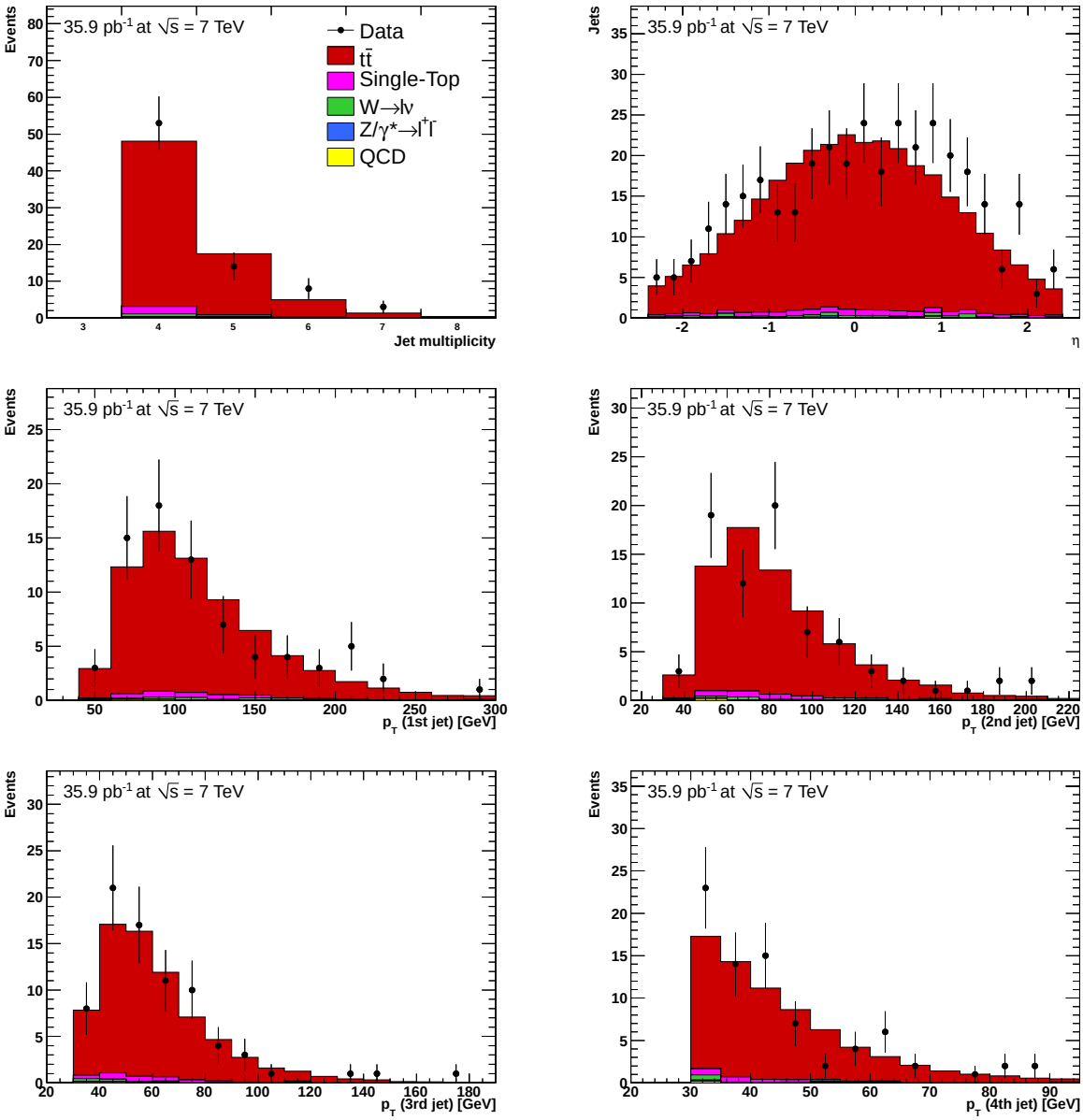

Figure 5.5: Jet multiplicity (first row, left), pseudorapidities (first row, right) and the transverse momenta of the 1st, 2nd, 3rd and 4th leading jet (second row left to third row right) after the final event selection.

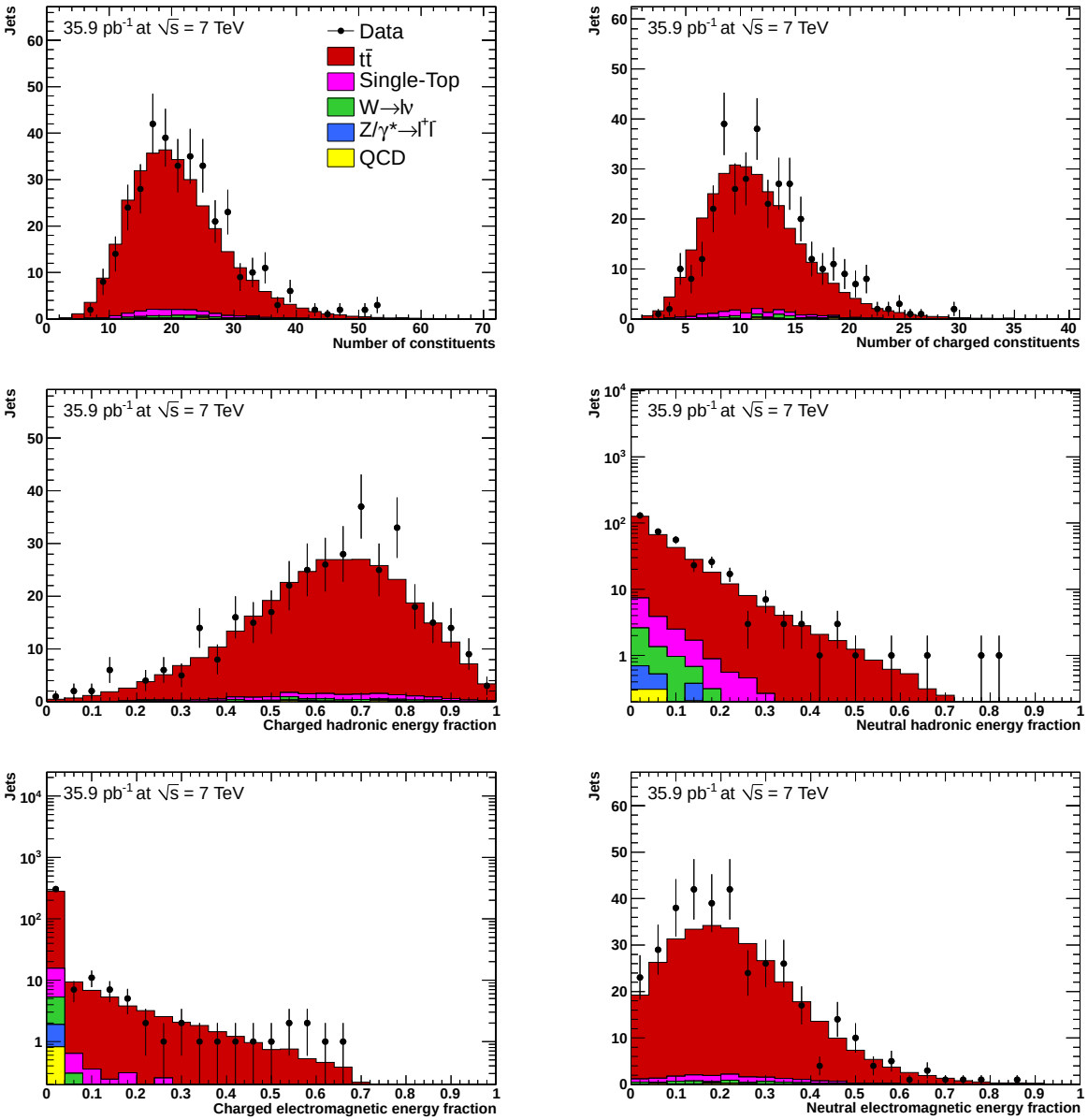

Figure 5.6: In the first row, the number of all jet constituents (left) and of charged constituents (right) is shown. The fraction of jet energy carried by charged (left) and neutral (right) hadrons is shown in the second row. The charged (left) and neutral (right) electromagnetic jet energy fractions can be found in the third row.

Chapter 6

Study of the Jet Energy Scale in Simulated Events

6.1 Resolution Bias

The energy spectrum of particles is typically not flat and thus a finite energy resolution leads to net migrations from higher populated to less populated energy bins. In addition to this, any selection cut performed on the energy, e.g. on the reconstructed jet p_T, introduces a shift of the apparent energy scale due to the finite resolution, as true values below the cut but reconstructed above are selected while true values above the cut and reconstructed below are lost. These are two different effects that depend on the energy resolution and which both introduce a bias in the effective energy scale even for a perfect calibration.

A simple toy model is used here to study the energy resolution related effects and to derive a quantitative estimate for the resulting bias. From hadronically decaying top quarks in the default simulation of $t\bar{t}$ events (cf. Chapter 4), the b quark and the two quarks from the W boson are taken if their pseudorapidity lies within $|\eta| < 2.4$. The energies of these partons are then smeared according to a Gaussian distribution having a width σ that corresponds to the actual jet energy resolution at CMS. This energy resolution, which depends on both the energy and on η, can be parametrized as a function of p_T in bins of η [44]:

$$\frac{\sigma(p_T)}{p_T} = \sqrt{\mathrm{sgn}(N)\left(\frac{N}{p_T}\right)^2 + S^2 \cdot p_T^{(M-1)} + C^2} \tag{6.1}$$

The parameters N, S and C characterize the noise, stochastic and constant term, respectively. The additional parameter M is introduced to better describe the low-p_T resolution for jets that include tracking information. The actual values of N, S, C and M that are used in this thesis are listed in Table 6.1 and the resulting resolution as a function of p_T

Table 6.1: Parameters used to model the jet energy resolution with Eq. 6.1.

	N	S	C	M
$0.0 < \|\eta\| < 0.5$	3.97	0.183	0.027	0.626
$0.5 < \|\eta\| < 1.0$	3.55	0.240	0.025	0.526
$1.0 < \|\eta\| < 1.5$	4.55	0.227	0.034	0.590
$1.5 < \|\eta\| < 2.0$	4.63	0.237	0.045	0.487
$2.0 < \|\eta\| < 2.5$	2.53	0.343	0.052	0.287

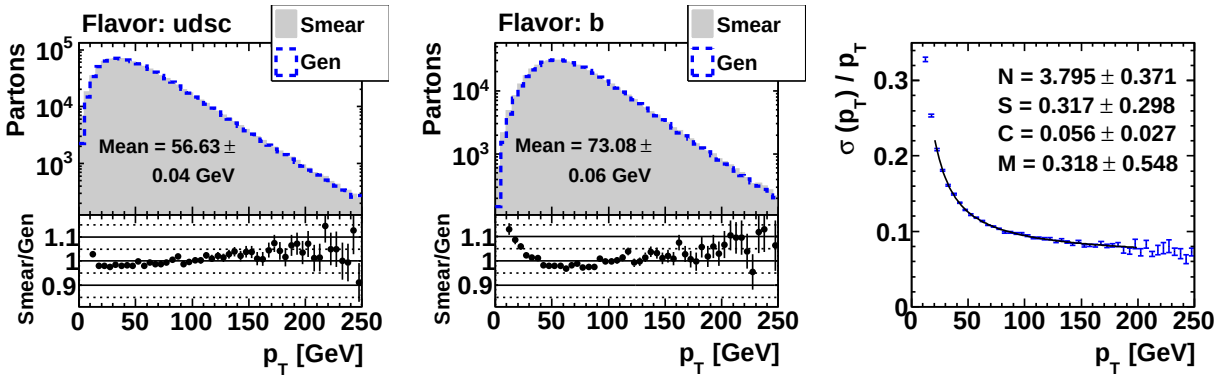

Figure 6.1: Transverse momentum spectra of u, d, s and c quarks (left) and b quarks (center) in $t\bar{t}$ events before ("gen") and after ("smear") smearing the quark energies according to the expected jet energy resolution. The relative resolution $\sigma(p_T)/p_T$ is shown on the right side. The parameter values for N, S, C and M listed in this figure are obtained by fitting Eq. 6.1 to the entries in the range of 20 GeV $< p_T <$ 200 GeV.

is shown in Fig. 6.1 together with the quark p_T spectra. As expected, migration effects reduce the yield around the peak positions of the spectra, producing additional entries in bins that are less populated in the original spectra. However, the mean p_T values, which for b quarks are by 29 % larger than for u, d, s and c quarks, are unchanged as long as no p_T selection cut is performed.

To determine the mean parton response, $p_T^{\text{smear}}/p_T^{\text{gen}}$, and mean values of the W boson and top quark masses reconstructed from the smeared quarks, Gaussian functions are fitted to the corresponding distributions as illustrated in Fig. 6.2. This is also done after performing different p_T selection cuts on the smeared four-vectors of the quarks. Figure 6.3 summarizes the observed effect of the energy resolution on the apparent energy scale and on the reconstructed W boson and top quark masses for values of $p_{T,\text{cut}}^{\text{smear}}$ up to 50 GeV. The energy resolution was varied by ±10% (relative) to estimate the uncertainty due to the assumed resolution model.

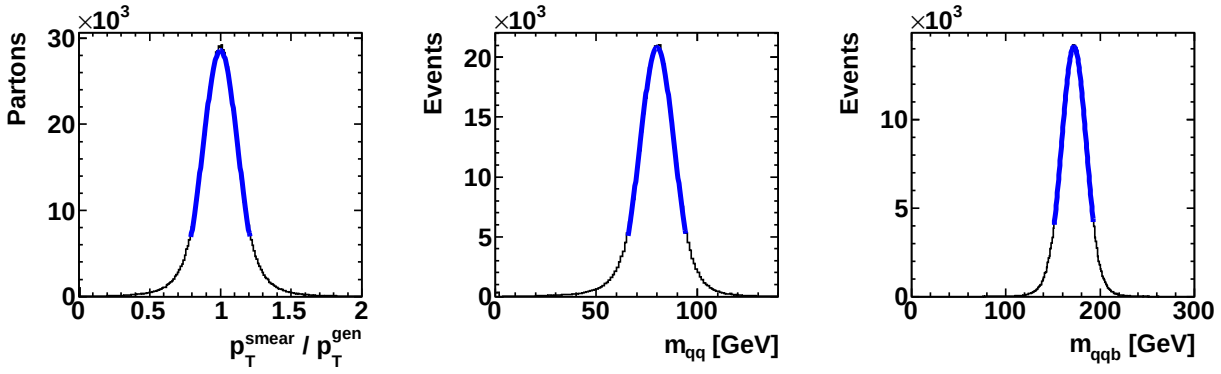

Figure 6.2: Parton response (left), defined as the ratio of the p_T after and before smearing the four-vector of the parton according to the expected jet energy resolution, and masses of W bosons (center) and top quarks (right) reconstructed from the smeared quarks. Gaussian functions are fitted to these distributions in two steps: For the second iteration, the fitting range is restricted to the region of 1.5σ around the peak of the first fit, where σ is the width of the Gaussian.

Although the mean energy response is not smaller than unity, the W boson and top quark masses for $p_{T,\mathrm{cut}}^{\mathrm{smear}} = 0$ and 10 GeV are below the masses resulting from the generated four-vectors without smearing. This shift with negative sign can be understood from the way in which the resolution of the quark energies propagates into the invariant masses of the combined four-vectors and is discussed in Appendix A.

With $p_{T,\mathrm{cut}}^{\mathrm{smear}} = 30$ GeV, the shift of the energy scale, here given as $\Delta p_T = p_T^{\mathrm{smear}}/p_T^{\mathrm{gen}} - 1$, is:

$$\begin{aligned} \Delta p_T(u,d,s,c) &= +1.15 \pm 0.03(\mathrm{stat})^{+0.19}_{-0.21}(\mathrm{resolution})\% = +1.15^{+0.19}_{-0.21}\% \\ \Delta p_T(b) &= +0.40 \pm 0.03(\mathrm{stat})^{+0.11}_{-0.11}(\mathrm{resolution})\% = +0.40^{+0.12}_{-0.11}\% \end{aligned}$$

It can be seen that the effect on the light quark energy scale is larger than the effect on the energy scale of b quarks and that the uncertainty is dominated by the assumed uncertainty on the resolution model. The resulting effect on the reconstructed W boson and top quark masses is:

$$\begin{aligned} m_{qq}^{\mathrm{smear}} - m_{qq}^{\mathrm{gen}} &= +1.08^{+0.20}_{-0.23}\ \mathrm{GeV} \qquad (\hat{=} + 1.35^{+0.25}_{-0.29}\%) \\ m_{qqb}^{\mathrm{smear}} - m_{qqb}^{\mathrm{gen}} &= +1.93^{+0.31}_{-0.45}\ \mathrm{GeV} \qquad (\hat{=} + 1.12^{+0.18}_{-0.26}\%) \end{aligned}$$

The ATLAS Collaboration published a similar study on the effects of detector resolution and p_T cuts on the apparent jet energy scale and reconstructed W boson and top quark masses [45]. The findings described therein are compatible with the results documented here.

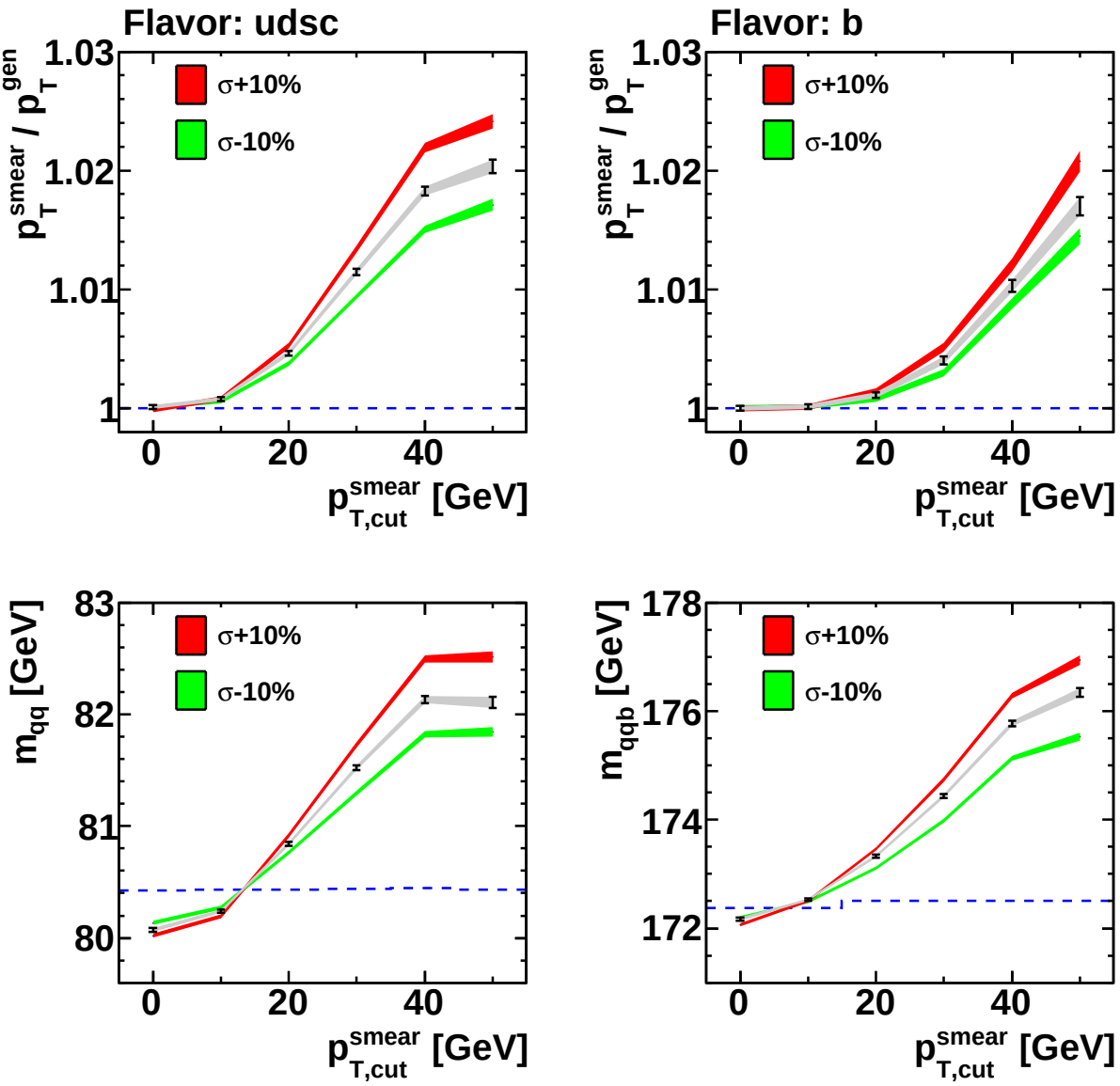

Figure 6.3: Effect of the expected energy resolution, σ, on the apparent parton energy scale (upper row) and on reconstructed W boson and top quark masses (lower row) for different selection cuts performed on the smeared p_T of the partons. The energy resolution was scaled by $\pm 10\%$ to estimate the systematic uncertainty due to the resolution parameters. The width of the shown error bands indicates the statistical uncertainty. The dashed line represents the case of a perfect resolution, i.e. without energy smearing.

The effect of the resolution bias on the apparent energy scale for $p_{T,\text{cut}}^{\text{smear}} = 30$ GeV is shown as a function of the parton p_T in Fig. 6.4. It can be seen that the bias on the energy scale is negligible in bins of the true transverse momentum, p_T^{gen}, above 40 GeV, while for 30 GeV $< p_T^{\text{gen}} <$ 40 GeV it is $\approx +4\%$ for light quarks and $\approx +3\%$ for b quarks. When looking at the apparent energy scale as a function of the smeared p_T, it can be seen that the resolution bias vanishes at $p_T^{\text{smear}} \approx 40$ GeV for light quarks and at $p_T^{\text{smear}} \approx 60$ GeV for b quarks. This is related to the shape of the p_T spectra (see Fig. 6.1) and compensating upwards and downwards migrations. Above these points, Δp_T is positive, while it is negative below these points. Differential distributions of the apparent energy scale for different values of $p_{T,\text{cut}}^{\text{smear}}$ can be found in Appendix B.

Figure 6.5 shows the effect of the resolution bias on the reconstructed W boson mass for $p_{T,\text{cut}}^{\text{smear}} = 30$ GeV as a function of the p_T of the associated quarks. In these distributions, the evolution of the apparent energy scale along the parton p_T as in figure 6.4 is reflected. In terms of the true parton p_T, the largest bias is found in the bin 30 GeV $< p_T^{\text{gen}} <$ 40 GeV. It is $\approx +2$ GeV, while it decreases to below +1 GeV above $p_T^{\text{gen}} = 40$ GeV. In terms of the smeared p_T in contrast, the bias is negligible for 30 GeV $< p_T^{\text{smear}} <$ 40 GeV. It reaches $\approx +2$ GeV above $p_T^{\text{smear}} \approx 50$ GeV. Distributions with the reconstructed W mass as a function of the parton p_T for different values of $p_{T,\text{cut}}^{\text{smear}}$ can be found in Appendix C.

The resolution bias on the top quark mass for $p_{T,\text{cut}}^{\text{smear}} = 30$ GeV as a function of the p_T of the associated b quark is also shown in Fig. 6.5. In terms of the true parton p_T, the bias varies between $\approx +1$ GeV (for 40 GeV $< p_T^{\text{gen}} <$ 50 GeV) and $\approx +3$ GeV (for 30 GeV $< p_T^{\text{gen}} <$ 40 GeV). In terms of the smeared p_T, the bias is -1.5 GeV for 30 GeV $< p_T^{\text{smear}} <$ 40 GeV, vanishes for 40 GeV $< p_T^{\text{smear}} <$ 50 GeV and reaches a value of $\approx +4$ GeV above a p_T^{smear} of 150 GeV. Distributions with the reconstructed top quark mass as a function of the parton p_T for different values of $p_{T,\text{cut}}^{\text{smear}}$ can be found in Appendix D.

6.2 Jet Response and Reconstructed Masses

In this section, the energy scale of reconstructed particle-flow jets is studied employing again the full simulation, including hadronization and detector simulation, i.e. not the simple toy model from Sec. 6.1. The standard selection criteria introduced in Chapter 5 are imposed on the reconstructed objects and events. However, information from the Monte Carlo generator is used to analyze only $t\bar{t}$ events that decay in the muon+jets channel and to match the reconstructed jets to jets built from generated hadrons and to partons from hadronic decays of top quarks. Events that do not have unambiguous matches between the detector, the hadron and the parton level are disregarded.

The jet response with respect to the hadron level is defined as the transverse momentum

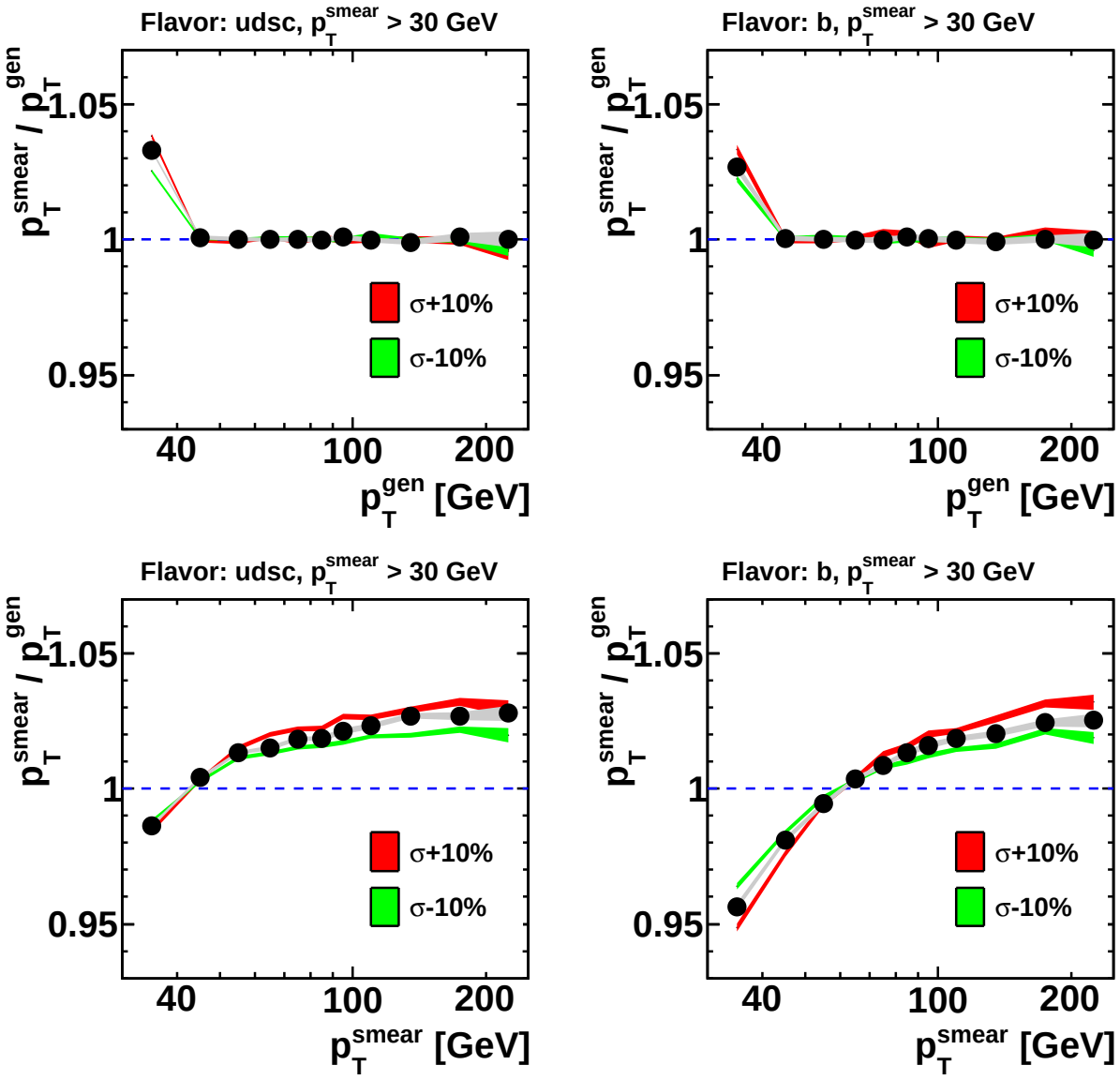

Figure 6.4: Effect of the expected energy resolution on the apparent parton energy scale after a selection cut on the smeared parton p_T at 30 GeV, shown for u, d, s and c quarks (left column) and for b quarks (right column) and as a function of the true p_T of the parton (upper row) and as a function of the smeared parton p_T (lower row). See the caption to Fig. 6.3 for further details.

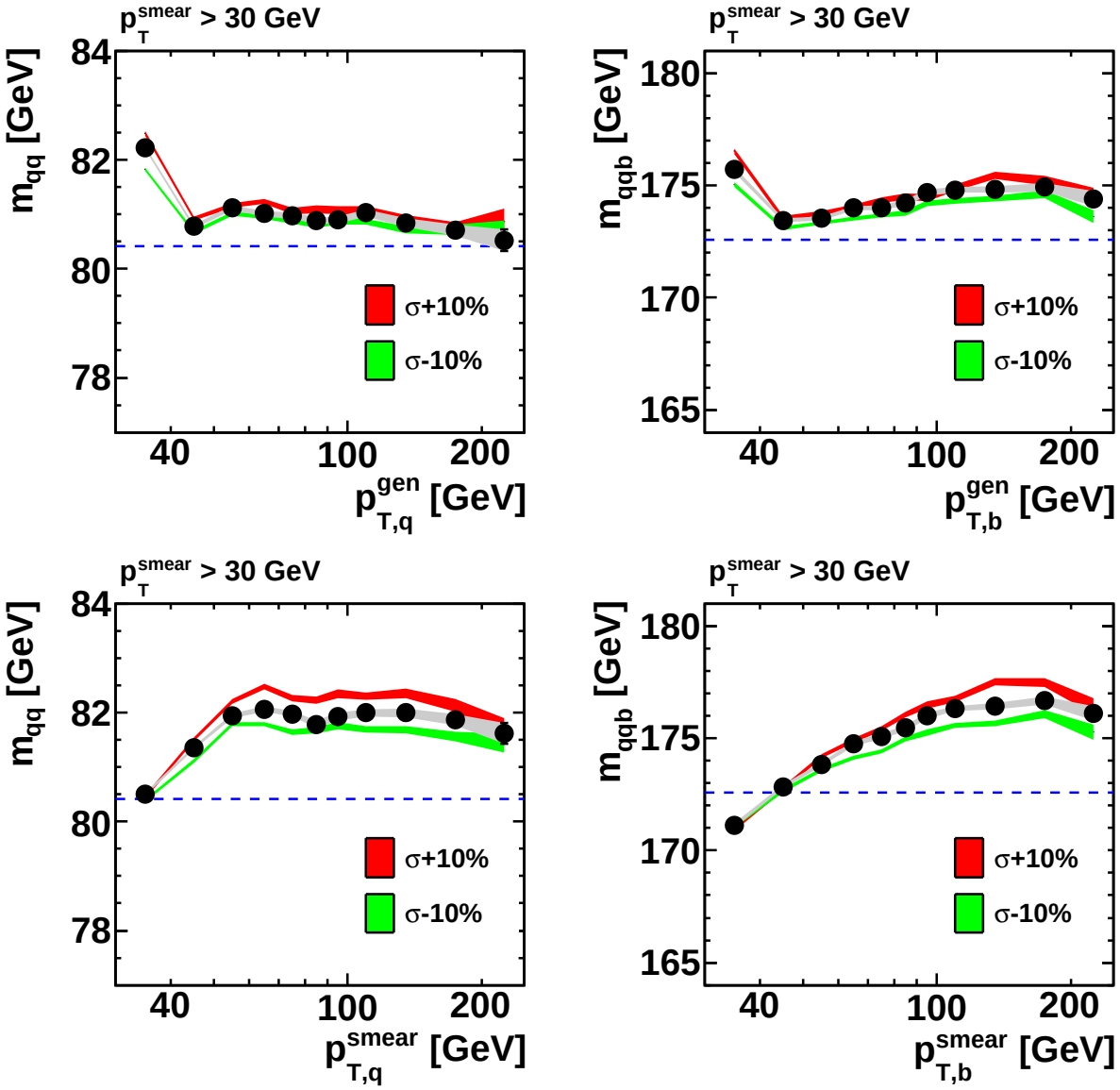

Figure 6.5: Effect of the expected energy resolution on the reconstructed W boson mass (left column) and on the reconstructed top quark mass (right column) after a selection cut on the smeared parton p_T at 30 GeV, shown as a function of the true p_T of the parton (upper row) and as a function of the smeared parton p_T (lower row). Note that the W boson mass is shown as a function of both associated quarks, i.e. each W boson enters these histograms twice, while only the single b quark is used in the case of the top quark mass. See the caption to Fig. 6.3 for other details.

of the jet on detector level relative to the transverse momentum of the corresponding jet built from generated hadrons before they were passed through the detector simulation: $p_T(\text{rec})/p_T(\text{had})$. The jet response with respect to the parton level is defined analogously as $p_T(\text{rec})/p_T(\text{parton})$.

Figure 6.6 shows different jet response distributions for jets with $p_T(\text{rec}) > 30$ GeV and $|\eta| < 2.4$ in events from $t\bar{t} \rightarrow$ muon+jets. In each case, the mean response is determined using Gaussian functions that are fitted to the distributions in two iterations. As in Sec. 6.1, first the whole histogram range is included in the fit, then the fitting range is restricted to the region of 1.5σ around the peak of the first fit. This procedure ignores the non-Gaussian tails in the response distribution, which are due to semileptonic decays of b and c hadrons.

For the distributions shown in the first column of Fig. 6.6, an additional cut of $p_T(\text{had}) > 40$ GeV is imposed to suppress the resolution bias on the apparent energy scale (cf. Fig. 6.4). A comparison to the distributions in the second column shows that the cut of $p_T(\text{had}) > 40$ GeV decreases the mean value of the jet response by 1.3% in the case of jets from u, d, s and c quarks and by 0.5% in the case of jets from b quarks, in good agreement with the predictions from the toy model in Sec. 6.1.

The first column of Fig. 6.6 suggests that the energy scale of jets from u, d, s and c quarks is too high by 2.2% while the energy scale of jets from b quarks is too low by 2.0%. These small mis-calibrations could be explained by differences in the software versions in which the jet energy corrections were derived and in which the events for this thesis were reconstructed and by the fact that the default jet correction factors were optimized for the average flavor mix in QCD dijet events, containing mostly gluon jets.

By comparing the second to the third column, it can be seen from Fig. 6.6 that the jet energy scale with respect to the hadron level is by 3.3% and 2.0% above the jet energy scale with respect to the parton level for light and for b jets, respectively. The main reason for the discrepancy between the hadron-level and the parton-level scales is showering of energy out of the jet cone in the hadronization. As a consequence, it is always necessary to specify with respect to which energy scale the jet response is optimized. The default jet energy corrections at CMS are supposed to bring at unity the mean jet response with respect to the hadron level. This is useful for most physics analyses. For some analyses, however, correcting the jet energy back to the parton level enables a comparison to more fundamental parameters. This can be the case, for example, when looking at the invariant mass of two jets stemming from partons that originated from one fundamental particle, e.g. from a W boson. And, for the same reason, jet energy corrections derived by explicitly constraining the invariant mass of jets from hadronically decaying W bosons to the true value of $m_W = 80.4$ GeV will refer to the parton level. Nonetheless, no parton-level corrections are used within this thesis. The template method, which is chosen for the measurement of the top quark mass in Chapter 7, does not require corrections to the parton level but only objects calibrated to the same energy scale in data and simulation.

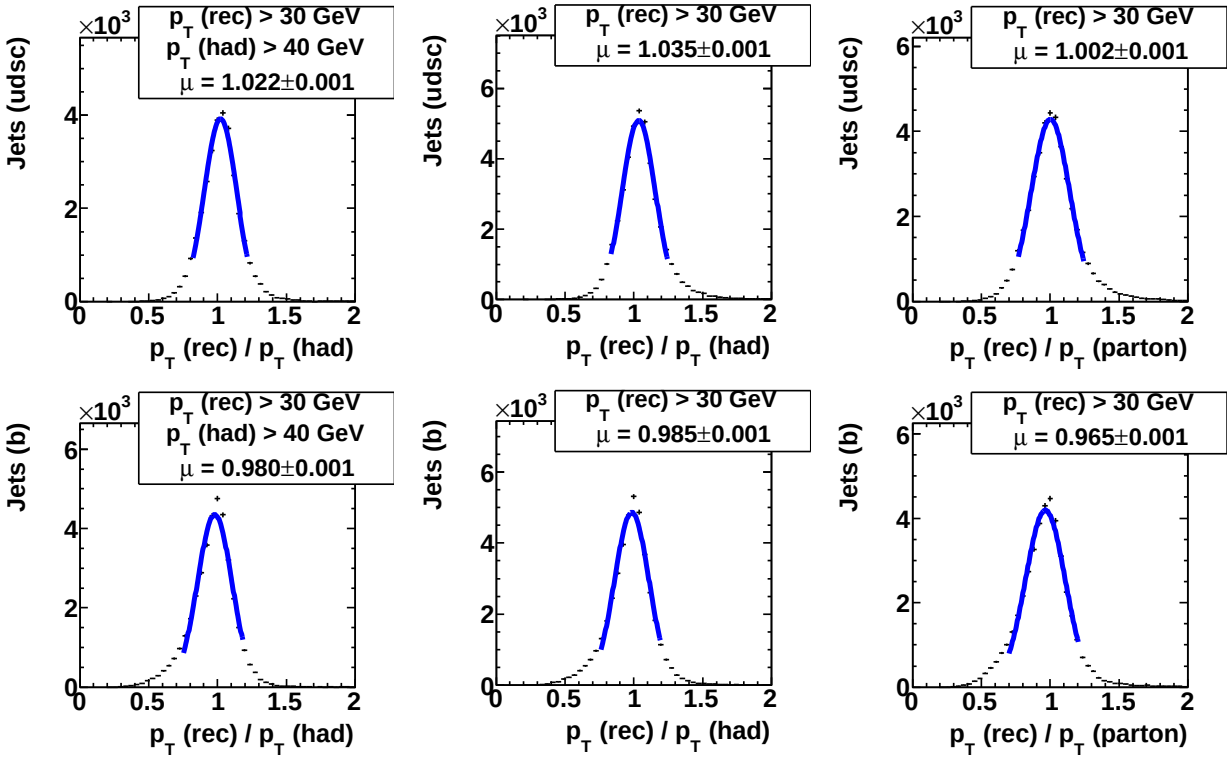

Figure 6.6: Jet response for jets from u, d, s and c quarks (upper row) and for jets from b quarks (lower row), shown with respect to the hadron level (first and second column) and with respect to the parton level (third column). All these distributions are obtained from jets with a reconstructed p_T above 30 GeV. For the distributions in the left column, an additional requirement of $p_T > 40$ GeV is imposed on the hadron-level jets. The parameter μ refers the Gaussian mean.

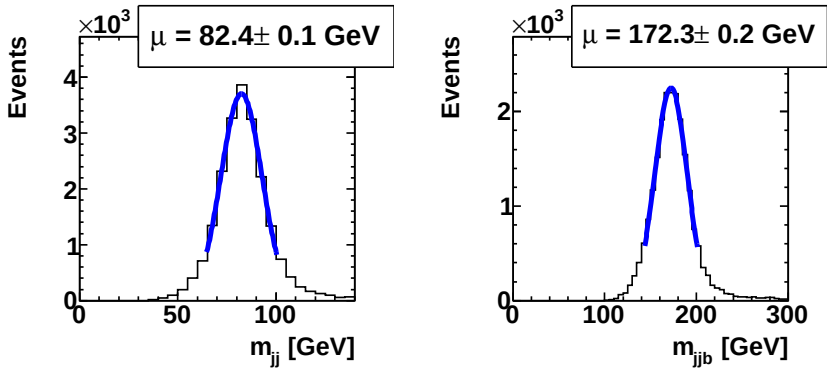

Figure 6.7: W boson mass (left) and top quark mass (right) reconstructed from jets that were matched to the partons from hadronically decaying top quarks. The parameter μ refers to the Gaussian mean.

Fig. 6.7 shows the W boson and top quark masses reconstructed from jets that could be unambiguously associated to the corresponding partons using generator information. The fact that despite the energy resolution bias the value of the reconstructed top quark mass corresponds roughly to the generated value of 172.5 GeV could be explained by the energy scale of the b jets which was found to be slightly too low (see above). In any case, the measurement of the top quark mass and the jet energy scale presented in Chapter 7 does not directly depend on the closure tests for the energy scale in simulated events presented here. It will only be sensitive to the relative difference between the energy scales in data and simulation. The jet energy scale can deviate from unity and the top quark mass does not have to be reconstructed at the true value, as long as the underlying effects are modeled correctly by the simulation.

Chapter 7

Measurement of Top Quark Mass and Jet Energy Scale

The selection criteria discussed in Chapter 5 result in a sample of events with a very high $t\bar{t}$ fraction. And, as it will be shown in the following, already simple algorithms allow the reconstruction of trijet masses that have a strong correlation with m_t. However, even if the jet energy scale were perfectly calibrated, the peak value of the invariant mass distribution obtained from those three jets per event assigned to a hadronically decaying top quark does not yield m_t directly. Several reasons for this have been discussed above. Among them are color connections between the decay products of the top quark and other parts of the event (see Sec. 2.3.1) and effects related to the finite jet energy resolution (see Sec. 6.2). Several approaches for top quark mass measurements exist. A short overview is given in Sec. 2.3.3. For this thesis, the template method is chosen, following in several aspects a measurement performed previously by the CDF Collaboration [46]. In this way, a well established technique from the Tevatron that allows for a good precision but is relatively simple and robust is taken as the basis for one of the very first measurements of the top quark mass at the LHC. The chosen method relies on a reasonable description of the underlying processes by the simulation, including both the top quark decay and the jet response of the experimental apparatus. But at the same time it enables an in-situ measurement of the jet energy scale, thus constraining the dominant systematic uncertainty using the data itself.

7.1 Mass Reconstruction

The invariant mass of those three jets in the event that yield the vectorial sum with maximum p_T is a simple estimator of the mass of the hadronically decaying top quark. For the measurement presented here, this observable, often referred to as M3, is reconstructed

Table 7.1: Correlation factors for pairs of the observables M3, M2 and ΔM_{32}, determined from simulated $t\bar{t}$ events.

	M3	M2	ΔM_{32}
M3	1	0.82	0.66
M2		1	0.12
ΔM_{32}			1

considering all selected jets, i.e. not only the four leading jets in the event, but always requiring exactly one b-tagged and two untagged jets per trijet combination. The invariant mass of the two untagged jets that were assigned to M3 is an estimator of the mass of the hadronically decaying W boson. This observable will be referred to as M2. The resulting M3 and M2 distributions can be found in Fig. 7.1, which also shows the distribution of the event-wise mass difference ΔM_{32} = M3 - M2. The correlations between these three observables are listed in Table 7.1. It can be seen that M3 and M2 are strongly correlated, while there is only a modest correlation between M2 and ΔM_{32}. The latter two will therefore be used for the simultaneous measurement of m_t and JES described in the following.

Table 7.2 holds estimates for the fraction of events in which the correct jets are chosen in the reconstruction of M2 and M3 by the algorithm described above. These fractions were determined using simulated $t\bar{t}$ events in the muon+jets channel. In order to relate them to the total number of events, one would have to take into account that 94% of all events that pass the final selection are expected to be from $t\bar{t}$ production and 88% out of these to decay in the muon+jets channel. All selected jets are considered in the jet-parton matching used to determine the numbers that are listed in Table 7.2. To illustrate the dependence on the jet-parton matching algorithm, two different approaches are used: the first matching algorithm considers only events in which for each of the four quarks exactly one jet is found within a cone of size $\Delta R = 0.5$ in (η, ϕ), while the second matching algorithm minimizes the summed ΔR of the four jet-parton pairs but does not reject events with ambiguities or outliers with large ΔR. Table 7.2 shows that the correct jets are chosen for M2 in about $\frac{2}{3}$ of the $t\bar{t}$ events that decay in the muon+jets channel. Roughly half of the events in this decay channel have the correct jets associated to M3. Only a very small fraction of events that has the correct jet combination for M3 gets a wrong jet pair associated to M2.

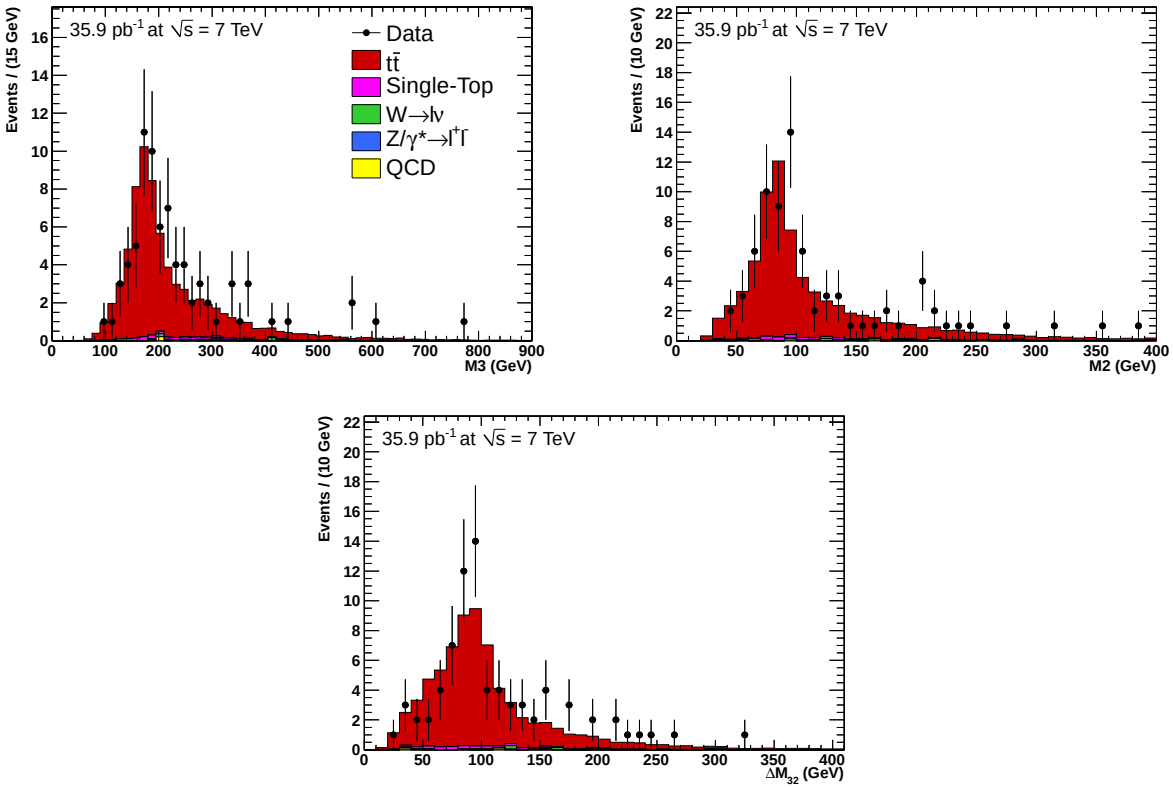

Figure 7.1: M3 (upper row left), M2 (upper row right) and ΔM_{32} (lower row) distributions in data compared to the Monte Carlo predictions.

Table 7.2: Fraction of simulated $t\bar{t}$ events in the muon+jets channel with correct jet combinations for M2 and M3. See text for further details.

Algorithm for jet-parton matching	Unambiguous only	$\min \sum \Delta R$
Both M2 and M3 correct	48.2%	43.3%
M2 correct, M3 wrong	22.0%	21.8%
M2 wrong, M3 correct	3.3%	4.8%
Neither M2 nor M3 correct	26.5%	30.1%

7.2 Template Parametrization

7.2.1 Parametrization of ΔM_{32}

ΔM_{32} distributions from simulated $t\bar{t}$ events with $m_t = 166.5, 172.5, 178.5$ GeV and JES = 0.90, 0.95, 1.00, 1.05, 1.10 are shown in Fig. 7.2. It can be seen how the peak of the distribution moves to higher values when increasing the value of m_t or JES. The shape of all distributions can be nicely described by the sum of a gamma distribution and two Gaussians:

$$\begin{aligned} P(\Delta M_{32}) &= \alpha_3 \cdot \frac{\alpha_1^{-\alpha_0}}{\Gamma(\alpha_0)} \cdot (\Delta M_{32} - \alpha_2)^{\alpha_0 - 1} \cdot \exp\left(-\frac{(\Delta M_{32} - \alpha_2)}{\alpha_1}\right) \\ &\quad + (1-\alpha_3) \cdot \left(\alpha_6 \frac{1}{p_5\sqrt{\alpha_4} \cdot \sqrt{2\pi}} \cdot \exp\left(\frac{-(\Delta M_{32} - \alpha_4)^2}{2(p_5\sqrt{\alpha_4})^2}\right) \right. \\ &\quad \left. + (1-\alpha_6) \frac{1}{p_8\sqrt{\alpha_7} \cdot \sqrt{2\pi}} \cdot \exp\left(\frac{-(\Delta M_{32} - \alpha_7)^2}{2(p_8\sqrt{\alpha_7})^2}\right) \right) \end{aligned} \tag{7.1}$$

α_0 : "shape" parameter of the gamma distribution
α_1 : "scale" parameter of the gamma distribution
α_2 : horizontal shift of the gamma distribution
α_3 : relative contribution of the gamma distribution
$\alpha_{4/7}$: peak position of the first/second Gaussian
α_6 : relative contribution of the first Gaussian to the sum of both Gaussians

One Gaussian corresponds to the main mass peak, which consist of ΔM_{32} values from events in which all three jets were chosen correctly. The other Gaussian describes a small shoulder at lower values of ΔM_{32}, which arises from events in which one of the three jets was chosen incorrectly. The gamma distribution describes the remaining combinatorial background as well as background from $t\bar{t}$ events that did not decay in the muon+jets channel.

In order to obtain one template function for ΔM_{32} smoothly varying with m_t and JES, all seven α_i are allowed to depend linearly on both quantities:

$$\alpha_i = p_i + p_{i+9} \cdot (\mathrm{JES} - 1) + p_{i+18} \cdot (m_t - 172.5) \qquad i \in \{0, 1, 2, 3, 4, 6, 7\} \tag{7.2}$$

The widths of both Gaussians are calculated as the square root of the respective peak position multiplied by a factor (p_5 and p_8, respectively) that is independent of JES and

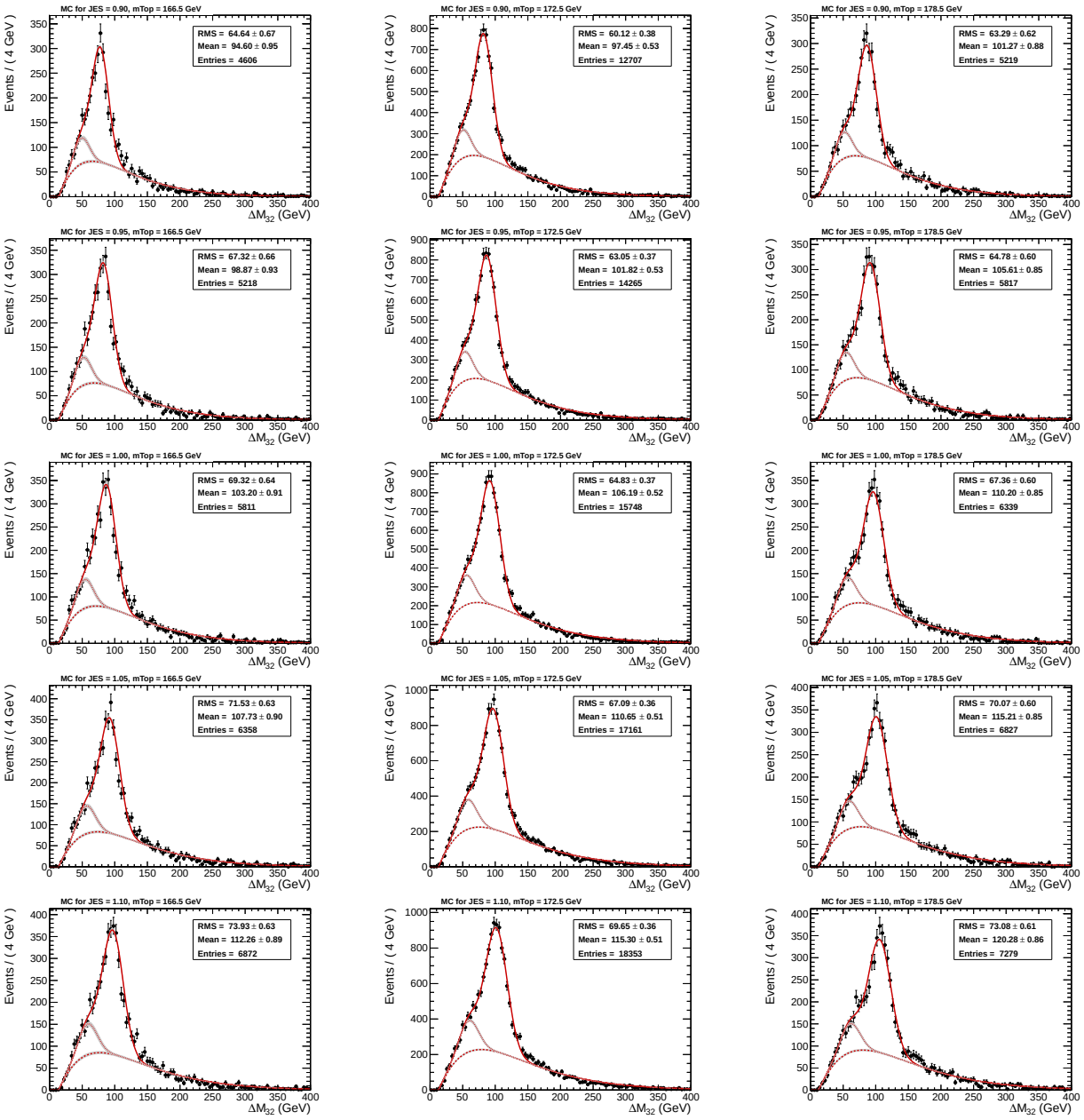

Figure 7.2: ΔM_{32} templates overlaid with the fitted function $P(\mathrm{JES}, m_t)$. The templates are shown for $m_t = 166.5$ GeV (left), 172.5 GeV (center) and 178.5 GeV (right) and for JES = 0.90 (first row), 0.95 (second row), 1.00 (third row), 1.05 (fourth row) and 1.10 (fifth row).

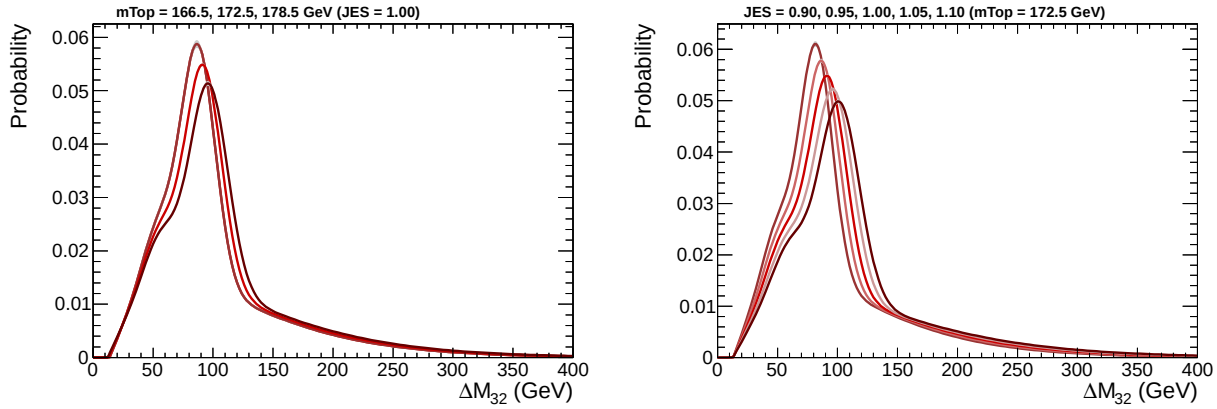

Figure 7.3: Direct comparison of the probability density function $P(\Delta\mathrm{M}_{32}; \mathrm{JES}, m_t)$ at JES = 1.00 and $m_t = 166.6, 172.5, 178.5$ GeV (left) and at $m_t = 172.5$ GeV and JES = 0.90, 0.95, 1.00, 1.05, 1.10 (right).

m_t. This gives $7 \cdot 3 + 2 = 23$ parameters p_i for $P(\Delta\mathrm{M}_{32}; \mathrm{JES}, m_t)$, which are determined in a simultaneous likelihood fit to the 15 template histograms shown in Fig. 7.2. A direct comparison of the resulting probability density function evaluated at different values of m_t and JES can be found in Fig. 7.3. The parameter α_7, which corresponds to the position of the main Gaussian peak, has a large sensitivity to m_t and JES as illustrated in Fig. 7.4. However, the other α_i are also correlated with m_t and JES. This will be taken into account in the following and the measurement of m_t and JES uses the shape of the entire probability density function $P(\Delta\mathrm{M}_{32}; \mathrm{JES}, m_t)$. The dependence of all α_i on m_t and JES as well as the values of all parameters p_i can be found in Appendix E.

7.2.2 Parametrization of M2

Figure 7.5 shows M2 distributions from simulated $t\bar{t}$ events with $m_t = 166.5, 172.5, 178.5$ GeV and JES = 0.90, 0.95, 1.00, 1.05, 1.10. It can be seen how the distribution moves to higher values when increasing the JES, while there is no significant dependence on m_t. The shape of all distributions can be nicely described again by the sum of a gamma distribution and two Gaussians:

$$\begin{aligned} P(\mathrm{M2}) \;=\; & \alpha_3 \cdot \frac{\alpha_1^{-\alpha_0}}{\Gamma(\alpha_0)} \cdot (\mathrm{M2} - \alpha_2)^{\alpha_0 - 1} \cdot \exp\left(-\frac{(\mathrm{M2} - \alpha_2)}{\alpha_1}\right) \\ & + (1 - \alpha_3) \cdot \left(\alpha_6 \frac{1}{p_5\sqrt{\alpha_4} \cdot \sqrt{2\pi}} \cdot \exp\left(\frac{-(\mathrm{M2} - \alpha_4)^2}{2(p_5\sqrt{\alpha_4})^2}\right) \right. \\ & \left. + (1 - \alpha_6) \frac{1}{p_7\sqrt{\alpha_4} \cdot \sqrt{2\pi}} \cdot \exp\left(\frac{-(\mathrm{M2} - \alpha_4)^2}{2(p_7\sqrt{\alpha_4})^2}\right) \right) \end{aligned} \tag{7.3}$$

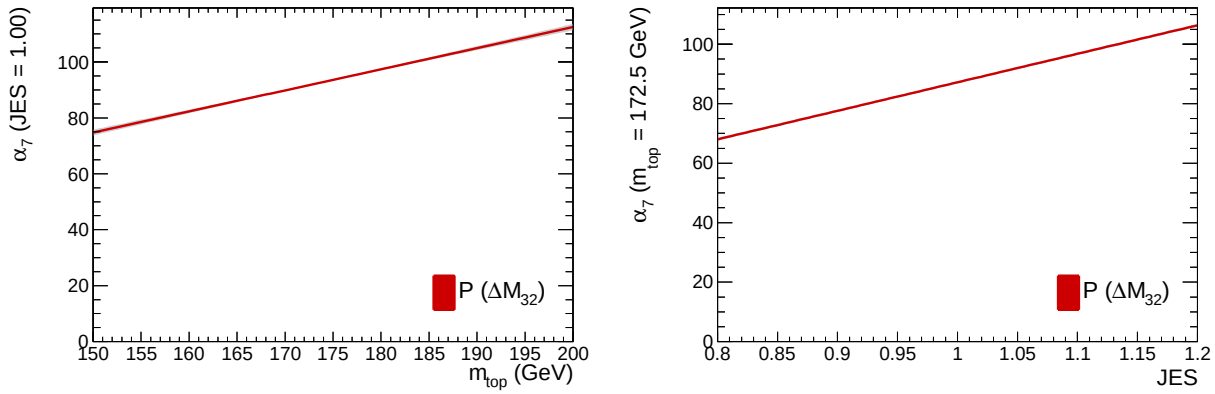

Figure 7.4: Parameter α_7, which determines the peak position of the main Gaussian in the template function $P(\Delta\mathrm{M}_{32})$, shown as a function of m_t (left) and JES (right).

α_0 : "shape" parameter of the gamma distribution
α_1 : "scale" parameter of the gamma distribution
α_2 : horizontal shift of the gamma distribution
α_3 : relative contribution of the gamma distribution
α_4 : peak position of both Gaussians
α_6 : relative contribution of the first Gaussian to the sum of both Gaussians

The parametrization is identical to the one chosen for $\Delta\mathrm{M}_{32}$ except for two differences. In the case of M2, both Gaussians are centered at the same peak position. As discussed in Sec. 7.1, there is less combinatorial background in M2 than in $\Delta\mathrm{M}_{32}$. The double Gaussian is thus only used to better model the shape of the narrow M2 peak, which is caused by the energy resolution of the particle-flow jets. Furthermore, all α_i for $P(\mathrm{M2})$ only depend on the JES and not on m_t:

$$\alpha_i = p_i + p_{i+9} \cdot (\mathrm{JES} - 1) \qquad i \in \{0, 1, 2, 3, 4, 6\} \tag{7.4}$$

p_5 and p_7 are the two parameters that in the case of M2 determine the width of the two Gaussians as a function of the common mean value α_4. This gives $6{\cdot}2{+}2 = 14$ parameters p_i for $P(\mathrm{M2};\mathrm{JES})$, which are determined in a simultaneous likelihood fit to the 15 template histograms shown in Fig. 7.5. A direct comparison of the resulting probability density function evaluated at different values of JES can be found in Fig. 7.6. The evolution of all α_i of $P(\mathrm{M2};\mathrm{JES})$ as a function of the JES as well as the values of all parameters p_i can be found in Appendix E.

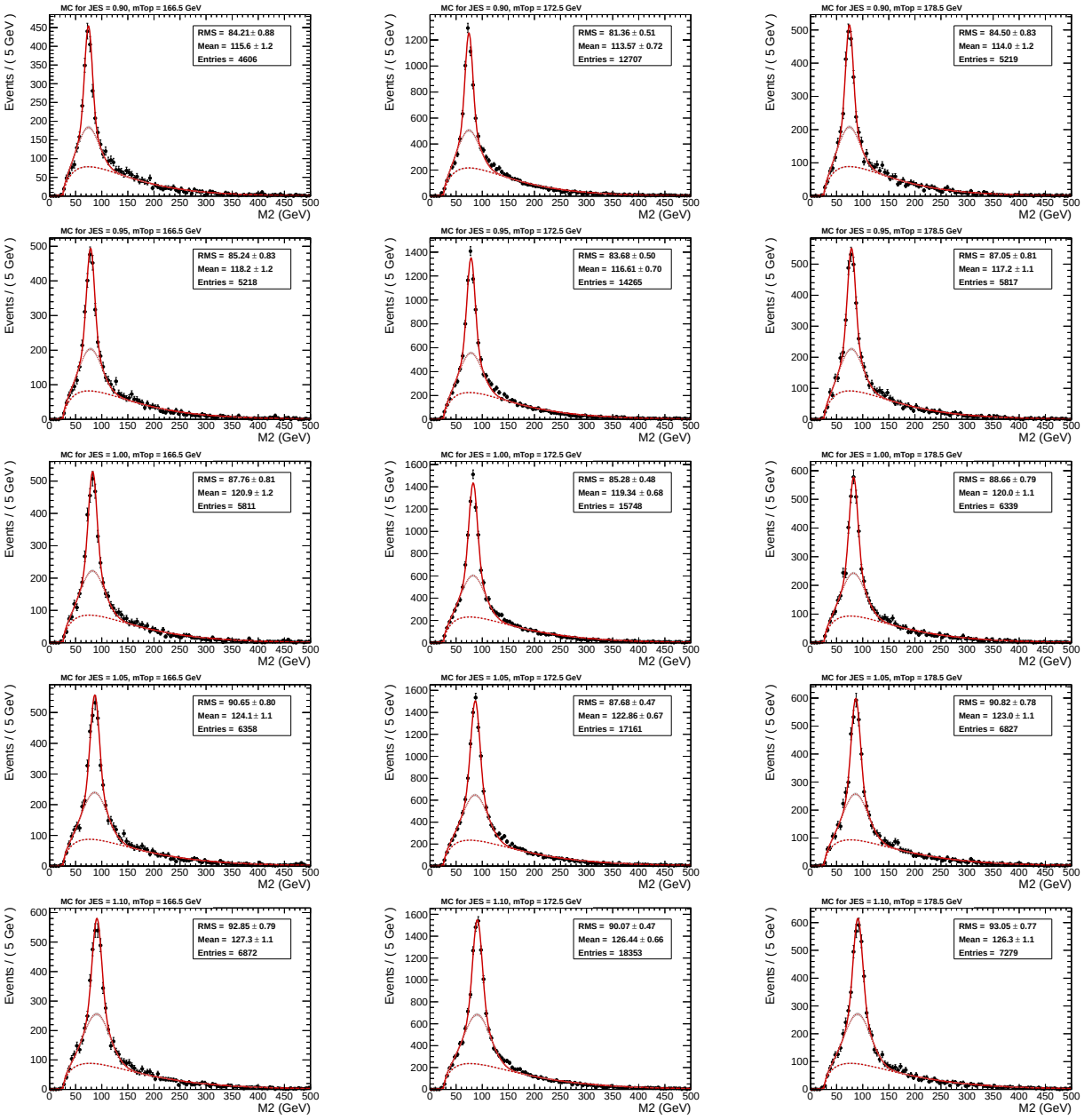

Figure 7.5: M2 templates overlaid with the fitted function $P(\text{JES})$. The templates are shown for $m_t = 166.5$ GeV (left), 172.5 GeV (center) and 178.5 GeV (right) and for JES = 0.90 (first row), 0.95 (second row), 1.00 (third row), 1.05 (fourth row) and 1.10 (fifth row).

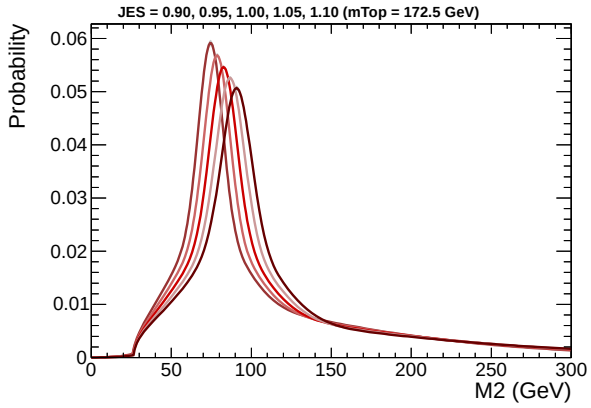

Figure 7.6: Direct comparison of the probability density function $P(\mathrm{M2};\mathrm{JES})$ at JES = 0.90, 0.95, 1.00, 1.05, 1.10.

7.3 Fitting of top quark mass and jet energy scale

A combined unbinned maximum likelihood fit of the $\Delta\mathrm{M}_{32}$ and M2 template functions to the data is finally performed to measure m_t and JES:

$$\mathcal{L} = \mathcal{L}_{\Delta\mathrm{M}_{32}} \times \mathcal{L}_{\mathrm{M2}} \tag{7.5}$$

Therein, the likelihoods for $\Delta\mathrm{M}_{32}$ and M2 are defined as follows:

$$\mathcal{L}_{\Delta\mathrm{M}_{32}} = \prod_{k}^{N} P(\Delta\mathrm{M}_{32,k}; m_t, \mathrm{JES}) \tag{7.6}$$

$$\mathcal{L}_{\mathrm{M2}} = \prod_{k}^{N} P(\mathrm{M2}_k; \mathrm{JES}) \tag{7.7}$$

N is the total number of selected events. The only free parameters of the fit are m_t and JES. All other shape parameters p_i of the probability density functions $P(\Delta\mathrm{M}_{32};\mathrm{JES}, m_t)$ and $P(\mathrm{M2};\mathrm{JES})$, determined in Sections 7.2.1 and 7.2.2, are kept constant. For the analysis presented here, the $t\bar{t}$ templates are used to model the full data. Influences of non-$t\bar{t}$ backgrounds will be treated as a systematic error.

7.4 Validation on Simulated Events

Pseudo-experiments are performed to test the method of this measurement for biases and to validate the statistical uncertainties. For every pseudo-experiment at given values of m_t

and JES, the number of events is varied within Poisson statistics around the observed value of 78 for an integrated luminosity of 35.9 pb^{-1}. Then events are randomly picked from the full statistics of the corresponding $t\bar{t}$ Monte Carlo sample and the fit of $\mathcal{L}_{\Delta \mathrm{M}_{32}} \times \mathcal{L}_{\mathrm{M2}}$ is performed just as for data. Since for the pseudo-experiments it is known with which values of m_t and JES the events were generated, one can calculate the residual and the pull, defined as:

$$\text{residual} = \text{fitted value} - \text{input value} \tag{7.8}$$

$$\text{pull} = \frac{\text{fitted value} - \text{input value}}{\text{uncertainty of fitted value}} \tag{7.9}$$

If a method has no bias, one should get a mean residual of 0 and, consequently, also a mean pull of 0. A pull width of 1 suggests that the statistical uncertainties are estimated correctly.

Figure 7.7 shows the residuals, the pulls and the expected statistical uncertainties of the fitted m_t and JES from 3,000 pseudo-experiments generated with $m_t = 172.5$ GeV and JES = 1.00. The corresponding distributions for input values of $m_{\mathrm{top}} = 166.5, 178.5$ GeV and for JES = 0.90, 0.95, 1.05, 1.10 can be found in Appendix F. They are also obtained from 3,000 pseudo-experiments at each point.

When estimating the uncertainties on values determined using these pseudo-experiments, the limited statistics of the Monte Carlo samples has to be taken into account. If N is the number of pseudo-experiments, n the number of events drawn for each pseudo-experiment and $\mathcal{N}$ the size of the pool from which the events are drawn, and if the pseudo-experiments are generated without replacement, i.e. such that events can not be drawn twice within one pseudo-experiment, then the error on a mean value determined from the pseudo-experiments goes rather like $\sqrt{1/N + n/\mathcal{N}}$ than $1/\sqrt{N}$ [47]. In this thesis, the uncertainties on the mean values of the Gaussians fitted to the distributions from the pseudo-experiments will therefore be rescaled by a factor of $\sqrt{1/N + n/\mathcal{N}}/(1/\sqrt{N}) = \sqrt{1 + N \cdot n/\mathcal{N}}$. For 3,000 pseudo-experiments and 78 events drawn for each pseudo-experiment from the same 15,748 selected events in a $t\bar{t}$ sample, the scaling factor has a value of roughly 4. Since pseudo-experiments are generated with replacement for the analysis presented here, i.e. events could be drawn multiple times for each pseudo-experiment, a Poissonian term would have to be incorporated into $\sqrt{1/N + n/\mathcal{N}}$ in order to take into account the correlations of events within the individual pseudo-experiments. The resulting scale factor would be still slightly larger. However, this is neglected in the numbers shown in the following. Similar considerations as for the error on the mean values above motivate the usage of a scale factor of $\sqrt{1 + N \cdot (n/\mathcal{N})^2}$ for the error on the widths of the Gaussians fitted to the distributions from the pseudo-experiments. In the case of 3,000 pseudo-experiments and 78 events drawn from a pool of 15,748 events, such scale factor for the uncertainty on the pull widths is indeed only marginally larger than unity.

Figure 7.8 summarizes the mean residuals of m_t and JES as a function of the different input values of m_t and JES. There is no significant bias visible for m_t and, on average,

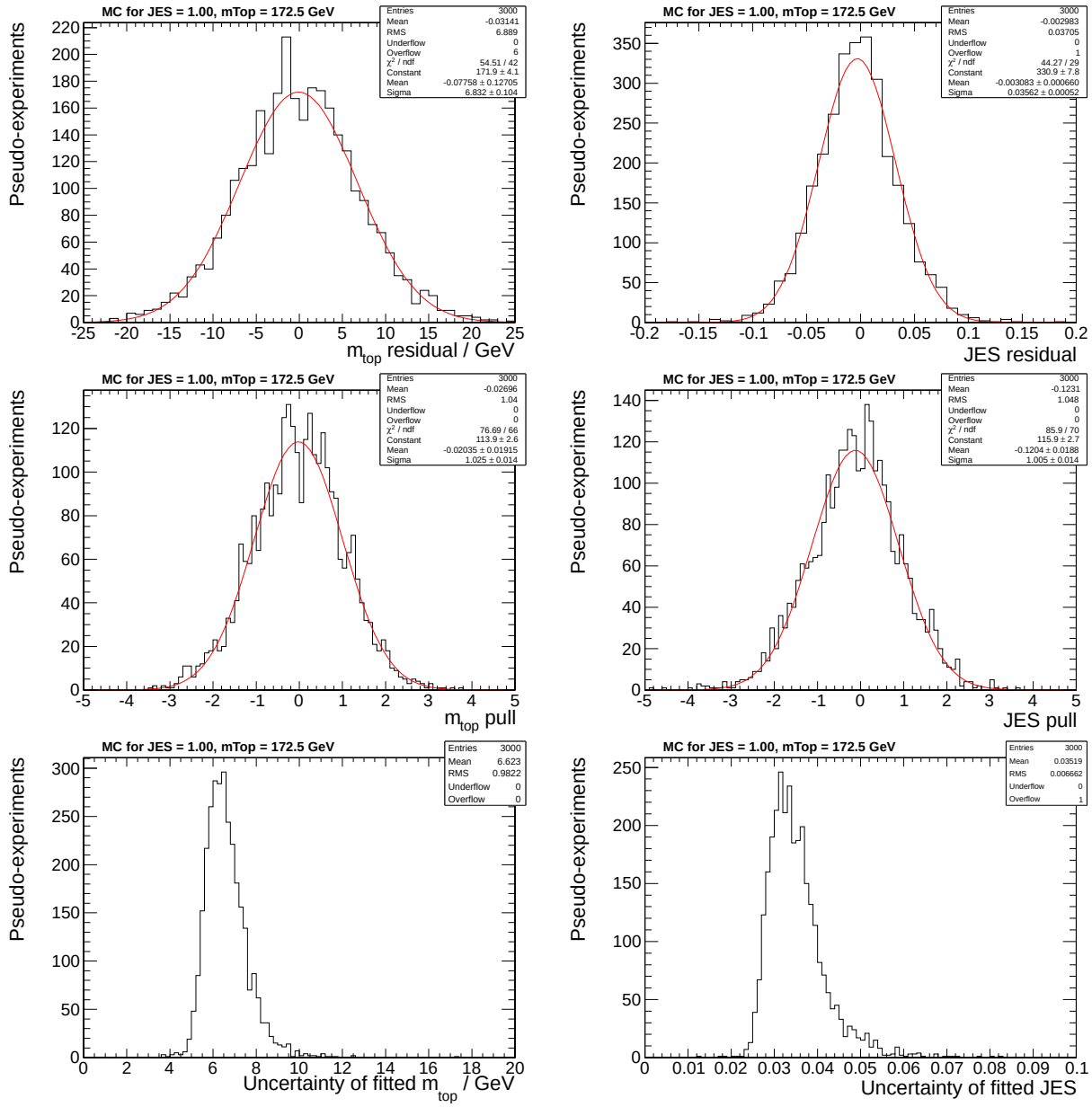

Figure 7.7: Residuals (first row), pulls (second row) and expected statistical uncertainties (third row) of m_t (left) and JES (right) for 3,000 pseudo-experiments at 35.9 pb^{-1} with input values of $m_t = 172.5$ GeV and JES = 1.00.

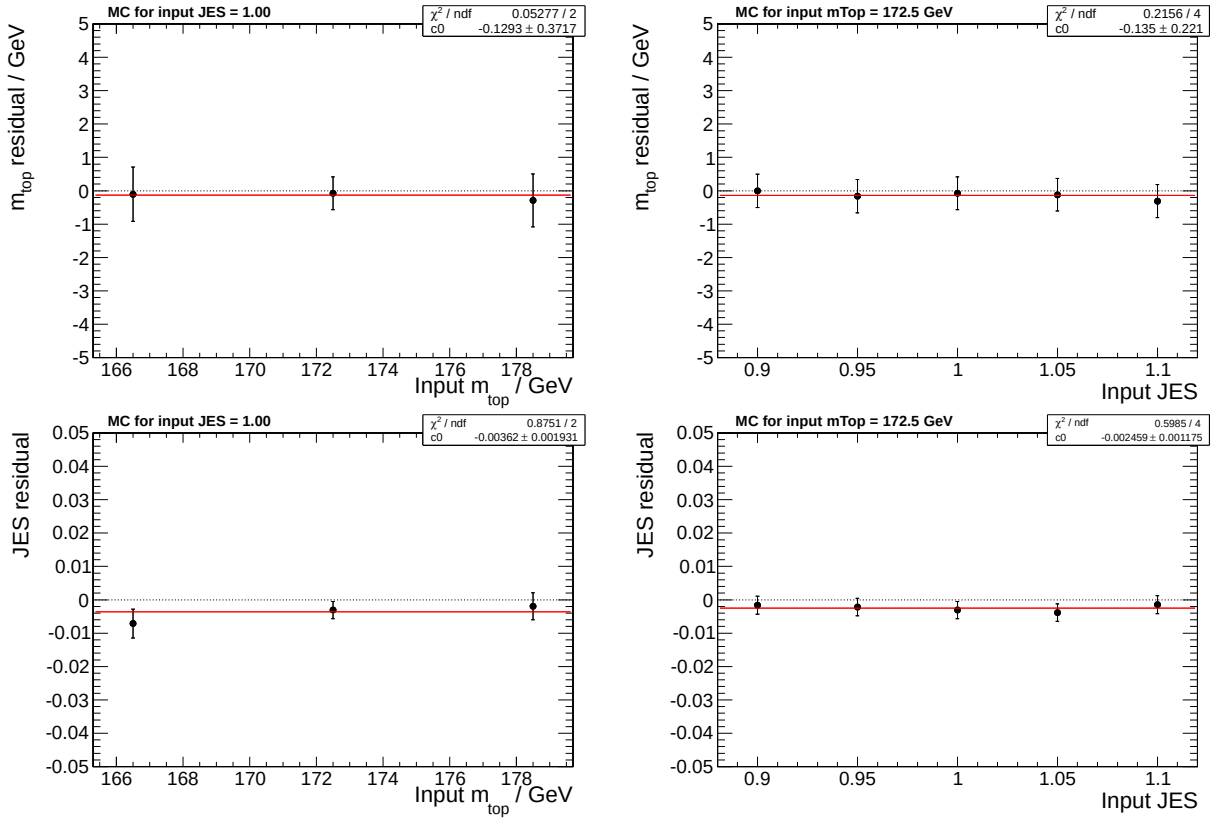

Figure 7.8: Mean residuals of m_t (upper row) and of JES (lower row) as a function of the generated m_t (left) and as a function of the generated JES (right).

the mean JES residual also deviates by less then 0.004 from 0. Instead of correcting the measurement for the small offsets observed in Fig. 7.8, 0.1 GeV and 0.004 will be added to the systematic uncertainties on the fitted m_t and JES, respectively.

Figure 7.9 summarizes the pull widths of m_t and JES as a function of the different input values. Pull widths slightly larger than unity indicate a small underestimation of the statistical uncertainties by the combined likelihood fit for m_t and JES. To account for this, the fit uncertainties for m_t and JES will be rescaled by a factor of 1.02.

As shown in Fig. 7.7, the expected statistical uncertainties for an integrated luminosity of 35.9 pb^{-1} are close to 7 GeV and around 3.5% for m_t and JES, respectively. The evolution of the expected uncertainty on the fitted m_t and JES as a function of the integrated luminosity is illustrated in Fig. 7.10. These distributions were obtained by performing several sets of pseudo-experiments, successively increasing the number of events per pseudo-experiment, n, according to the expectation for the corresponding integrated luminosity. The expected uncertainty on the fitted m_t and JES decreases as $1/\sqrt{n}$.

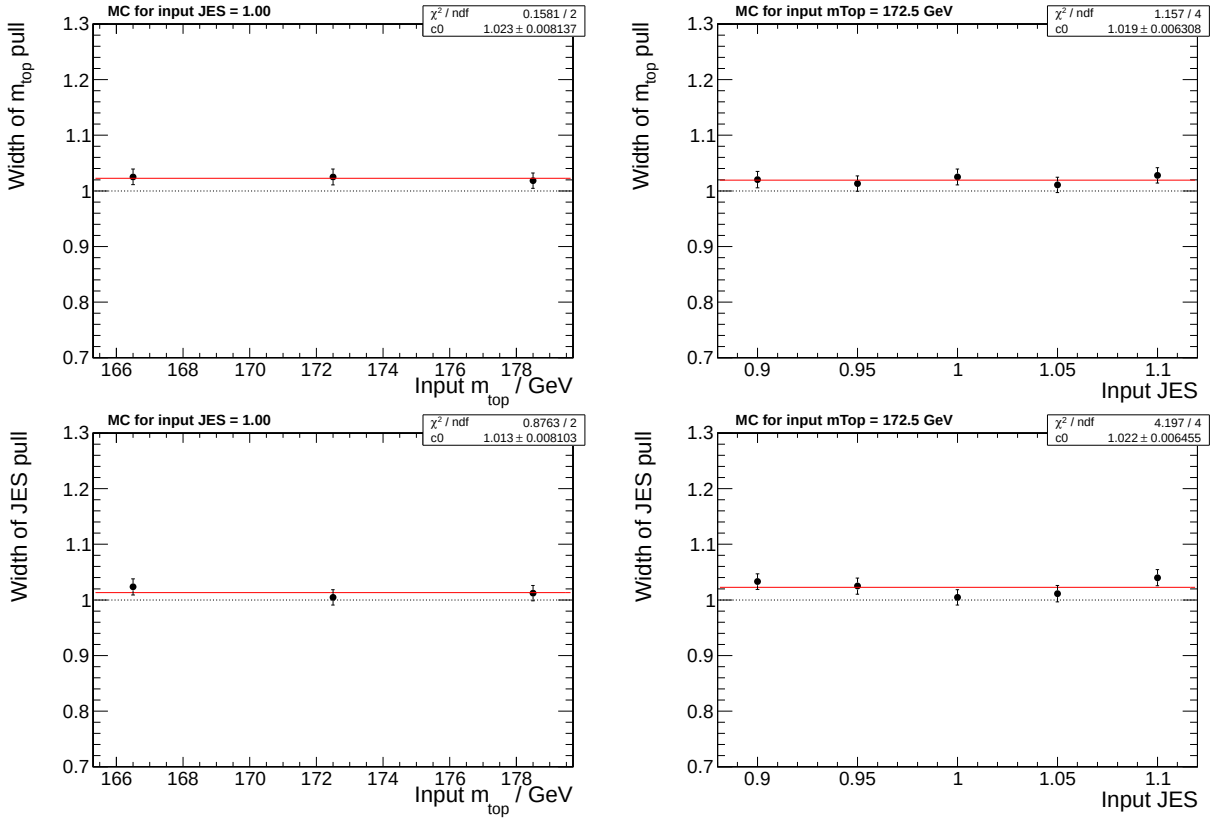

Figure 7.9: Pull widths of m_t (upper row) and of JES (lower row) as a function of the generated m_t (left) and as a function of the generated JES (right).

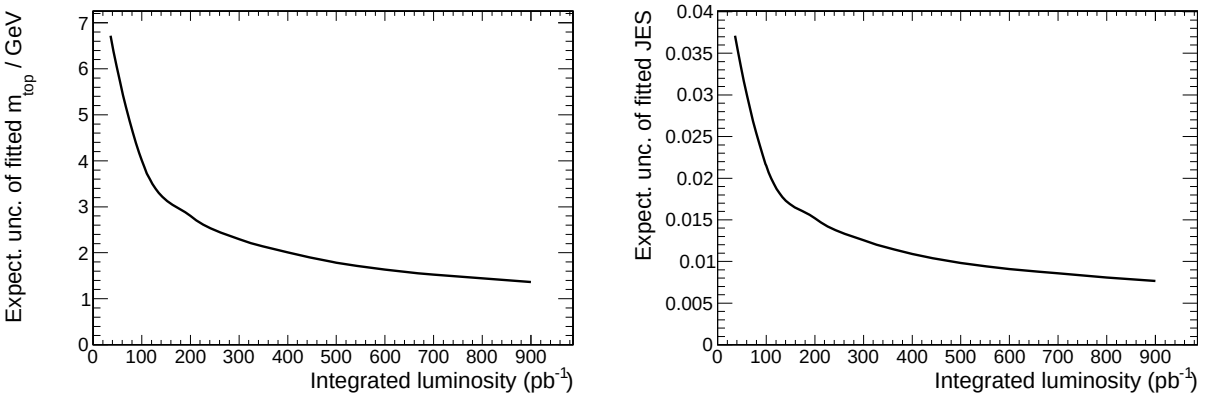

Figure 7.10: Evolution of the expected uncertainty on the fitted m_t (left) and JES (right) as a function of the integrated luminosity.

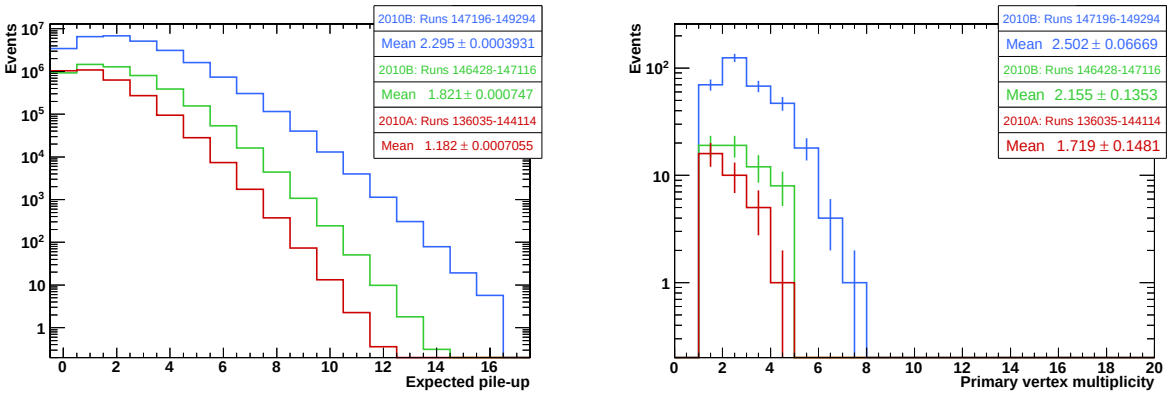

Figure 7.11: Expected pileup (left) and multiplicity of good primary vertices (right). The distributions are shown for the three different data-taking periods introduced in Chapter 5. The vertices, required to have ndof > 4, $|z| < 24$ cm and $\rho < 2$ cm, are shown for the sample before demanding two b-tagged jets, including 423 events.

7.5 Pileup correction

The default Monte Carlo samples used in this analysis were produced without any pileup of events. To estimate the impact of pileup on the measurement, the samples without pileup are compared to samples that include the simulation of a pileup scenario roughly corresponding to the data taken at the end of the 2010 LHC pp running.

An estimate for the expected number of pileup events in data can be calculated for each luminosity section (LS) from the instantaneous luminosity per proton bunch crossing of the LS, $\mathcal{L}_{\text{xing, LS}}$, the minimum bias cross section, σ_{mb}, and the bunch crossing rate, $\mathcal{R}_{\text{xing}}$, which is in the order of 11 kHz [48]:

$$N_{\text{PU / (xing, LS)}} = \frac{\mathcal{L}_{\text{xing, LS}} \cdot \sigma_{\text{mb}}}{R_{\text{xing}}} \tag{7.10}$$

Performing this calculation for all LS of all runs in the dataset, assuming a Poissonian distribution around the expected mean multiplicity of pileup events and weighting the number of pileup events from each LS and bunch crossing with the corresponding integrated luminosity, yields the expected pileup distribution shown in Fig. 7.11. It can be seen that the expected number of pileup events is around 1.2 for the first part of the dataset and, due to the increased instantaneous luminosities, almost 2.3 for the last part of the dataset. The weighted average for the whole dataset is 2.1 pileup events, i.e. slightly less than 93% of the value for the data taken at the end of the 2010 pp running.

Figure 7.11 also shows the multiplicity of good primary vertices. The mean multiplicity is 2.5 for the last part of the dataset, while it is 2.4 for the combined dataset, i.e. lower

by 4-5%. The mean multiplicity of good primary vertices in the simulated $t\bar{t}$ sample with pileup is 2.527 ± 0.005. Assuming that efficiency and fake rate of the vertex reconstruction are well simulated, these numbers support that the mean number of pileup events in our dataset is roughly 5% below the value from the simulated samples with pileup used in this analysis.

Performing 3,000 pseudo-experiments and comparing the mean fitted values from the samples that were simulated with pileup to the values from those without pileup, shifts of Δm_t =+ 0.7 GeV and ΔJES = -0.018 are observed. As a simple approach and assuming that the average amount of pileup in the 2010 data is indeed overestimated by 5% by the simulation, 95% of the Δm_t and ΔJES from the pseudo-experiments are taken to correct the measured m_t and JES for pileup in data. A systematic uncertainty of 25% will be assigned to these linear corrections.

7.6 Systematic Uncertainties

It is a virtue of the method used in this thesis that the JES uncertainty on the measured m_t is absorbed already into the uncertainty reported by the combined likelihood fit. The remaining systematic uncertainties are evaluated in this section and summarized in Table 7.3. For the evaluation of most systematic uncertainties, dedicated Monte Carlo samples are used. 3,000 pseudo-experiments are again performed in each case and the mean fit results compared to the results from the nominal scenario to estimate the effect of the variations in the input data.

- **Fit calibration:** As discussed in Sec. 7.4, the mean deviations of the m_t and JES residuals from 0 are taken as systematic uncertainties. The corresponding values are listed again in Table 7.3.
- **b Tagging:** In order to study the impact of uncertainties in the simulation of b tagging, the cut on the discriminator is varied from 1.74 to values of 1.19 and 2.29, which roughly covers the 11% uncertainty on the b-tagging efficiency discussed in Sec. 5.5.5. The shapes of ΔM_{32} and M2 with varied b tagging are shown in Fig. 7.12. The resulting effects on the fitted m_t and JES values can found in Table 7.4. Both for m_t and JES, the larger of the two variations listed here are taken for calculating the combined uncertainty in Table 7.3.
- **b JES:** In order to evaluate the impact of a relative shift of the JES of b jets with respect to the JES of light jets, the energy of all b-tagged jets is scaled up and down by 3%. The resulting shapes of ΔM_{32} and M2 are shown in Figure 7.13 and the effects of the $\pm$3% relative shifts between light and b JES on the fitted m_t and JES values are given in Table 7.5. Both for m_t and JES, the larger of the two variations listed here is taken for calculating the combined uncertainty in Table 7.3.

Table 7.3: List of systematic uncertainties.

	δm_{top} (GeV)	δJES
Fit calibration	0.1	0.004
b tagging	0.2	0.003
b JES	2.6	0.002
p_T and η dependent JES	0.3	0.004
Jet energy resolution	0.2	0.005
Initial-state and final-state radiation	0.4	0.008
Factorization scale	0.9	0.001
ME-PS matching threshold	0.2	0.003
Underlying event	0.7	0.001
Pileup	0.2	0.005
Parton distribution functions	0.2	0.002
Non-$t\bar{t}$ background	0.9	0.007
Total	3.1	0.015

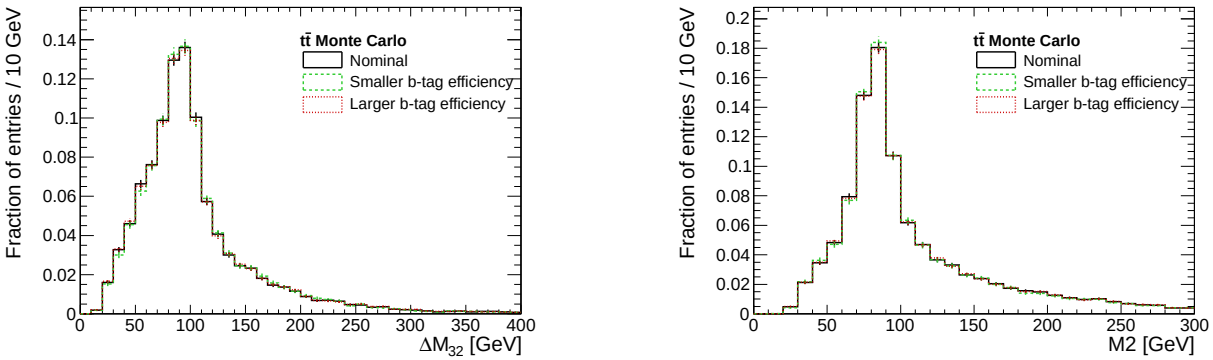

Figure 7.12: Distributions of ΔM_{32} (left) and M2 (right) in simulated $t\bar{t}$ events with varied b-tagging efficiencies.

Table 7.4: Systematic uncertainties from variations in the b-tagging efficiency.

	δm_{top} (GeV)	δJES
Larger b-tag efficiency	-0.2	$+0.001$
Smaller b-tag efficiency	-0.2	$+0.003$

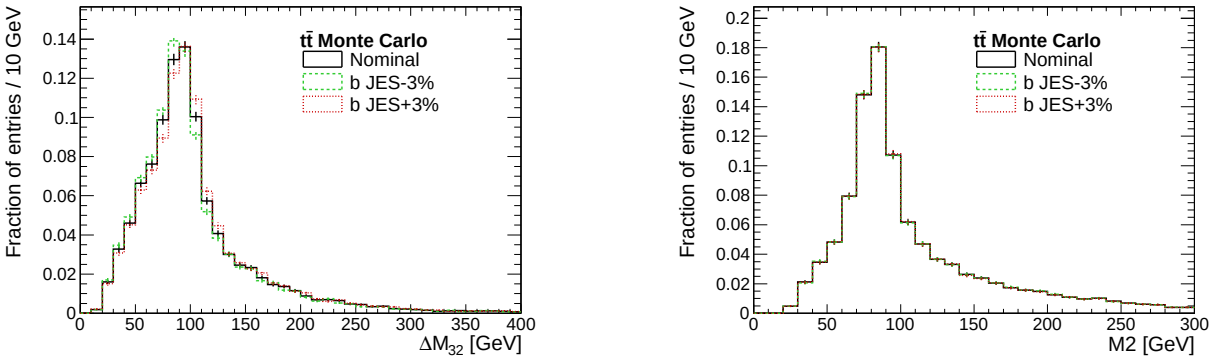

Figure 7.13: Distributions of ΔM_{32} (left) and M2 (right) in simulated $t\bar{t}$ events with the energy scale of b-tagged jets shifted by $\pm 3\%$.

Table 7.5: Systematic uncertainties from relative shifts of the energy scale of b-tagged jets with respect to the energy scale of untagged jets.

	δm_{top} (GeV)	δJES
b JES+3%	+2.6	−0.000
b JES−3%	−2.2	+0.002

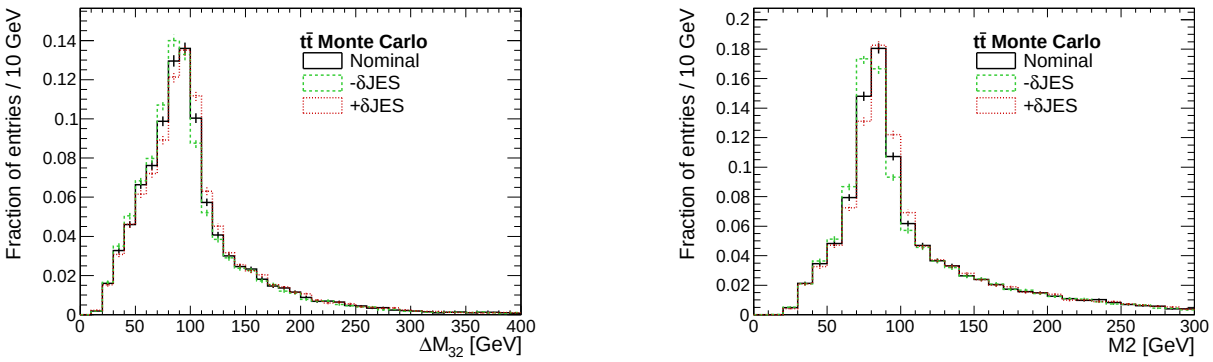

Figure 7.14: Distributions of ΔM_{32} (left) and M2 (right) in simulated $t\bar{t}$ events with the energy scale shifted according to the uncertainty on the default jet energy correction factors.

Table 7.6: Systematic uncertainties from p_T and η dependencies in the JES.

	δm_{top} (GeV)	δJES
$+\delta$JES	-0.1	-0.004
-δJES	$+0.3$	-0.003

- **p_T and η dependent JES:** To evaluate the impact of p_T and η dependencies in the JES, the jets are scaled up and down according to the official uncertainties on the default jet energy corrections, which are parametrized as a function of p_T and η [40]. This results in a larger rescaling of the energy for jets at low p_T or large η than for jets at high p_T or in the central detector region. The resulting shapes of ΔM_{32} and M2 are shown in Figure 7.14. As a result of the p_T and η dependent rescaling, the overall jet response in the sample relevant for this thesis changes by $\pm 2.6\%$. This is taken as the reference value for the fitted JES in this case. The resulting effects on the fitted m_t and JES values are given in Table 7.6. Both for m_t and JES, the larger of the two variations listed here is taken for calculating the combined uncertainty in Table 7.3.

- **Jet energy resolution:** Jet asymmetry measurements indicate that the jet energy resolution (JER) in data is about 10% worse than in the current detector simulation [44]. The uncertainty on these measurements is in the same order ($\pm 10\%$). To account for this in the calculation of the central values in this thesis, the energy of any jet after detector simulation is rescaled such that the difference with respect to the energy of the associated hadron-level jet is increased by 10%. To estimate the effect of the $\pm 10\%$ uncertainty, one can compare to the jets before the JER rescaling and to jets with a JER+20% rescaling with respect to the original simulation. The

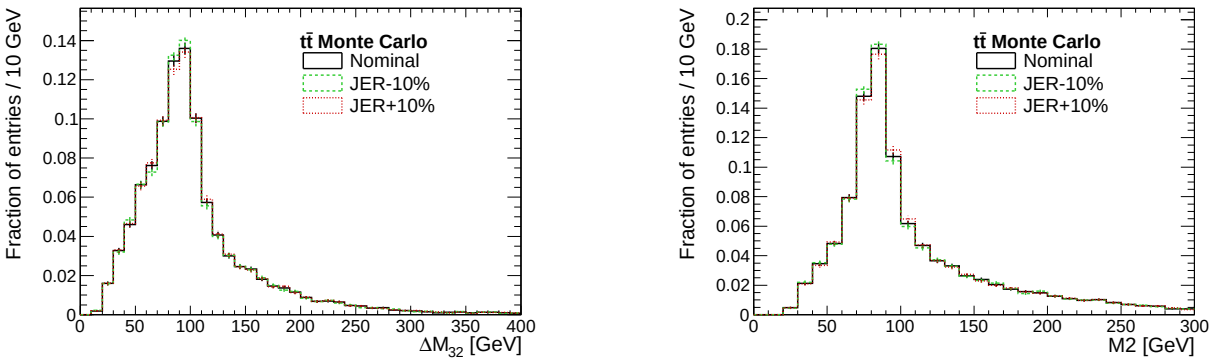

Figure 7.15: Distributions of ΔM_{32} (left) and M2 (right) in simulated $t\bar{t}$ events with varied jet energy resolution.

Table 7.7: Systematic uncertainties from variations of the jet energy resolution.

	δm_{top} (GeV)	δJES
JER+10%	−0.2	+0.005
JER−10%	+0.0	−0.003

resulting shapes of ΔM_{32} and M2 are shown in Fig. 7.15. The resulting differences in the fitted m_t and JES are given in Table 7.7. Both for m_{top} and JES, the larger of the two variations listed here are taken for calculating the combined uncertainty in Table 7.3.

- **Initial- and final-state radiation:** To estimate the effect of variations in the amount of initial-state radiation (ISR) and final-state radiation (FSR), a simulated $t\bar{t}$ sample with increased ISR and FSR and another one with reduced ISR and FSR are analyzed. The resulting shapes of ΔM_{32} and M2 are shown in Fig. 7.16 and the differences in the fitted m_t and JES values are given in Table 7.8. Both for m_t and JES, the larger of the two variations listed here are taken for calculating the combined uncertainty in Table 7.3.

- **Factorization scale:** To estimate the effect of the uncertainty on the factorization scale in the modeling of $t\bar{t}$ production, the Q^2 parameter in the simulation is varied by a factor of 0.25 and 4, corresponding to a scale variation of 0.5 and 2, respectively. The resulting shapes of ΔM_{32} and M2 are shown in Fig. 7.17. The differences in the fitted m_t and JES values are given in Table 7.9. Both for m_t and JES, the larger of the two variations listed here are taken for calculating the combined uncertainty in Table 7.3.

- **ME-PS matching threshold:** To estimate the effect of variations of the threshold

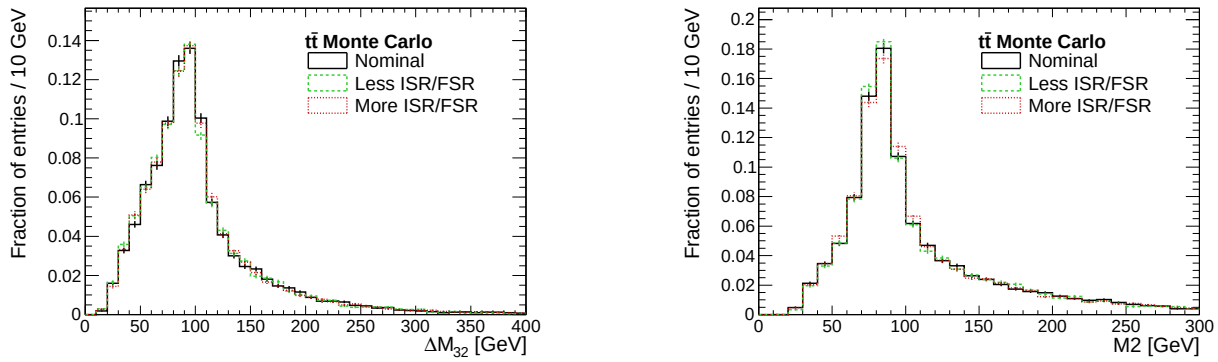

Figure 7.16: Distributions of ΔM_{32} (left) and M2 (right) in simulated $t\bar{t}$ events with varied initial- and final-state radiation.

Table 7.8: Systematic uncertainties from variations of the initial- and final-state radiation.

	δm_{top} (GeV)	δJES
More ISR/FSR	-0.4	$+0.008$
Less ISR/FSR	$+0.3$	-0.003

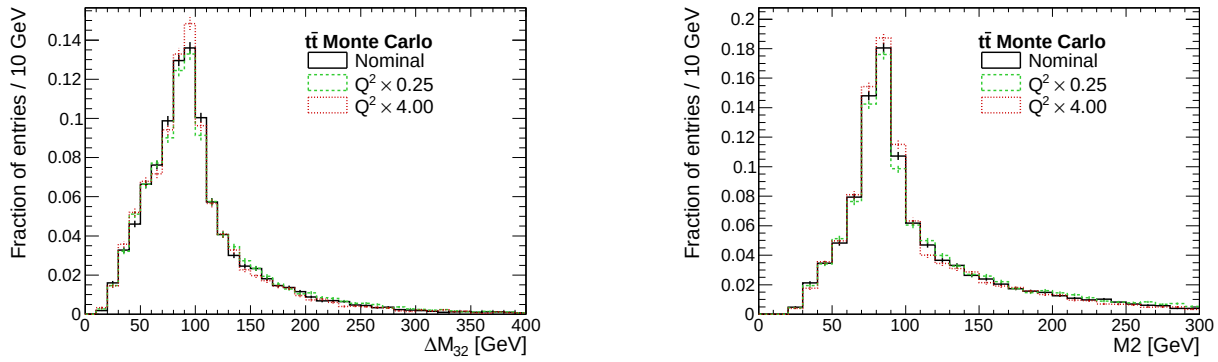

Figure 7.17: Distributions of ΔM_{32} (left) and M2 (right) in simulated $t\bar{t}$ events with varied factorization scale.

Table 7.9: Systematic uncertainties from variations of the factorization scale.

	δm_{top} (GeV)	δJES
$Q^2 \times 4.00$	-0.4	$+0.001$
$Q^2 \times 0.25$	$+0.9$	$+0.001$

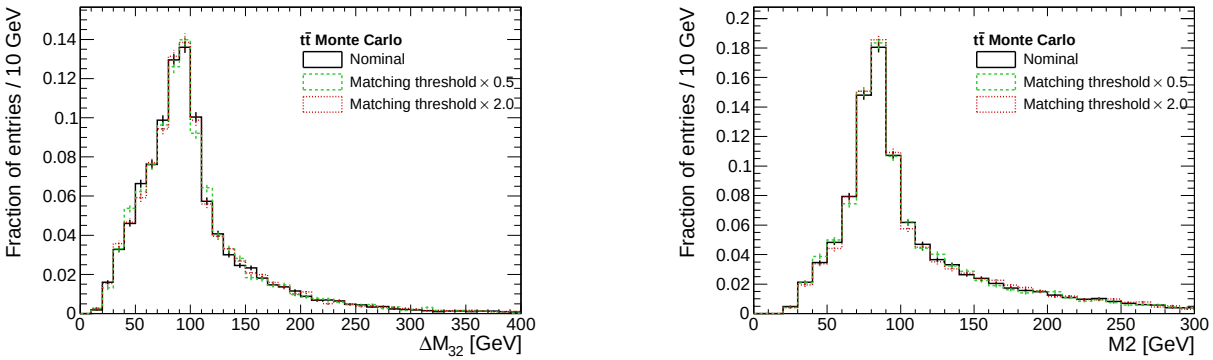

Figure 7.18: Distributions of ΔM_{32} (left) and M2 (right) in simulated $t\bar{t}$ events with varied ME-PS matching threshold.

used for the matching between the matrix-element level (ME) and parton showers (PS) in the $t\bar{t}$ simulation, the corresponding parameter is varied by a factor of 0.5 and 2.0. The resulting shapes of ΔM_{32} and M2 are shown in Fig. 7.18 and the differences in the fitted m_t and JES values are given in Table 7.10. Both for m_t and JES, the larger of the two variations listed here are taken for calculating the combined uncertainty in Table 7.3.

- **Underlying event:** To estimate the effect of differences in the underlying event simulation, $t\bar{t}$ samples produced with the underlying event tunes D6T and Z2 (see Chapter 4) are compared. The corresponding shapes of ΔM_{32} and M2 are shown in Fig. 7.19. The effects on the fitted m_t and JES values are listed in Table 7.3.

- **Pileup:** The shapes of ΔM_{32} and M2 from simulation with and without pileup are

Table 7.10: Systematic uncertainties from variations of the ME-PS matching threshold.

	δm_{top} (GeV)	δJES
Matching threshold $\times$ 2.0	$+0.0$	$+0.003$
Matching threshold $\times$ 0.5	$+0.2$	$+0.003$

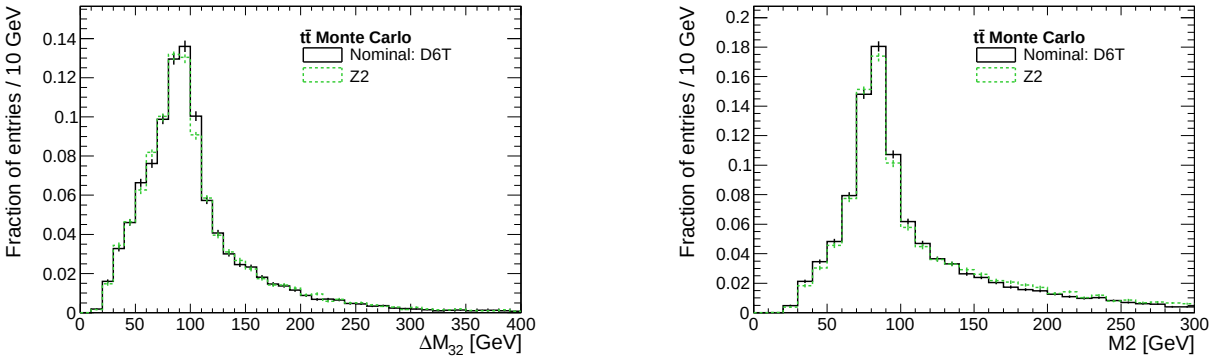

Figure 7.19: Distributions of ΔM_{32} (left) and M2 (right) in simulated $t\bar{t}$ events with two different underlying event tunes.

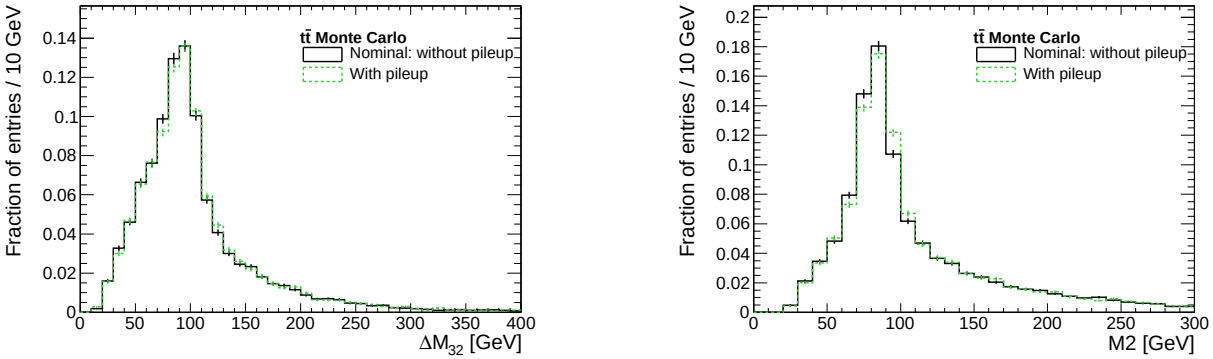

Figure 7.20: Distributions of ΔM_{32} (left) and M2 (right) in simulated $t\bar{t}$ events with and without pileup.

shown in Fig. 7.20. As discussed in Sec. 7.5, a simple pileup correction will be applied to correct the results for m_t and JES of the fit on data and, as listed in Table 7.3, 25% of the correction are taken as systematic uncertainty.

- **Parton distribution functions:** The Monte Carlo samples employed for this thesis were generated using the CTEQ 6.6 parton distribution functions (PDFs) [49]. The uncertainties of these PDFs can be described by 22 orthogonal parameters. Up and down variations of those parameters result in 2·22 additional PDFs, which can be used to evaluate the impact of the PDF uncertainties on the measurement, re-weighting the events according to the deviation of the respective PDF from the original one. The impact of the PDF variations on the ΔM_{32} and M2 distributions is shown in Fig. 7.21. The resulting uncertainties on the fitted m_t and JES values, listed in Table 7.3, are calculated as half the quadratic sums of the differences from each of the 22 PDF pairs.

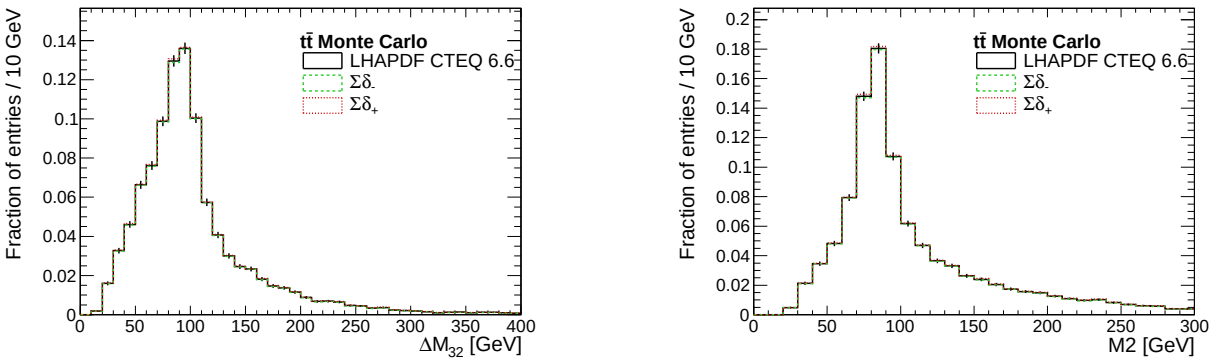

Figure 7.21: Effect on the uncertainties in the PDFs on the distributions of ΔM_{32} (left) and M2 (right) in simulated $t\bar{t}$ events.

Table 7.11: Impact of non-$t\bar{t}$ backgrounds on the measurement.

	δm_{top} (GeV)	δJES
88% $t\bar{t}$ + 12% $W \to l\nu$ (pre-tag)	+0.9	−0.002
88% $t\bar{t}$ + 12% single top (t channel)	+0.6	+0.007
88% $t\bar{t}$ + 12% associated tW production	+0.9	−0.001

- **Non-$t\bar{t}$ background:** As detailed in Chapter 5, a fraction of 6% non-$t\bar{t}$ background is expected after requiring two b-tagged jets in the event selection. To be conservative, 12% non-$t\bar{t}$ events, i.e. twice the expectation, are taken to study the effect of background contamination on the fitted m_t and JES values. Successively, three different processes are taken to model the full non-$t\bar{t}$ background: single-top production in the t channel, associated tW production and, finally, inclusive W+jets. For the latter, the pre-tagged sample is analyzed, assuming that the b-tag requirements do not lead to major changes in the shapes of the ΔM_{32} and M2 distributions in the case of W+jets. For a given M3, one of the three possible M2 that could be chosen when neglecting b tagging is picked randomly for W+jets in the pseudo-experiments. The shifts in the fitted m_t and JES values due to the contamination with non-$t\bar{t}$ events are listed in Table 7.11. Both for m_t and JES, the largest effect among the three background processes is taken for calculating the combined uncertainty in Table 7.3.

Adding in quadrature the uncertainties discussed above, results in a combined systematic uncertainty of 3.1 GeV and 0.015 for m_t and JES, respectively.

7.7 Results on Data

Performing the combined unbinned maximum likelihood fit to the data yields:

$$\begin{aligned} m_t &= 167.8 \pm 7.1(\text{stat+JES}) \pm 3.1(\text{syst}) \text{ GeV} \\ \text{JES} &= 1.048 \pm 0.040(\text{stat+}m_t) \pm 0.015(\text{syst}) \end{aligned}$$

The ΔM_{32} and M2 distributions in data overlaid with the expected distributions for the fitted values of m_t and JES are shown in Fig. 7.22. The negative log-likelihood curves as a function of m_t and JES are given in Fig. 7.23. The correlation coefficient between m_t and JES is -0.68. The 1σ uncertainties in the m_t-JES plane and the correlation between the two parameters are illustrated in Fig. 7.24.

Within the uncertainties, the obtained m_t is consistent with the very precise Tevatron average of 173.3 ± 1.1 GeV [14] and with both the CMS measurements in the dileptonic $t\bar{t}$ channel [15] and the ATLAS measurements in the lepton+jets channel [16]. The combined statistical and systematic uncertainty is compatible with the uncertainty of the ATLAS measurement when comparing to either the electron+jets or the muon+jets channel.

The obtained value of JES indicates that the data might prefer a small increase in the energy calibration for jets from light quarks. Although the deviation from unity might still be a statistical fluctuation, the same trend is observed within the b-tagged measurement of the $t\bar{t}$ cross section in the lepton+jets channel published by CMS [43], where a JES of 1.07 ± 0.06 results from a profile likelihood fit to the jet multiplicity distribution in data.

The same result of JES $= 1.048 \pm 0.040$ is found in this thesis when fitting only the M2 distribution. This shows that the JES value resulting from the combined fit to ΔM_{32} and M2 is fully determined already by the M2 distribution and therefore independent of the value of m_t.

As cross-checks for the simultaneous fit of m_t and JES, the data can also be used determine only one the two parameters from the combined fit to ΔM_{32} and M2. Fixing m_t at the current Tevatron average of 173.3 GeV and varying it by the corresponding uncertainty of ± 1.1 GeV, results in:

$$\text{JES} = 1.027 \pm 0.031(\text{stat}) \pm 0.004(m_t)$$

Fixing the JES at unity and varying it by $\pm 3.1\%$ (cf. Appendix G) yields:

$$m_t = 174.4 \pm 5.3(\text{stat}) \pm 3.8(\text{JES}) \text{ GeV}$$

Adding in quadrature the statistical uncertainty and the JES uncertainty gives in this case a value of 6.5 GeV, which is only slightly smaller than the 7.1 GeV uncertainty on m_t from the simultaneous fit of m_t and JES. This demonstrates the strength of the

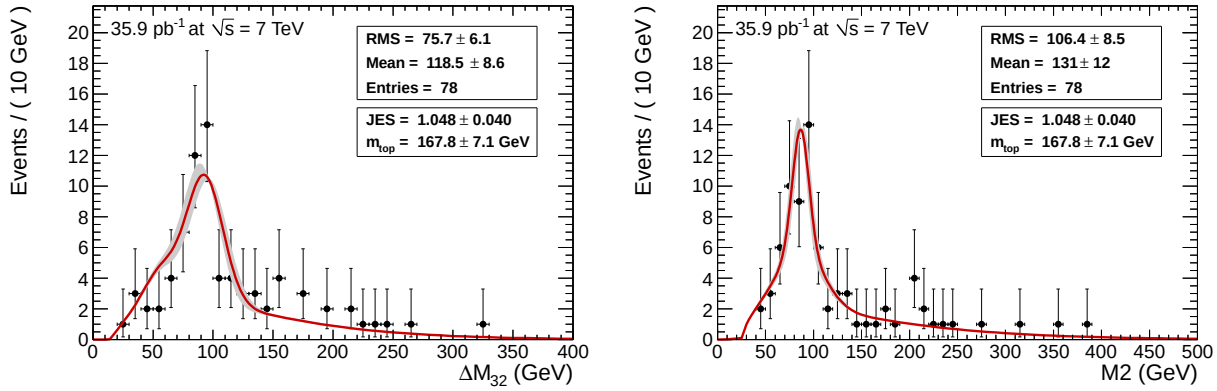

Figure 7.22: Distributions of ΔM_{32} (left) and M2 (right) in data overlaid with the expected distributions using m_t and JES as determined in the combined fit to the unbinned data.

employed technique: two parameters, m_t and JES, are measured using the same data, without significantly increasing the individual uncertainties.

Note that the fit uncertainties could be further reduced when adding a third likelihood term to Eq. 7.5 that constraints the JES to unity with a Gaussian uncertainty of $\sigma = 3.1\%$, based on the results obtained from other jet measurements at CMS and studies in simulated events. That would imply that the light flavor JES tested by this measurement is actually the same as the JES referred to by the other analyses, which has not been assumed for the results presented here.

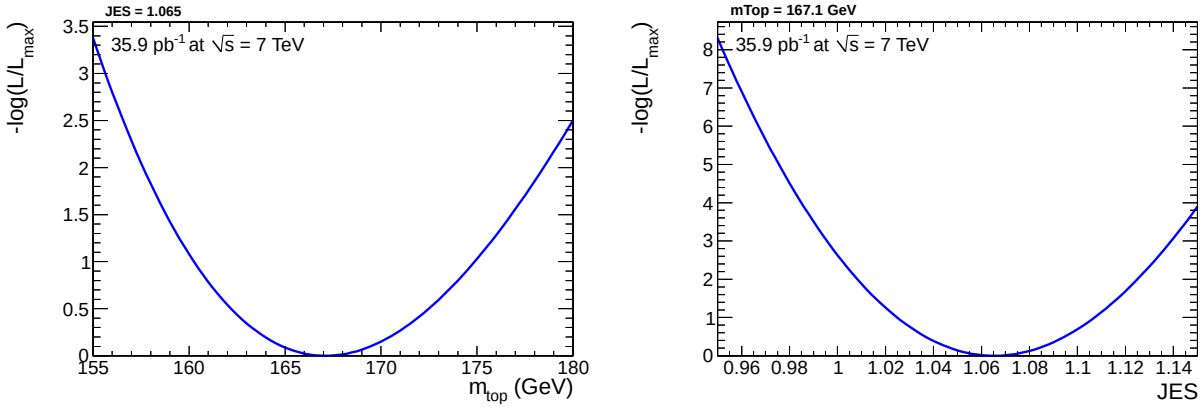

Figure 7.23: Negative log-likelihood curves as a function of m_t (left) and JES (right) for the combined fit on data. Note that these log-likelihood scans are performed before applying the pileup correction, which would result in a simple linear shift for both m_t and JES.

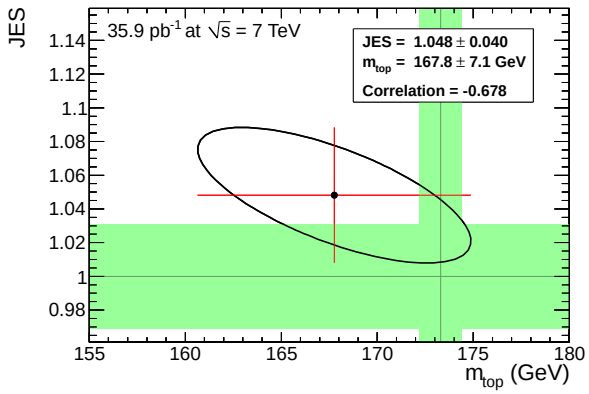

Figure 7.24: Error ellipse in the m_t-JES plane, illustrating the 1σ uncertainties and the correlation between the values that result from the combined fit on data. For comparison, the Tevatron m_t average and the default CMS JES are shown with the corresponding uncertainties as shaded bands. See Appendix G concerning the uncertainty on the default JES.

Chapter 8

Summary and Outlook

In this thesis, a simultaneous measurement of the top quark mass, m_t, and the jet energy scale (JES) in muon+jets events is presented, using data collected by the CMS detector at the LHC in the year 2010. It is one of the first measurements of m_t in pp collisions at $\sqrt{s} = 7$ TeV and the first complete m_t measurement in the lepton+jets channel at CMS.

Including b-tagging information in the event selection as well as in the reconstruction of dijet and trijet masses results in an estimated fraction of only 6% non-$t\bar{t}$ events in the final sample and good resolutions of the reconstructed M3 and M2 as estimators for the masses of top quarks that decayed hadronically and of the corresponding W boson, respectively. The method employed here for simultaneously measuring m_t and JES is similar to a measurement based on template fits in the lepton+jets channel developed by the CDF Collaboration [46]. The main differences are that no per-event fitting of the kinematics is performed in this thesis and that the mass difference ΔM_{32} = M3 - M2 is used together with M2 instead of using the reconstructed W boson and top quark masses directly. The motivation for choosing ΔM_{32} is that M3 and M2 were found to be highly correlated while there is only a modest correlation between ΔM_{32} and M2, where the former provides the information on m_t and the latter constraints the JES. Pseudo-experiments show an excellent linearity of the template fits in this thesis for both m_t and JES. The dominant systematic uncertainty on m_t amounts to 2.6 GeV and arises from relative shifts of the b JES with respect to the energy scale of jets from light quarks.

78 events are found in an integrated luminosity of 35.9 pb^{-1} when analyzing the full 2010 pp dataset and requiring two b-tagged jets per event. The results of the combined unbinned likelihood fit of ΔM_{32} and ΔM_{32} are:

$$\begin{aligned} m_t &= 167.8 \pm 7.1(\text{stat+JES}) \pm 3.1(\text{syst}) \text{ GeV} \\ \text{JES} &= 1.048 \pm 0.040(\text{stat}) \pm 0.015(\text{syst}) \end{aligned}$$

The same result for the JES is found when fitting only the M2 distribution. This shows that

the measured JES value is fully determined already by the M2 distribution and therefore independent of the value of m_t.

Within the uncertainties, the obtained result for m_t is consistent with the very precise Tevatron average of 173.3 ± 1.1 GeV [14] and with both the CMS measurements in the dileptonic $t\bar{t}$ channel [15] and the ATLAS measurements in the lepton+jets channel [16]. The combined statistical and systematic precision reached in this thesis is compatible with the precision of the ATLAS measurement when comparing to the electron+jets or muon+jets channel separately.

Although the precision of the measurement presented here is still significantly worse than the high precision reached in Tevatron measurements, it can be seen as one of the first independent cross-checks for the measurements of m_t performed at the Tevatron and, most of all, as a benchmark on the way to more precise measurements of m_t at CMS. In general, the determination of the JES in data using $t\bar{t}$ events is an important part in the preparation for precision measurements that include jets in such event topologies.

The JES result obtained within this thesis could be compared to the findings of the b-tagged measurement of the $t\bar{t}$ cross section in the lepton+jets channel published by CMS [43], where a JES of 1.07 ± 0.06 results from a profile likelihood fit to the jet multiplicity distribution in data. Both JES values suggest that the data prefer a small increase in the energy calibration for jets from light quarks.

The precision of the measurement presented here is still limited by the statistical uncertainty. The 2011 data-taking at the LHC has already begun and drastic increases in the instantaneous luminosity are expected within the near future, which could allow for the collection of up to several fb^{-1} within this year. The uncertainties on the fitted m_t and JES are expected to fall below the current level of systematic uncertainties in this measurement already at an integrated luminosity of roughly 200 pb^{-1}. Apart from this, the size of the dataset could be increased by a factor of 2, thereby also reducing significantly the statistical uncertainty, when adding the electron+jets to the muon+jets channel. Furthermore, it should be possible to increase the precision of the measurement presented here by minimizing the combinatorial background in the reconstructed masses. This could be achieved, for example, when choosing the best jet combination with a multivariate technique.

As soon as the statistical uncertainty decreases, the size of the systematic uncertainties will become more important. The technique presented here provides a constraint on the energy scale of light jets. This could be even more valuable when aiming at precision measurements of m_t with larger datasets. However, it still depends on the understanding of the energy scale of b quarks. The systematic uncertainty due to pileup events, which at the moment is relatively small in this measurement, might grow, at least temporarily, with the 2011 data given the unprecedented instantaneous luminosities at which the LHC operates.

After completion of this thesis, a measurement of m_t in the 2010 data using the ideogram method and both the muon+jets and the electron+jets channel has been presented to the CMS Collaboration. The precision of that measurement, which is foreseen to be made public in the near future [1], almost reaches the level of precision of the best measurements performed at the Tevatron so far. Despite this progress and the large amount of data that is already being recorded, it will be very challenging to really reach or even surpass the precision of the Tevatron experiments. The crucial aspects will be the correct handling of the increasing amount of pileup and, finally, still the understanding of the energy scales of b and light jets. In this context, a measurement following the technique presented in this thesis would again provide very valuable results.

Acknowledgments

The studies summarized in this thesis were performed within the group led by Prof. Dr. Peter Schleper and Prof. Dr. Robert Klanner. I am grateful to both for providing excellent conditions of work and for their advice during the last years. With his enthusiasm, Peter set off the fire in me for the LHC data. And he knows how to kick an analysis with ideas at the right moment.

I am indebted to Prof. Dr. Thomas Müller from Karlsruhe for reading this thesis as second referee (despite the short time that was left until the date of my disputation) as well as to Prof. Dr. Johannes Haller for acting as second referee of the disputation.

I have to thank a large number of postdocs and students of our working group at the Hamburg University and of the DESY CMS group for their support and for many helpful discussions. Here, I am going to name only a few of them. Dr. Roger Wolf and Dr. Hartmut Stadie mainly guided me through this PhD project. Roger not only introduced me to top quark analyses but also to software development, which I enjoyed. He also taught me some useful lessons about the dynamics in large research collaborations like CMS. Hartmut took care of me and my work especially during the last months, dedicated to the jet energy scale validation and the top quark mass measurement. Furthermore, he always was a precious help on all these nasty problems related to programming and to computing in general. I have been asking Dr. Georg Steinbrück for advice on a variety of topics, including those not directly related to my analysis. Georg also reviewed the first draft of this thesis. Dr. Martijn Gosselink helped, while I was unavailable, to take the final steps for bringing the results of this thesis into a public document of CMS. Important partners for discussion about the physics of top quarks and of jets were Holger Enderle and Matthias Schröder. Now I will finally stop walking into their office, disturbing them with my questions. Over the last three and a half years, I shared the office with a number of colleagues. Most time I spent together with Kolja Kaschube and Torben Schum. We shared not only thoughts concerning our physics analyses but also enjoyed commenting anything else that came on our screens.

I am indebted to the CMS Collaboration as a whole and to many individual members (I don't dare to make an incomplete list). Special thanks go to the Top Quark and JetMET working groups for their feedback.

Successfully finishing a project like this thesis with two small kids at home is impossible without strong social support. I'd like to thank in particular my parents, my sister and my parents-in-law. My wife Gesche still had to carry the heaviest load. Especially in the final phase of this project, she put on hold many of her own needs and wants, released me from almost all domestic duties and often, when I needed it, she pushed me to focus yet another couple of hours on this thesis. But at the same time she also gave me always the best possibility to disconnect from the world of particle physics, to relax and to recover quickly.

Danke!

Appendix A

Taylor Expansion for the Energy Resolution Bias in Dijet Masses

In Sec. 6.1, a bias of dijet and trijet masses towards smaller values caused by the finite energy resolution is seen for cases in which there is no bias on the energy scale. Simple calculations are presented in the following to illustrate how energy resolutions propagate into dijet masses and that they can result in a bias towards smaller masses.

The Taylor expansion for a function of two variables is:

$$\begin{aligned} f(x,y) &= f(x_0,y_0) + (x-x_0)\frac{\partial f(x_0,y_0)}{\partial x} + (y-y_0)\frac{\partial f(x_0,y_0)}{\partial y} \\ &\quad + \frac{1}{2}\left[(x-x_0)^2\frac{\partial^2 f(x_0,y_0)}{\partial x^2} + 2(x-x_0)\frac{\partial^2 f(x_0,y_0)}{\partial x \partial y}(y-y_0)\right. \\ &\quad \left. + (y-y_0)^2\frac{\partial^2 f(x_0,y_0)}{\partial y^2}\right] + \dots \end{aligned}$$

With $x_0 = \langle x \rangle$ and $y_0 = \langle y \rangle$, one finds for the expectation value of this function:

$$\begin{aligned} \langle f(x,y) \rangle &\approx f(\langle x \rangle, \langle y \rangle) \\ &\quad + \frac{1}{2}\left[(\langle x^2 \rangle - \langle x \rangle^2)\frac{\partial^2 f(\langle x \rangle, \langle y \rangle)}{\partial x^2} + (\langle y^2 \rangle - \langle y \rangle^2)\frac{\partial^2 f(\langle x \rangle, \langle y \rangle)}{\partial y^2}\right] \\ &= f(\langle x \rangle, \langle y \rangle) + \frac{1}{2}\left[\sigma_x^2\frac{\partial^2 f(\langle x \rangle, \langle y \rangle)}{\partial x^2} + \sigma_y^2\frac{\partial^2 f(\langle x \rangle, \langle y \rangle)}{\partial y^2}\right] \end{aligned}$$

For $M(E_1, E_2) = \sqrt{aE_1E_2}$, this gives:

$$\frac{\partial M}{\partial E_1} = \frac{1}{2}\sqrt{\frac{aE_2}{E_1}} \qquad \text{and} \qquad \frac{\partial M}{\partial E_2} = \frac{1}{2}\sqrt{\frac{aE_1}{E_2}}$$

$$\frac{\partial^2 M}{\partial E_1^2} = -\frac{1}{4}\sqrt{\frac{aE_2}{E_1^3}} \qquad \text{and} \qquad \frac{\partial^2 M}{\partial E_2^2} = -\frac{1}{4}\sqrt{\frac{aE_1}{E_2^3}}$$

And:

$$\langle M(E_1, E_2)\rangle \approx \sqrt{a\,\langle E_1\rangle\,\langle E_2\rangle} - \frac{\sqrt{a}}{8}\left[\sigma_{E_1}^2\sqrt{\frac{\langle E_2\rangle}{\langle E_1\rangle^3}} + \sigma_{E_2}^2\sqrt{\frac{\langle E_1\rangle}{\langle E_2\rangle^3}}\right]$$

The negative sign in front of the second order term is due to the fact that $M(E_1, E_2) = \sqrt{aE_1E_2}$ is a concave function.

With $a = 2(1 - \cos\theta)$, the above expression corresponds to the expectation value for the invariant mass of two particles with mean energies $\langle E_1\rangle$ and $\langle E_2\rangle$ and an opening angle θ.

For the special case $\langle E_1\rangle = \langle E_2\rangle = \langle E\rangle$ and $\sigma_{E_1}^2 = \sigma_{E_2}^2 = \sigma_E^2$, the expression would become:

$$\langle M(E)\rangle \approx \sqrt{a}\,\langle E\rangle - \frac{\sqrt{a}}{8}\frac{\sigma_E^2}{\langle E\rangle}$$

Taking, as an example, $\langle E\rangle = 91.7$ GeV, $\sigma_E = 11.8$ GeV and $a = 0.769$, results in:

$$\langle M\rangle \approx 80.40\text{ GeV} - 0.17\text{ GeV}$$

Appendix B

Resolution Bias on the Energy Scale as a Function of the Parton p_T

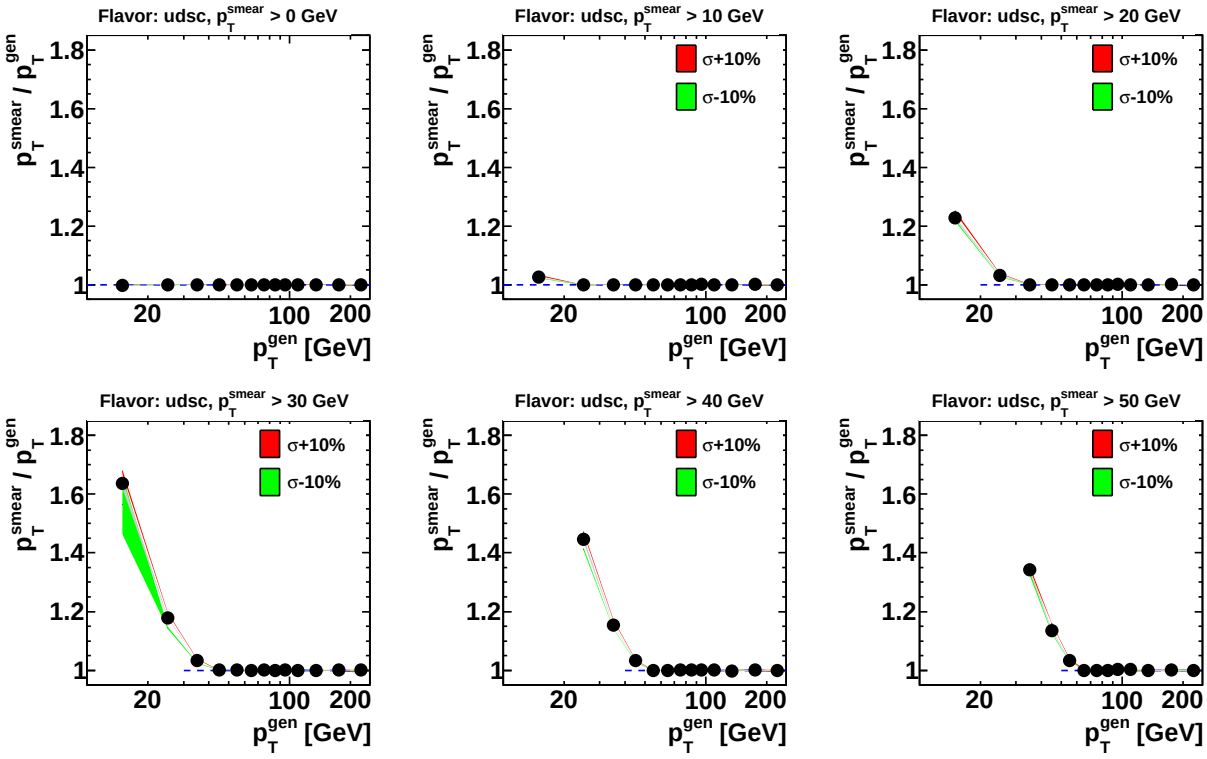

Figure B.1: Effect of the expected energy resolution on the apparent parton energy scale of u, d, s and c quarks, shown as a function of the true parton p_T and for six different selection cuts on the smeared parton p_T, from $p_{T,\mathrm{cut}}^{\mathrm{smear}} = 0$ GeV (upper left) to 50 GeV (lower right). See the caption to Fig. 6.3 for further details.

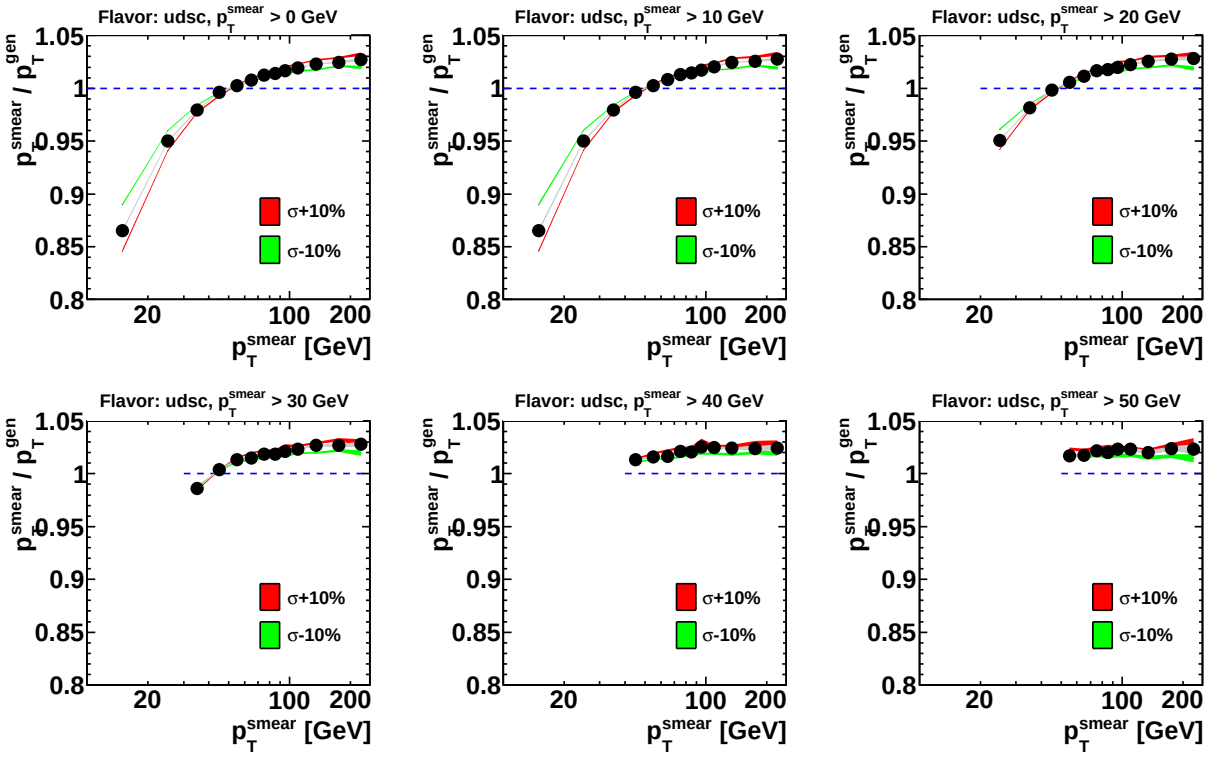

Figure B.2: Effect of the expected energy resolution on the apparent parton energy scale of u, d, s and c quarks, shown as a function of the smeared parton p_T and for six different selection cuts on the smeared parton p_T, from $p_{T,\mathrm{cut}}^{\mathrm{smear}} = 0$ GeV (upper left) to 50 GeV (lower right). See the caption to Fig. 6.3 for further details.

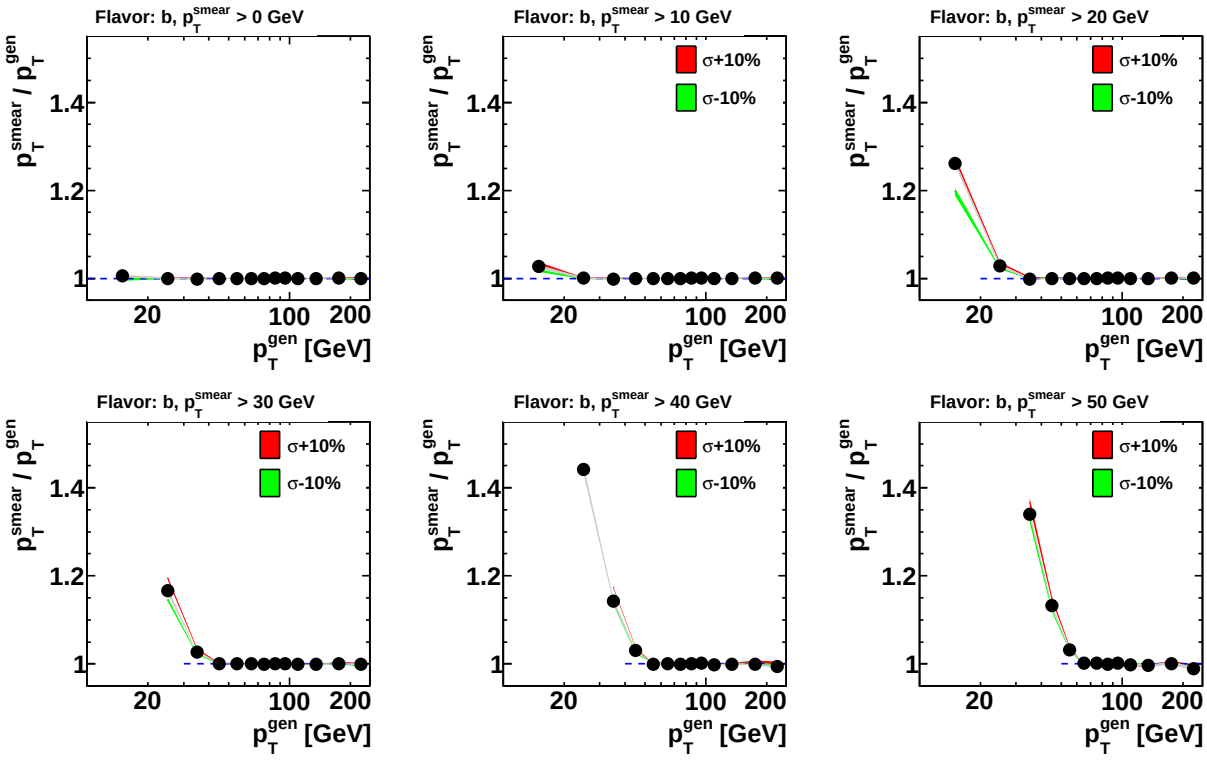

Figure B.3: Effect of the expected energy resolution on the apparent parton energy scale of b quarks, shown as a function of the true parton p_T and for six different selection cuts on the smeared parton p_T, from $p_{T,\mathrm{cut}}^{\mathrm{smear}} = 0$ GeV (upper left) to 50 GeV (lower right). See the caption to Fig. 6.3 for further details.

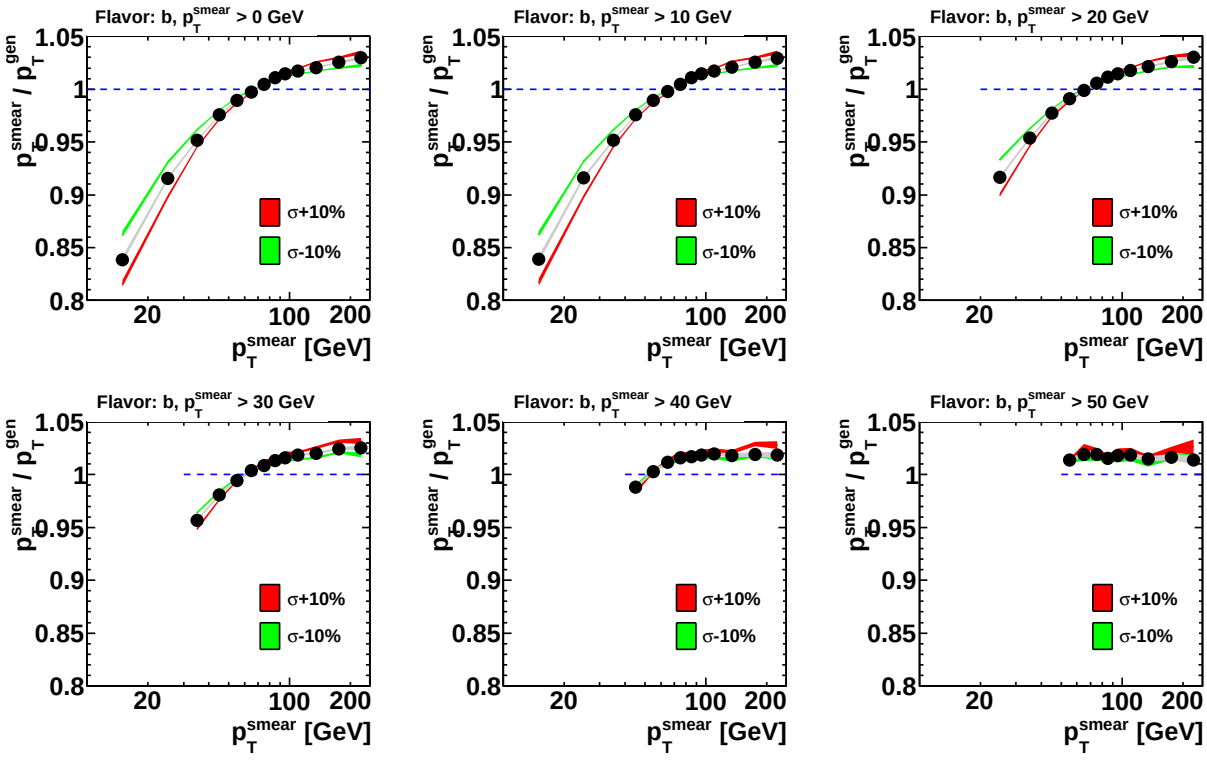

Figure B.4: Effect of the expected energy resolution on the apparent parton energy scale of b quarks, shown as a function of the smeared parton p_T and for six different selection cuts on the smeared parton p_T, from $p_{T,\mathrm{cut}}^{\mathrm{smear}} = 0$ GeV (upper left) to 50 GeV (lower right). See the caption to Fig. 6.3 for further details.

Appendix C

Resolution Bias on the W Boson Mass as a Function of the Parton p_T

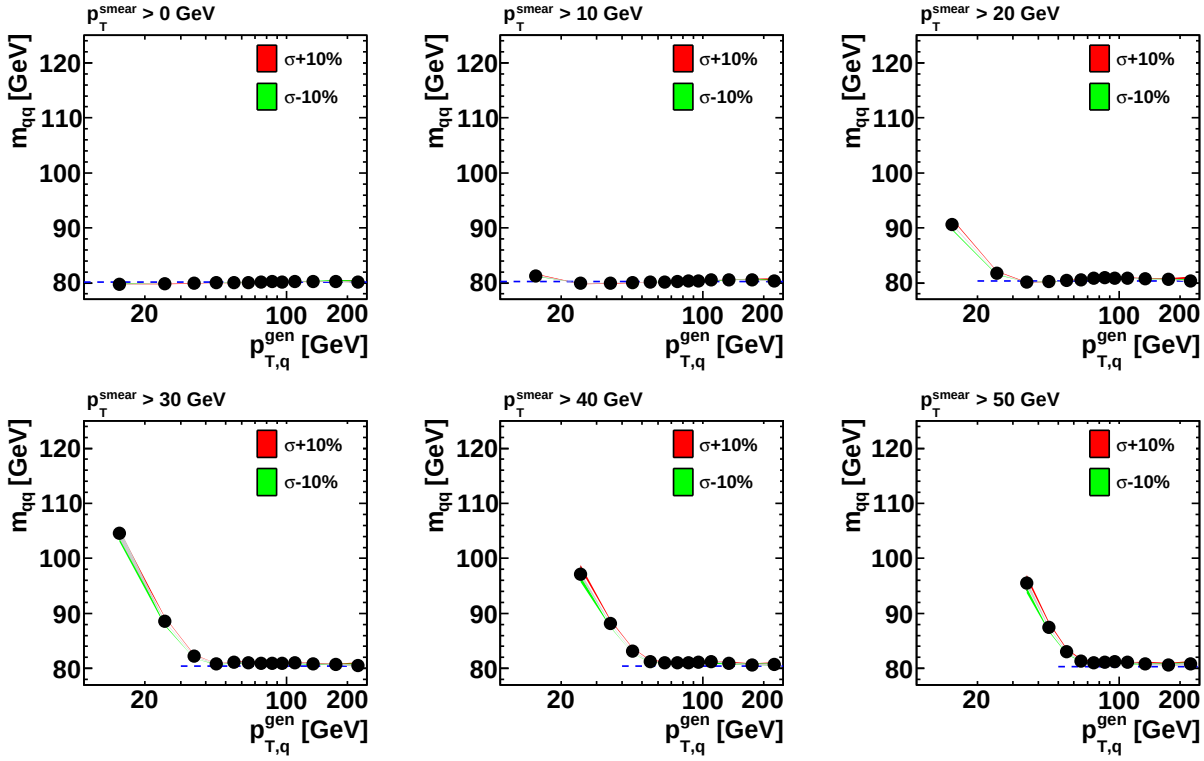

Figure C.1: Effect of the expected energy resolution on the reconstructed W boson mass, shown as a function of the true parton p_T and for six different selection cuts on the smeared parton p_T, from $p_{T,\mathrm{cut}}^{\mathrm{smear}} = 0$ GeV (upper left) to 50 GeV (lower right). See the caption to Fig. 6.3 for further details.

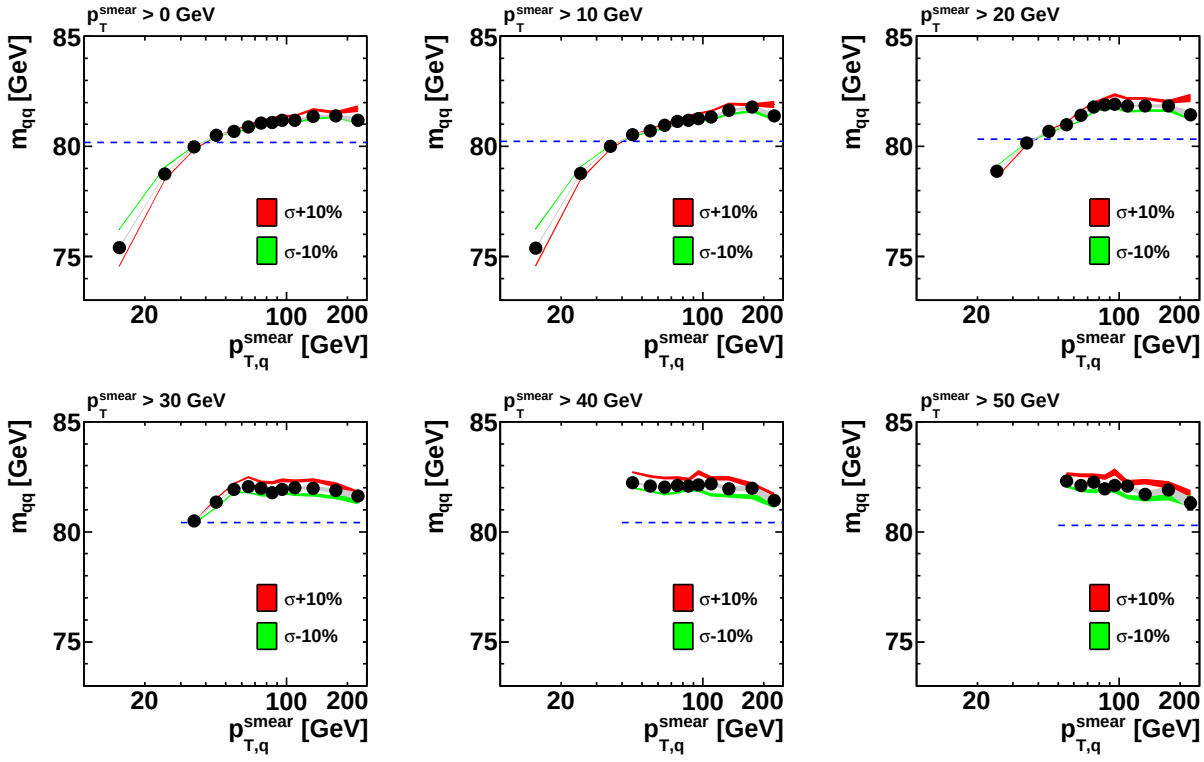

Figure C.2: Effect of the expected energy resolution on the reconstructed W boson mass, shown as a function of the smeared parton p_T and for six different selection cuts on the smeared parton p_T, from $p_{T,\mathrm{cut}}^{\mathrm{smear}} = 0$ GeV (upper left) to 50 GeV (lower right). See the caption to Fig. 6.3 for further details.

Appendix D

Resolution Bias on the Top Quark Mass as a Function of the Parton p_T

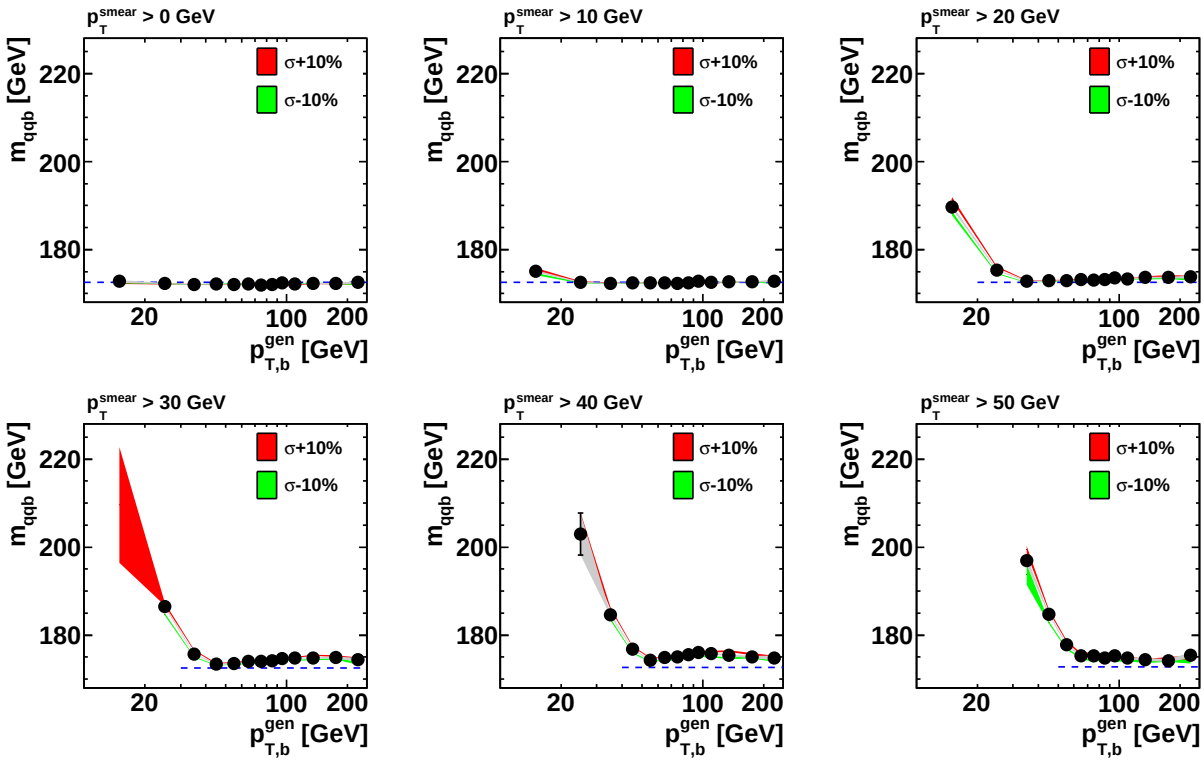

Figure D.1: Effect of the expected energy resolution on the reconstructed top mass, shown as a function of the true parton p_T and for six different selection cuts on the smeared parton p_T, from $p_{T,\mathrm{cut}}^{\mathrm{smear}} = 0$ GeV (upper left) to 50 GeV (lower right). See the caption to Fig. 6.3 for further details.

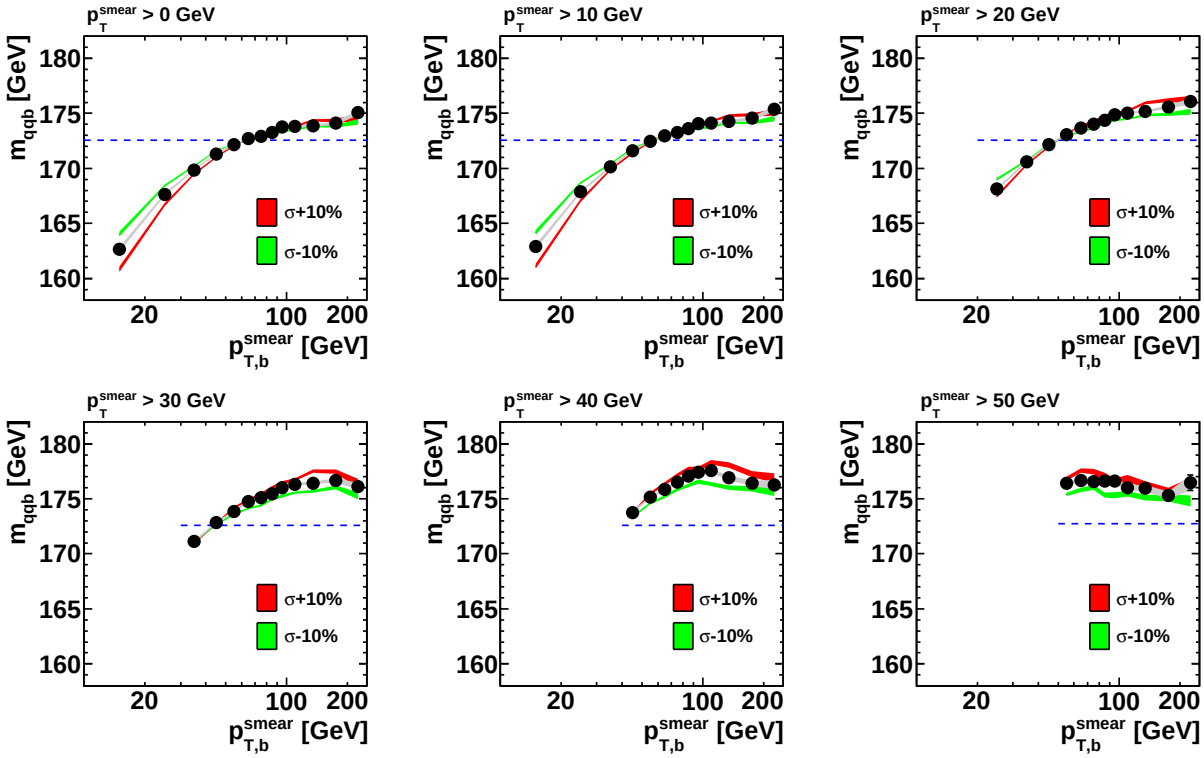

Figure D.2: Effect of the expected energy resolution on the reconstructed top mass, shown as a function of the smeared parton p_T and for six different selection cuts on the smeared parton p_T, from $p_{T,\mathrm{cut}}^{\mathrm{smear}} = 0$ GeV (upper left) to 50 GeV (lower right). See the caption to Fig. 6.3 for further details.

Appendix E

Template Parameters

On the following pages, the values of the parameters p_i of the template functions are listed (Table E.1) and the m_t and JES dependence of the resulting α_i is illustrated (Figures E.1 - E.3). More information on the template functions and their parameters can be found in Sections 7.2.1 and 7.2.2.

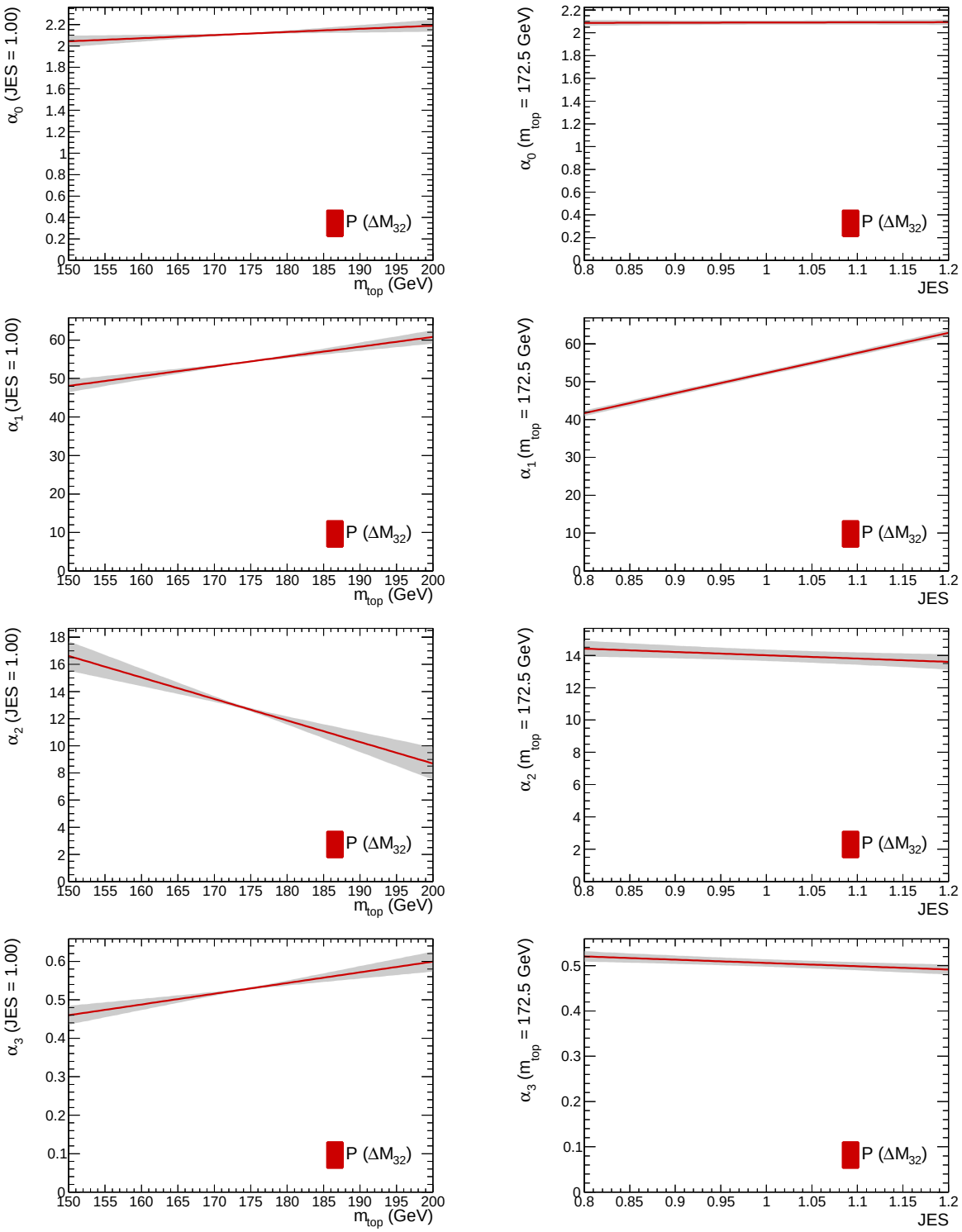

Figure E.1: Parameters α_0 (first row), α_1 (second row), α_2 (third row) and α_3 (fourth row) of the template function $P(\Delta M_{32})$, shown as a function of m_t (left) and JES (right).

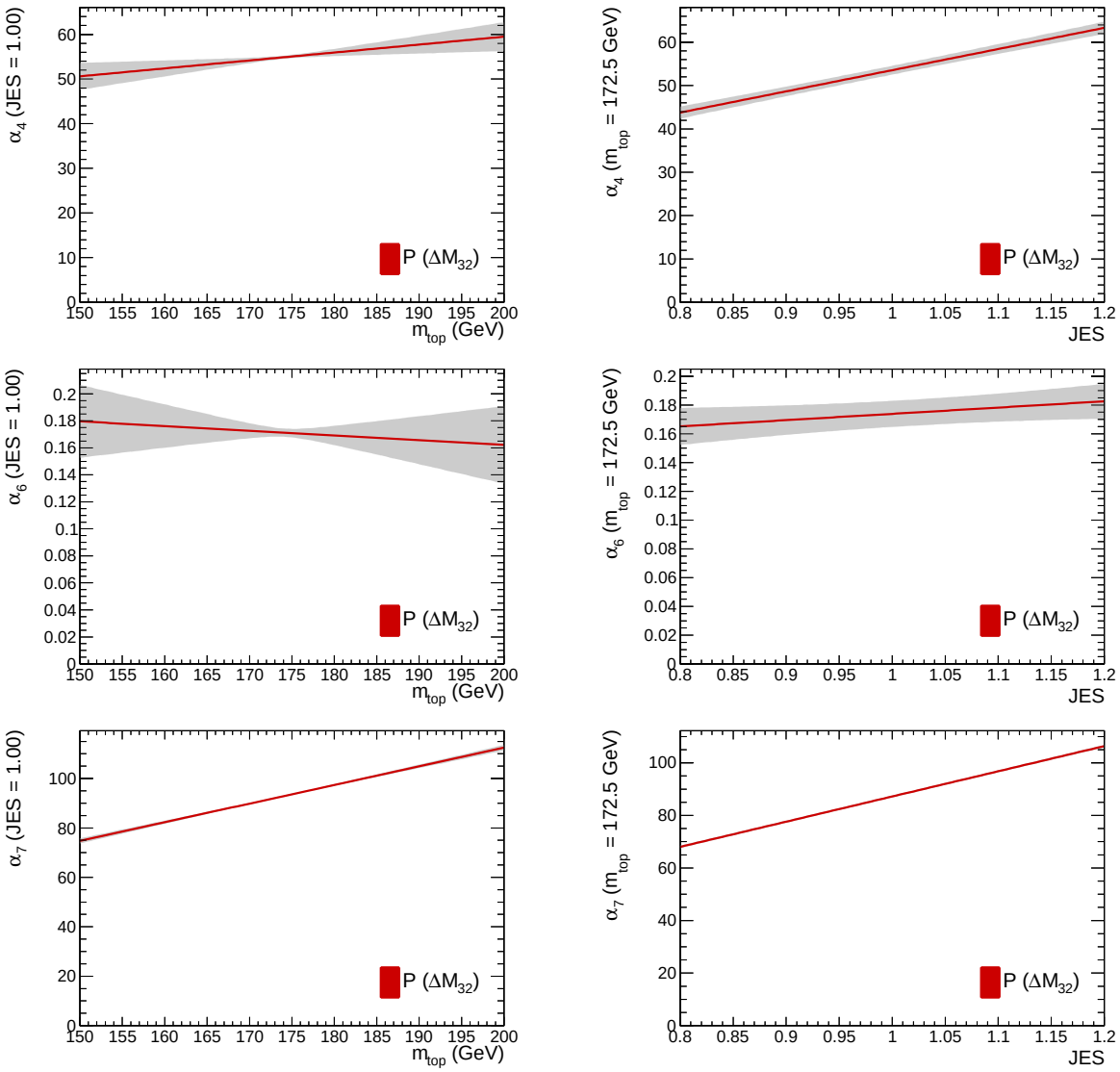

Figure E.2: Parameters α_4 (first row), α_6 (second row) and α_7 (fourth row) of the template function $P(\Delta M_{32})$, shown as a function of m_t (left) and JES (right).

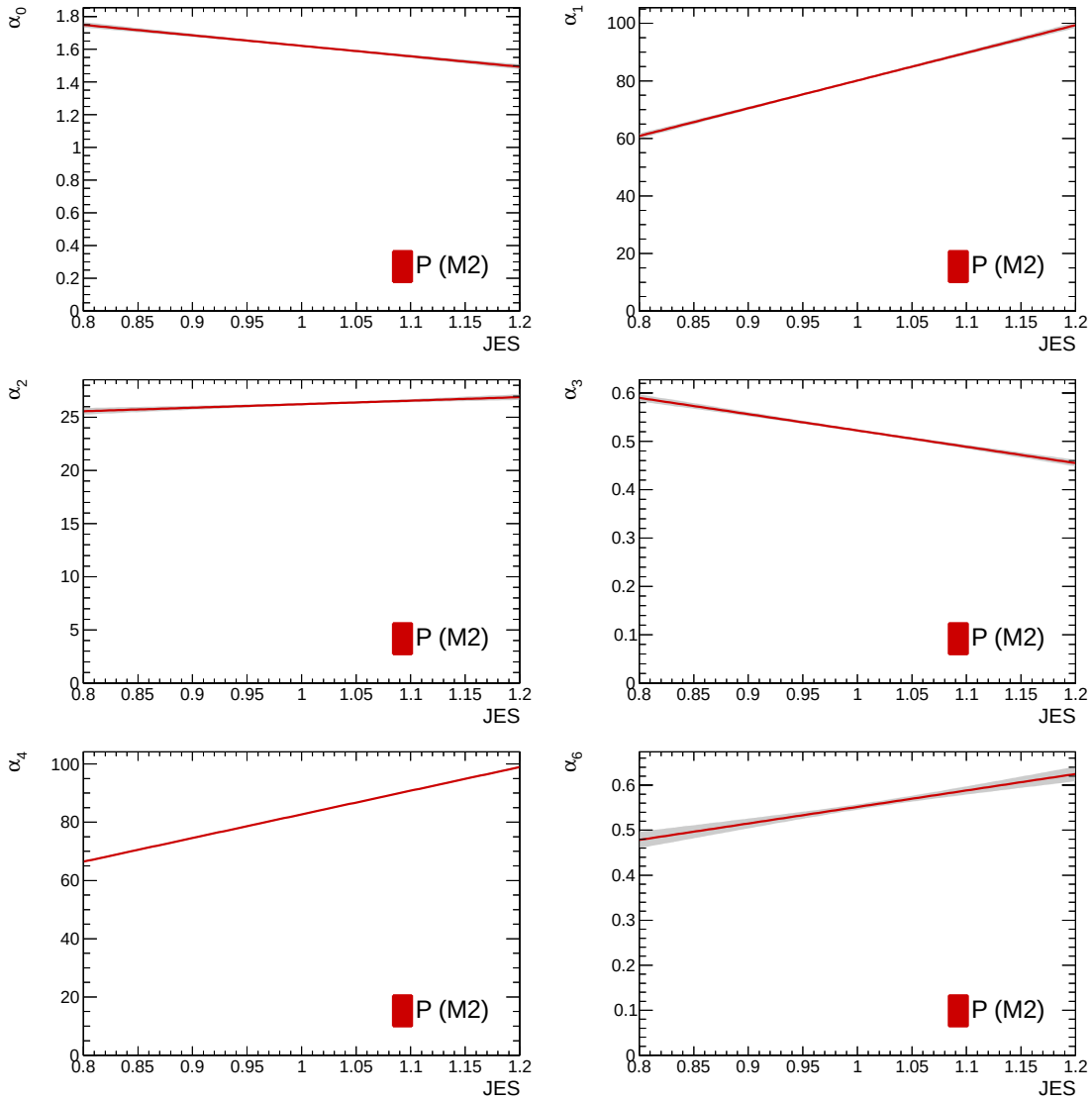

Figure E.3: Parameters α_0, α_1, α_2, α_3, α_4 and α_6 of the template function $P(\mathrm{M2})$, shown as a function of the JES.

Table E.1: Parameter values of the template functions $P(\Delta M_{32}; \mathrm{JES}, m_t)$ (on the left) and $P(\mathrm{M2}; \mathrm{JES})$ (on the right).

p_0	2.108 ± 0.022
p_1	53.80 ± 0.62
p_{10}	53.1 ± 7.3
p_{11}	-2.04 ± 2.2
p_{12}	-0.0722 ± 0.061
p_{13}	48.9 ± 6.9
p_{15}	0.044 ± 0.067
p_{16}	95.9 ± 2.0
p_{18}	0.0029 ± 0.0070
p_{19}	0.25 ± 0.18
p_2	13.06 ± 0.16
p_{20}	-0.1585 ± 0.067
p_{21}	0.0028 ± 0.0016
p_{22}	0.18 ± 0.17
p_{24}	-0.00035 ± 0.0017
p_{25}	0.754 ± 0.051
p_3	0.5227 ± 0.0062
p_4	54.61 ± 0.88
p_5	0.0578 ± 0.0028
p_6	0.1718 ± 0.0097
p_7	91.72 ± 0.24
p_8	0.02745 ± 0.00093
p_9	0.02 ± 0.27

p_0	1.620 ± 0.014
p_1	80.12 ± 0.74
p_{10}	96 ± 10
p_{11}	3.3 ± 1.7
p_{12}	-0.3372 ± 0.049
p_{13}	81.2 ± 1.1
p_{15}	0.37 ± 0.11
p_{18}	0.00
p_{19}	0.00
p_2	26.23 ± 0.12
p_{20}	0.00
p_{21}	0.00
p_{22}	0.00
p_{24}	0.00
p_3	0.5224 ± 0.0039
p_4	82.696 ± 0.081
p_5	0.0720 ± 0.0018
p_6	0.552 ± 0.012
p_7	0.00959 ± 0.00032
p_9	-0.640 ± 0.18

Appendix F

Residual and Pull Distributions

This section contains the residual distributions (Fig. F.1 and Fig. F.2) and the pull distributions (Fig. F.3 and Fig. F.4) of m_t and JES for the different points in the m_t-JES parameter space tested with pseudo-experiments. See Sec. 7.4 for further details.

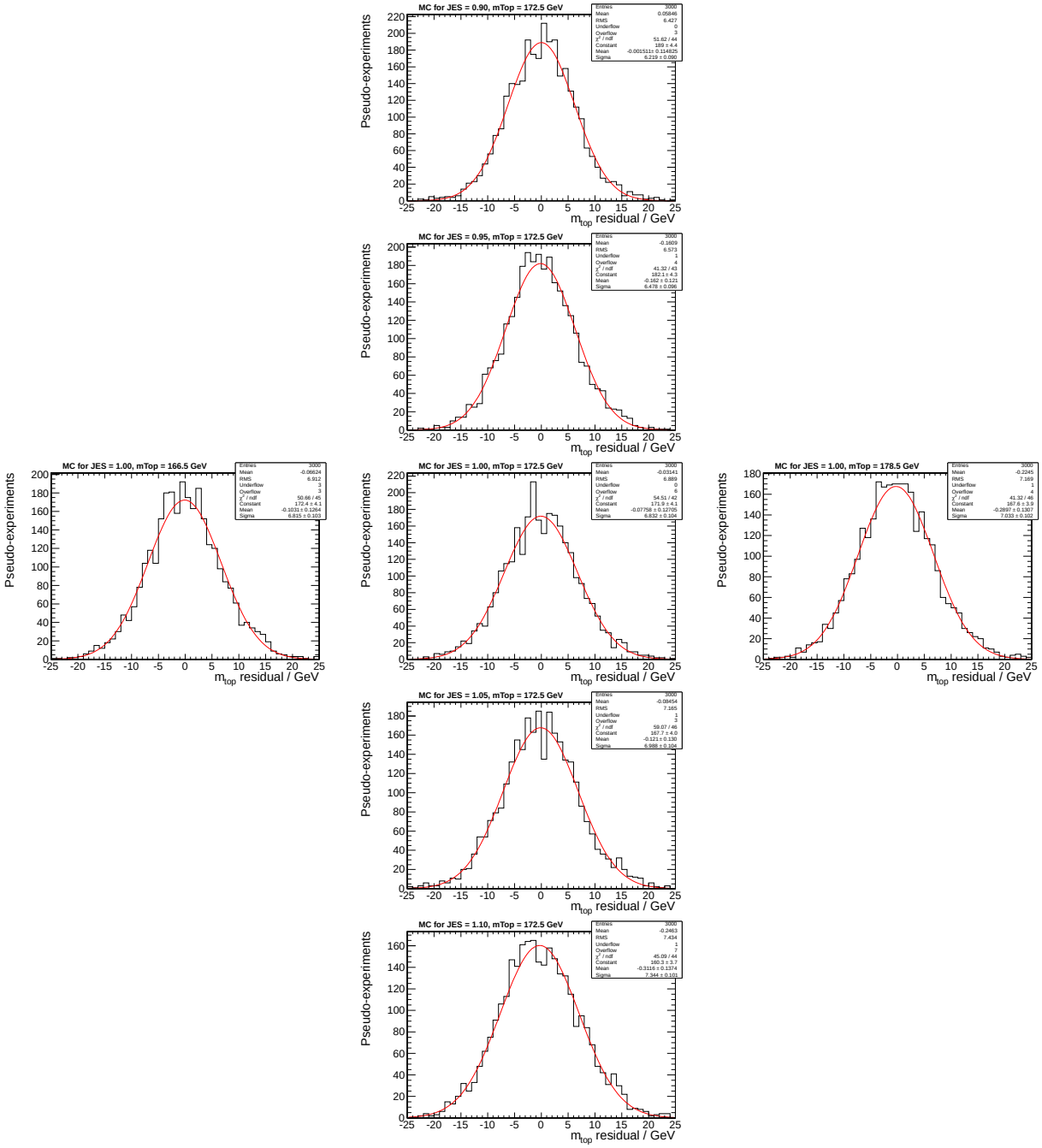

Figure F.1: m_t residuals for a generated m_t of 166.5 GeV (left), 172.5 GeV (center) and 178.5 GeV (right) and a generated JES of 0.90 (first row), 0.95 (second row), 1.00 (third row), 1.05 (fourth row) and 1.10 (fifth row).

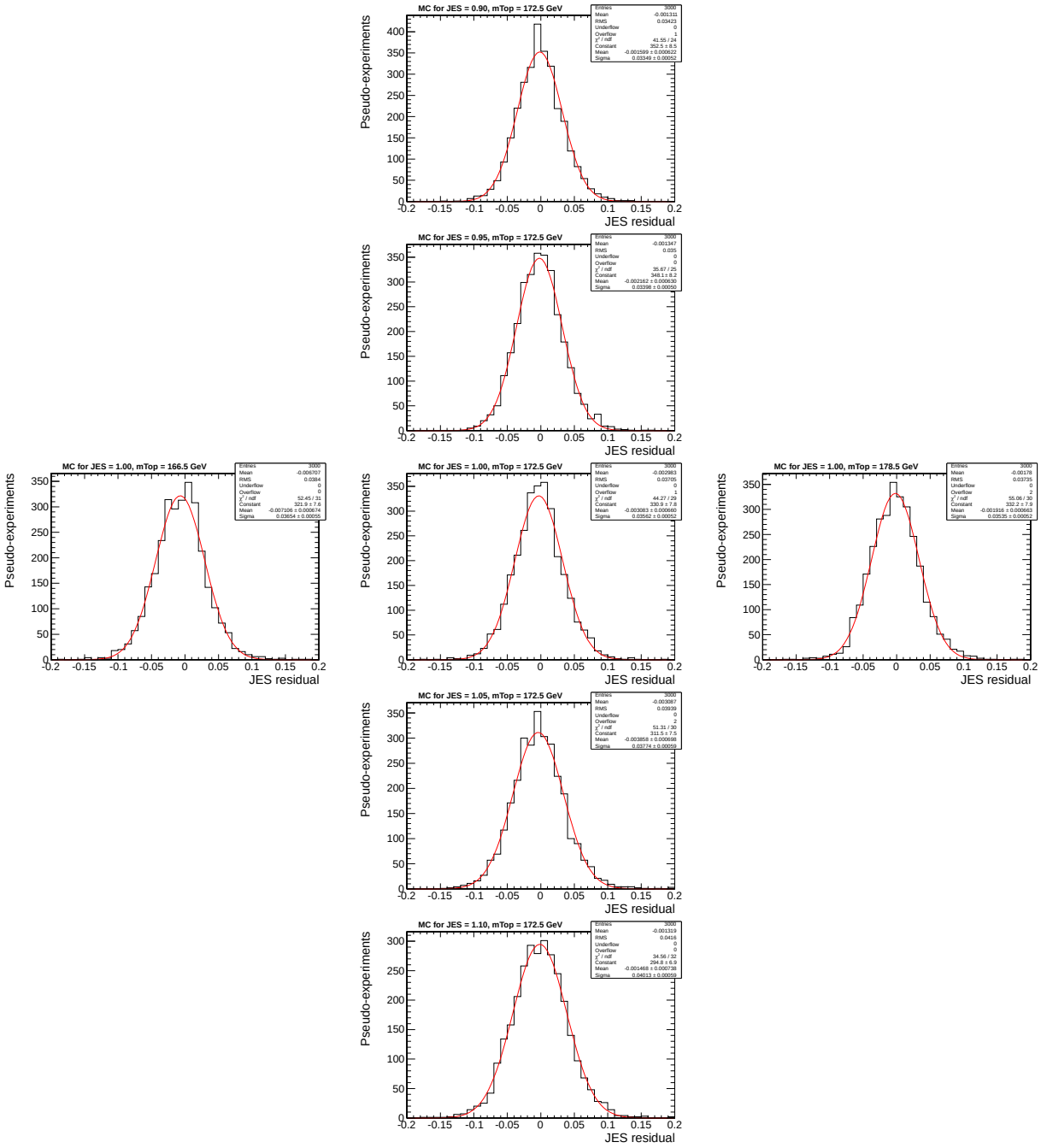

Figure F.2: JES residuals for a generated m_t of 166.5 GeV (left), 172.5 GeV (center) and 178.5 GeV (right) and a generated JES of 0.90 (first row), 0.95 (second row), 1.00 (third row), 1.05 (fourth row) and 1.10 (fifth row).

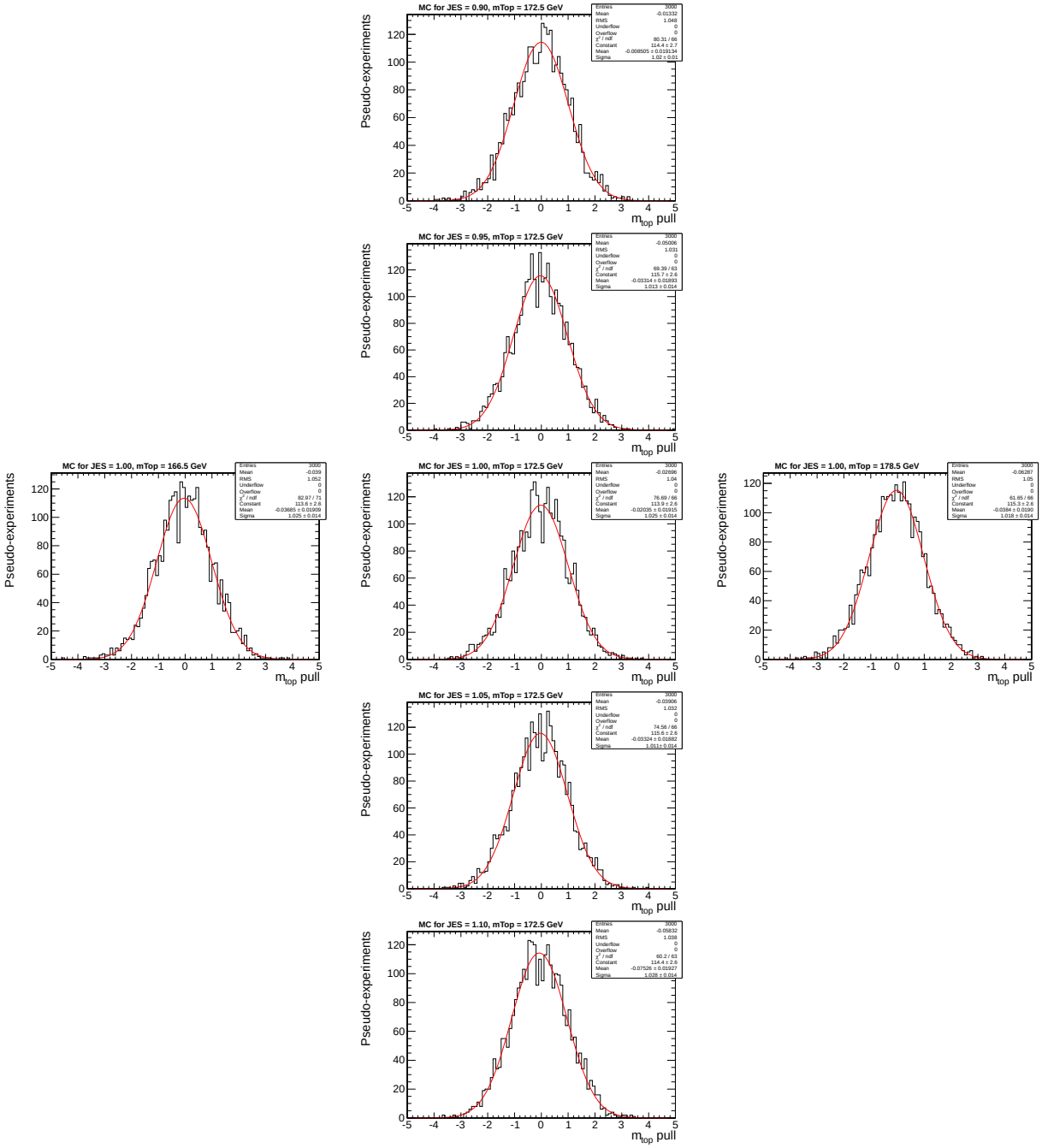

Figure F.3: m_t pulls for a generated m_t of 166.5 GeV (left), 172.5 GeV (center) and 178.5 GeV (right) and generated a JES of 0.90 (first row), 0.95 (second row), 1.00 (third row), 1.05 (fourth row) and 1.10 (fifth row).

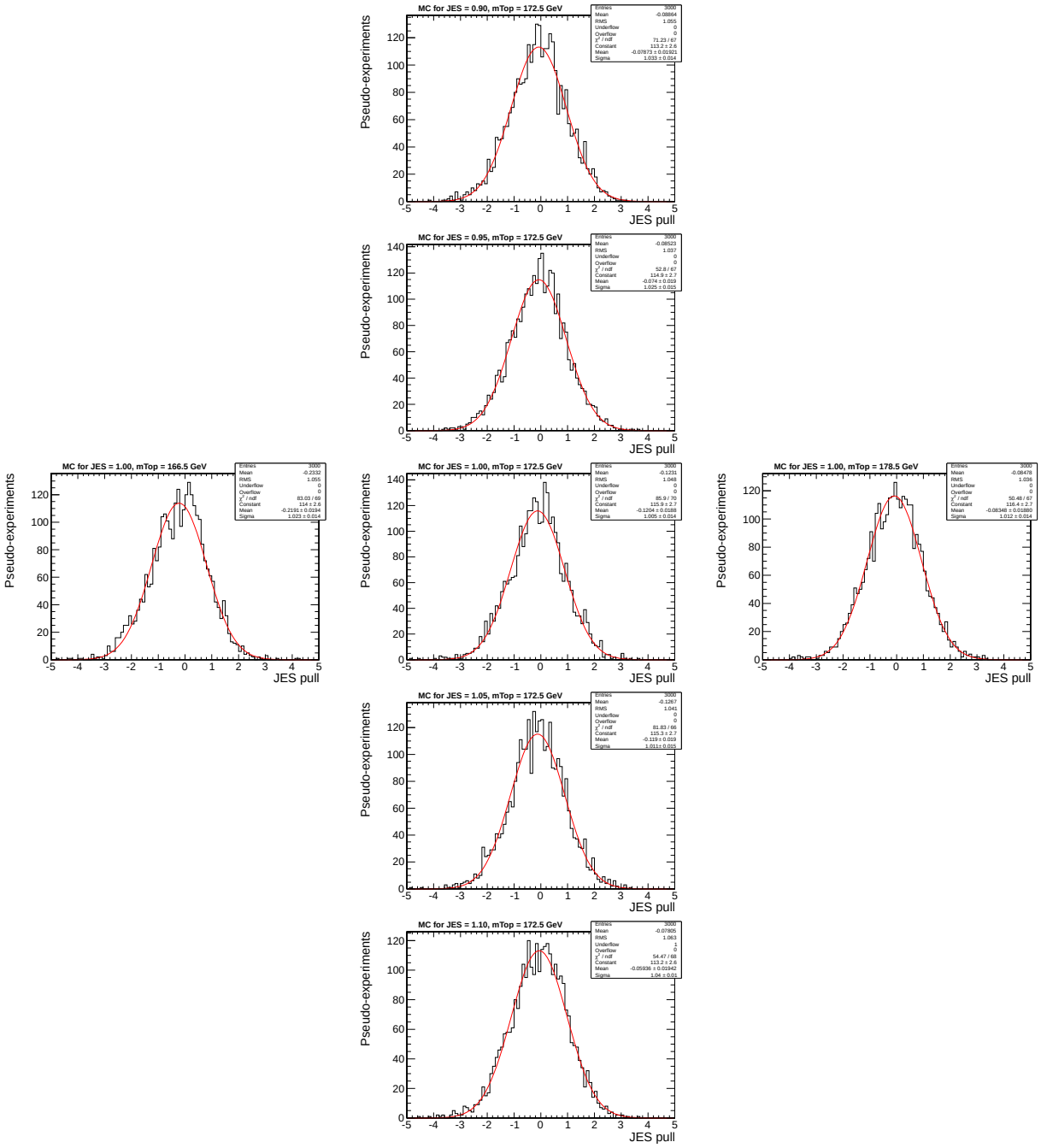

Figure F.4: JES pulls for a generated m_t of 166.5 GeV (left), 172.5 GeV (center) and 178.5 GeV (right) and a generated of JES = 0.90 (first row), 0.95 (second row), 1.00 (third row), 1.05 (fourth row) and 1.10 (fifth row).

Appendix G

Uncertainty on the Default Jet Energy Scale

The uncertainty of the jet energy corrections at CMS was determined as a function of the jet p_T and η [40]. As shown in Fig. G.1, an average uncertainty of 2.7% is found for the jets that were associated to the decay of a hadronic top quark in this thesis. Within the limited statistics of the final sample, there are no significant differences between the average uncertainties for light and b jets. Adding in quadrature 1.5% to account for differences between the software versions in which the jet energy corrections were determined and in which the data for this thesis were analyzed, yields an uncertainty of 3.1%

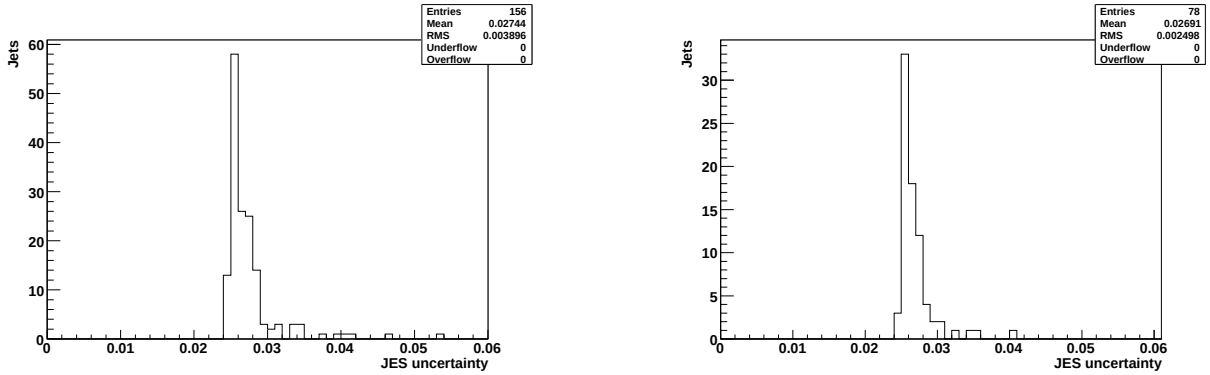

Figure G.1: Uncertainty on the default JES for the 156 light jets (left) and the corresponding 78 b-tagged jets (right) associated to the hadronic decay of a top quark in data.

Bibliography

[1] **CMS** Collaboration, "Measurement of the top quark mass in the lepton+jets channel". CMS-PAS-TOP-10-009. In preparation.

[2] N. Kidonakis, "Next-to-next-to-leading soft-gluon corrections for the top quark cross section and transverse momentum distribution", *Phys. Rev.* **D82** (2010) 114030, arXiv:1009.4935. doi:10.1103/PhysRevD.82.114030.

[3] **CMS** Collaboration, "Combination of top pair production cross sections in pp collisions at 7 TeV and comparisons with theory", 2011. CMS-PAS-TOP-11-001. Figure updated with the latest results from the ATLAS Collaboration available from https://twiki.cern.ch/twiki/bin/view/CMSPublic/PhysicsResultsTOP11001Update/.

[4] M. C. Smith and S. S. Willenbrock, "Top-quark pole mass", *Phys. Rev. Lett.* **79** (1997) 3825–3828, arXiv:hep-ph/9612329. doi:10.1103/PhysRevLett.79.3825.

[5] W. A. Bardeen, A. J. Buras, D. W. Duke et al., "Deep-inelastic scattering beyond the leading order in asymptotically free gauge theories", *Phys. Rev.* **D18** (1978) 3998. doi:10.1103/PhysRevD.18.3998.

[6] M. Beneke et al., "Top quark physics", arXiv:hep-ph/0003033. 2000.

[7] **Particle Data Group** Collaboration, K. Nakamura et al., "Review of particle physics", *J. Phys.* **G37** (2010) 075021. doi:10.1088/0954-3899/37/7A/075021.

[8] A. H. Hoang and I. W. Stewart, "Top mass measurements from jets and the Tevatron top-quark mass", *Nucl. Phys. Proc. Suppl.* **185** (2008) 220–226, arXiv:0808.0222. doi:10.1016/j.nuclphysbps.2008.10.028.

[9] A. H. Hoang, "What top mass is measured at the LHC", in *Strong interactions: From methods to structures*, 474th Wilhelm und Else Heraeus Seminar. Bad Honnef, Germany, 12-16 February 2011. Available from http://www.tp2.ruhr-uni-bochum.de/forschung/vortraege/workshops/bh11/.

[10] J. R. Incandela, A. Quadt, W. Wagner et al., "Status and prospects of top-quark physics", *Prog. Part. Nucl. Phys.* **63** (2009) 239–292, arXiv:0904.2499. doi:10.1016/j.ppnp.2009.08.001.

[11] The **ALEPH**, **CDF**, **D0**, **DELPHI**, **L3**, **OPAL**, **SLD** Collaborations, the **LEP Electroweak Working Group**, the **Tevatron Electroweak Working Group**, and the SLD electroweak and heavy flavor groups, "Precision electroweak measurements and constraints on the Standard Model", arXiv:1012.2367. 2010.

[12] S. Heinemeyer, W. Hollik, D. Stockinger et al., "Precise prediction for M_W in the MSSM", *JHEP* **08** (2006) 052, arXiv:hep-ph/0604147. Figure updated 2010 taken from http://www.ifca.unican.es/users/heinemey/uni/plots/. doi:10.1088/1126-6708/2006/08/052.

[13] F. Fiedler, "Precision measurements of the top quark mass", arXiv:1003.0521. 2010.

[14] The Tevatron Electroweak Working Group for the **CDF** and **D0** Collaborations, "Combination of CDF and D0 results on the mass of the top quark using up to 5.6 fb^{-1} of data", arXiv:1007.3178. 2010.

[15] **CMS** Collaboration, "First measurement of the top quark mass in pp collisions at $\sqrt{s} = 7$ TeV", 2011. CMS-PAS-TOP-10-006.

[16] **ATLAS** Collaboration, "Measurement of the top-quark mass using the template method in pp collisions at $\sqrt{s} = 7$ TeV with the ATLAS detector", 2011. ATLAS-CONF-2011-033.

[17] P. Bryant and L. Evans, eds., "LHC machine", *JINST* **3** (2008) S08001. doi:10.1088/1748-0221/3/08/S08001.

[18] M. Ferro-Luzzi, "2010 experience and expectations for 2011", in *Proceedings of the LHC Beam Operation Workshop, Evian, France, 7-9 December 2010*, B. Goddard, ed. 2011.

[19] **CMS** Collaboration, R. Adolphi et al., "The CMS experiment at the CERN LHC", *JINST* **3** (2008) S08004. doi:10.1088/1748-0221/3/08/S08004.

[20] **CMS** Collaboration, "Tracking and vertexing results from first collisions", 2010. CMS-PAS-TRK-10-001.

[21] **CMS** Collaboration, "Electromagnetic calorimeter calibration with 7 TeV data", 2010. CMS-PAS-EGM-10-003.

[22] **CMS** Collaboration, S. Chatrchyan et al., "Performance of the CMS hadron calorimeter with cosmic ray muons and LHC beam data", *JINST* **5** (2010) T03012, arXiv:0911.4991. doi:10.1088/1748-0221/5/03/T03012.

[23] **CMS** Collaboration, G. L. Bayatian et al., "CMS physics: Technical design report", 2006. CERN-LHCC-2006-001.

[24] **CMS** Collaboration, "Measurement of CMS luminosity", 2010. CMS-PAS-EWK-10-004.

[25] J. Alwall et al., "MadGraph/MadEvent v4: the new web generation", *JHEP* **09** (2007) 028, arXiv:0706.2334. doi:10.1088/1126-6708/2007/09/028.

[26] T. Sjöstrand, S. Mrenna, and P. Skands, "PYTHIA 6.4 physics and manual", *JHEP* **05** (2006) 026, arXiv:hep-ph/0603175. doi:10.1088/1126-6708/2006/05/026.

[27] M. L. Mangano, M. Moretti, F. Piccinini et al., "Matching matrix elements and shower evolution for top-quark production in hadronic collisions", *JHEP* **01** (2007) 013, arXiv:hep-ph/0611129. doi:10.1088/1126-6708/2007/01/013.

[28] R. Field, "Early LHC underlying event data - findings and surprises", arXiv:1010.3558. 2010.

[29] Tune Z2 is identical to the tune Z1 described in [28] except that Z2 uses the CTEQ6L PDF while Z1 uses CTEQ5L.

[30] J. Allison et al., "Geant4 developments and applications", *IEEE Trans. Nucl. Sci.* **53** (2006) 270. doi:10.1109/TNS.2006.869826.

[31] J. M. Campbell and R. K. Ellis, "MCFM for the Tevatron and the LHC", *Nucl. Phys. Proc. Suppl.* **205-206** (2010) 10–15, arXiv:1007.3492. doi:10.1016/j.nuclphysbps.2010.08.011.

[32] K. Melnikov and F. Petriello, "Electroweak gauge boson production at hadron colliders through $\mathcal{O}(\alpha_s^2)$", *Phys. Rev.* **D74** (2006) 114017, arXiv:hep-ph/0609070. doi:10.1103/PhysRevD.74.114017.

[33] **CMS** Collaboration, "Measurement of the $t\bar{t}$ pair production cross section at $\sqrt{s} =$ 7 TeV using the kinematic properties of lepton+jets events", 2011. CMS-PAS-TOP-10-002.

[34] **CMS** Collaboration, "Performance of muon identification in pp collisions at $\sqrt{s} =$ 7 TeV", 2010. CMS-PAS-MUO-10-002.

[35] S. Baffioni et al., "Electron reconstruction in CMS", *Eur. Phys. J.* **C49** (2007) 1099–1116. doi:10.1140/epjc/s10052-006-0175-5.

[36] **CMS** Collaboration, "Particle-flow event reconstruction in CMS and performance for jets, taus, and MET", 2009. CMS-PAS-PFT-09-001.

[37] M. Cacciari, G. P. Salam, and G. Soyez, "The anti-k_t jet clustering algorithm", *JHEP* **04** (2008) 063, arXiv:0802.1189. doi:10.1088/1126-6708/2008/04/063.

[38] **CMS** Collaboration, "Plans for jet energy corrections at CMS", 2008. CMS-PAS-JME-07-002.

[39] **CMS** Collaboration, "Jet performance in pp collisions at $\sqrt{s} = 7$ TeV", 2010. CMS-PAS-JME-10-003.

[40] **CMS** Collaboration, "Jet energy corrections determination at 7 TeV", 2010. CMS-PAS-JME-10-010.

[41] **CMS** Collaboration, "Algorithms for b jet identification in CMS", 2009. CMS-PAS-BTV-09-001.

[42] **CMS** Collaboration, "Commissioning of b-jet identification with pp collisions at $\sqrt{s} = 7$ TeV", 2010. CMS-PAS-BTV-10-001.

[43] **CMS** Collaboration, "Measurement of the $t\bar{t}$ Pair Production Cross Section at $\sqrt{s} =$ 7 TeV using b-quark Jet Identification Techniques in Lepton+Jet Events", 2011. CMS-PAS-TOP-10-003.

[44] **CMS** Collaboration, "Jet energy resolution in CMS at $\sqrt{s} = 7$ TeV", 2011. CMS-PAS-JME-10-014.

[45] **ATLAS** Collaboration, G. Aad et al., "Expected Performance of the ATLAS Experiment - Detector, Trigger and Physics", `arXiv:0901.0512`. pp. 909-911, 2009.

[46] **CDF** Collaboration, A. Abulencia et al., "Top quark mass measurement using the template method in the lepton + jets channel at CDF II", *Phys. Rev.* **D73** (2006) 032003.

[47] R. Barlow, "Application of the Bootstrap resampling technique to Particle Physics experiments". Manchester, 2000. MAN/HEP/99/4.

[48] This calculation was adopted from: `http://home.fnal.gov/~cplager/log/1007/log.html`.

[49] H.-L. Lai et al., "Uncertainty induced by QCD coupling in the CTEQ global analysis of parton distributions", *Phys. Rev.* **D82** (2010) 054021, `arXiv:1004.4624`. `doi:10.1103/PhysRevD.82.054021`.